(12)

DDC
MAY 8 1978
F

ENGINEERING AND INDUSTRIAL EXPERIMENT STATION

College of Engineering

University of Florida

Gainesville

Electrical Properties of Polycrystalline
Ceramic Insulators

Final Report
February 20, 1978

To the

Office of Naval Research
Department of the Navy
Washington, D. C.   20360

For the Period April 1, 1975 - July 31, 1977
Contract No. N00014-75-C-0888

by

Ronald Loehman*, Principal Investigator
Robert DeHoff, Co-Investigator
G. Rama Rao, Post Doctoral Research Associate

Department of Materials Science and Engineering
University of Florida
Gainesville, Florida   32611

* Present address: Division 5846 Sandia Laboratories, Albuquerque, N. M.   87111

REPORT DOCUMENTATION PAGE	READ INSTRUCTIONS BEFORE COMPLETING FORM

1. REPORT NUMBER	2. GOVT ACCESSION NO.	3. RECIPIENT'S CATALOG NUMBER
Final Report	9	Final rept. 1 Apr 75-31 Jul 77

4. TITLE (and Subtitle)

Electrical Properties of Polycrystalline Ceramic Insulators.

5. TYPE OF REPORT & PERIOD COVERED

Final
April 1, 1975-July 31, 1977

6. PERFORMING ORG. REPORT NUMBER

7. AUTHOR(s)

Ronald E. Loehman,
Robert DeHoff and
G. Rama Rao

8. CONTRACT OR GRANT NUMBER(s)

N00014-75-C-0888

9. PERFORMING ORGANIZATION NAME AND ADDRESS

University of Florida
Department of Materials Science & Engineering
Gainesville, Florida 32611

10. PROGRAM ELEMENT, PROJECT, TASK AREA & WORK UNIT NUMBERS

20 Feb 78

11. CONTROLLING OFFICE NAME AND ADDRESS

Office of Naval Research
Department of the Navy
Washington, D. C. 20360

12. REPORT DATE

February 20, 1978

13. NUMBER OF PAGES

103 108 p.

14. MONITORING AGENCY NAME & ADDRESS(if different from Controlling Office)

15. SECURITY CLASS (of this report)

Unclassified

15a. DECLASSIFICATION/ DOWNGRADING SCHEDULE

16. DISTRIBUTION STATEMENT (of this Report)

This document has been approved for public release and sale; its distribution is unlimited.

17. DISTRIBUTION STATEMENT (of the abstract entered in Block 20, if different from Report)

18. SUPPLEMENTARY NOTES

19. KEY WORDS (Continue on reverse side if necessary and identify by block number)

Quantitative Microscopy
Dielectric Properties
Microstructure-Property Relations
Polycrystalline Al_2O_3

Barium Titanate
Ferroelectric Ageing

20. ABSTRACT (Continue on reverse side if necessary and identify by block number)

An attempt has been made to show the effect of microstructure on electrical properties in several types of idealized polycrystalline ceramic insulators. The concept of the path of microstructural change was used to vary hot-pressing or sintering conditions to produce samples of Al_2O_3-porosity and Al_2O_3-SiO_2 with systematically related microstructures. The most detailed quantitative microstructural study yet reported for a ceramic system was made on these samples. Information on volume fractions, surface area,

DD FORM 1473 1 JAN 73
EDITION OF 1 NOV 65 IS OBSOLETE
S/N 0102-LF-014-6601

408174

curvatures and lengths of various features shows clearly that classifying specimens only on the basis of density and average grain size, as is commonly done, tends to lump together samples with very different microstructrues, thus observing microstructure-porsity relations. Dielectric measurements on Al_2O_3-porosity specimens with similar densities and chemical compositions but different values for the 'quantitative microscopic variables reveal strong differences inconductivity, dielectric constant and dielectric loss behavior. A qualitative model involving bulk and grain boundary conduction is advanced to explain dielectric data obtained for a series of systematically related Al_2O_3-porosity specimens. A quantitative microscopic investigation of $BaTiO_3$ microstructure to determine if the technique might be useful in understanding ferroelectric ageing effects is disucssed in the second part of the report.

ACCESSION for

NTIS   White Section
DDC   Buff Section
UNANNOUNC'D
JUSTIFICATION ....

BY
DISTRIBUTION/AVAILABILITY CODES
Dist.

A

TABLE OF CONTENTS

Introduction

The electrical properties of heterogeneous systems have been the subject of considerable practical and theoretical interest for many years. As early as 1894, Maxwell[1], and later others,[2-6] developed models to predict the dielectric behavior of mixtures of geometrically idealized particles dispersed in media with different electrical properties. These models give mixing rules in which an effective conductivity can be calculated in terms of the volume fractions and conductivities of the pure components. Wimmer, Graham and Tallan[7] recently reviewed these mixing rules and discussed their applicability to ceramic systems. Other treatments such as effective medium theory[8-10] and percolation theory[11-16] have been applied to heterogenous systems with varying success, as discussed in our 1976 Technical Report[17].

Each of these models so far has been limited in its applicability to real ceramic systems. In part this is due to mathematical complexities in the theories which prevent analytic solutions for all but the simplest, least realistic geometries; e.g., isolated spheres in a continuous, isotropic medium. In part also, it is due to an almost universally inadequate level of microstructural characterization in the ceramic systems under study. No model containing materials parameters more complex than volume fractions can be applied to systems in which only average grain sizes are measured.

For a few ceramic systems the simple geometric theories do work; Koops,[18] for example, found his experimental data to be in excellent agreement with a simple two-layer model of conducting grains separated by insulating layers

in nickel-zinc ferrite. For most ceramics, however, microstructures are more complicated and the geometrically idealized models are inadequate. A good example is Tien's work[19] on two-phase mixtures in the $CaO-ZrO_2$ system in which his electrical conductivity data could not be fit by any of the simple mixture rules. However, he later[20] developed a geometrically more realistic model which incorporated (apparently independently) some of the features of the percolation theory and which fit his data well.

Quantitative Microscopy

The philosophy on which the present work is based is that progress toward developing more realistic conduction models for ceramic materials requires a quantitative characterization of microstructures at a level not generally achieved at present. The qualitative characterization of a ceramic microstructure should be formulated in terms of a listing of the 0, 1, 2, and 3-dimensional features that it contains, possibly accompanied by descriptive modifiers, such as "fine," "coarse," "equiaxed," "irregular," etc. A complete list of the features that may exist in a one-phase polycrystal and in a porous polycrystalline material is presented in Table I[21].

The microstructural state may be quantified by recognizing that each of the features listed in Table I has associated with it one or more geometric properties, as shown in Table II, and by assigning values to one or more of these properties. Much progress has been made in the last decade in identifying the set of geometric properties that has unambiguous meaning for real microstructures, and in developing procedures for making quantitative estimates of these properties [22-24]. However, it is clear from Table II that a complete evaluation of a porous polycrystal structure requires the

Table I

Qualitative Microstructural States for Single Phase and Porous Polycrystals

	Dimensionality	Feature	Designation
One Phase Polycrystals	3	Grains	α
	2	Grain Faces	$\alpha\alpha$
	1	Grain Edges (Triple Lines)	$\alpha\alpha\alpha$
	0	Grain Corners (Quadruple Points)	$\alpha\alpha\alpha\alpha$
Porous Polycrystals	3	Pores	α
		Grains	ρ
	2	Pore-solid Interface	$\alpha\rho$
		Grain Boundaries	$\alpha\alpha$
	1	Triple Lines (on the pore surface)	$\alpha\alpha\rho$
		Triple Lines (in the grain boundary network)	$\alpha\alpha\alpha$
	0	Quadruple Points (on the pore surface)	$\alpha\alpha\alpha\rho$
		Quadruple Points (in the Grain Boundary Network)	$\alpha\alpha\alpha\alpha$

Table II

Quantitative Microstructural States

Geometrical Properties Associated with Each of the Features in Table I

	Desig-nation	Properties — Metric			Properties — Topological		
		Property	Symbol	Units	Property	Symbol	Units
One Phase Polyxtls	α	---	---	---	Number per unit volume	N_V^{α}	1/cm^3
	αα	Surface area per unit volume	$S_V^{\alpha\alpha}$	cm^2/cm^3	Number per unit volume	$N_V^{\alpha\alpha}$	1/cm^3
					Connectivity per unit volume	$C_V^{\alpha\alpha}$	1/cm^3
	ααα	Length per unit volume	$L_V^{\alpha\alpha\alpha}$	cm/cm^3	Number per unit volume	$N_V^{\alpha\alpha\alpha}$	1/cm^3
					Connectivity per unit volume	$C_V^{\alpha\alpha\alpha}$	1/cm^3
	αααα	---	---	---	Number per unit volume	$N_V^{\alpha\alpha\alpha\alpha}$	1/cm^3
Porous Polyxtls	α	Volume fraction	V_V^{α}	1	Number per unit volume	N_V^{α}	1/cm^3
					Connectivity per unit volume	C_V^{α}	1/cm^3
	ρ	Volume fraction	V_V^{ρ}	1	Number per unit volume	N_V^{ρ}	1/cm^3
					Connectivity per unit volume	C_V^{ρ}	1/cm^3
	αρ	Surface area per unit volume	$S_V^{\alpha\rho}$	cm^2/cm^3	Number per unit volume	$N_V^{\alpha\rho}$	1/cm^3
		Total curvature per unit volume	$M_V^{\alpha\rho}$	cm/cm^3	Connectivity per unit volume	$C_V^{\alpha\rho}$	1/cm^3
	αα	Surface area per unit volume	$S_V^{\alpha\alpha}$	cm^2/cm^3	Number per unit volume	$N_V^{\alpha\alpha}$	1/cm^3
					Connectivity per unit volume	$C_V^{\alpha\alpha}$	1/cm^3
	ααρ	Length per unit volume	$L_V^{\alpha\alpha\rho}$	cm/cm^3	Number per unit volume	$N_V^{\alpha\alpha\rho}$	1/cm^3
		Total curvature per unit volume	$M_V^{\alpha\alpha\rho}$	cm/cm^3	Connectivity per unit volume	$C_V^{\alpha\alpha\rho}$	1/cm^3
	ααα	Length per unit volume	$L_V^{\alpha\alpha\alpha}$	cm/cm^3	Number per unit volume	$N_V^{\alpha\alpha\alpha}$	1/cm^3
					Connectivity per unit volume	$C_V^{\alpha\alpha\alpha}$	1/cm^3
	αααρ	---	---	---	Number per unit volume	$N_V^{\alpha\alpha\alpha\rho}$	1/cm^3
	αααα	---	---	---	Number per unit volume	$N_V^{\alpha\alpha\alpha\alpha}$	1/cm^3

experimental determination of 6 metric properties and 10 or more topological properties.[*] While these properties are all independently variable in principle, in practice it is probable that a sequence of microstructures that are similarly fabricated will not exhibit all these geometric degrees of freedom. Experience with somewhat similar cases in the past had shown that quantification adequate for this program would necessitate analysis of three to five properties. The level of quantification required to describe an experimentally observed behavior could not be determined _a priori_, however. The following levels of quantification were pursued in this program to yield measures of the primary geometric degrees of freedom for the structures under examination.

1. <u>One Phase Polycrystals</u>:

    a) $S_V^{\alpha\alpha}$, the surface area of grain boundaries per unit volume;

    b) $L_V^{\alpha\alpha\alpha}$, the length of triple line per unit volume.

2. <u>Porous Polycrystals</u>:

    a) Geometry of the porosity:

        1) V_V^ρ, the volume fraction of porosity

        2) $S_V^{\alpha\rho}$, surface area of pore-solid interface per unit volume,

        3) $M_V^{\alpha\rho}$, total curvature of pore-solid interface per unit volume.

    b) Geometry of the Grain Boundary Network:

        1) S_V, surface area of grain boundaries per unit volume.

3. <u>Two -Phase Systems</u>

    This is equivalent to (2) above with the minor phase substituted

    for the porosity.

---

*It should be recognized that the topological properties listed in Table II are not all independent.

Information on three-dimensional microstructural geometry may be obtained from simple counting measurements made on a suitable representative two-dimensional section through this structure. The only limitations are that the features of interest must be homogeneously distributed in a random fashion through the structure or, if nonuniformities exist, that they are represented appropritely in the same analyses and that enough measurements be made to provide adequate statistics of the count distribution. If the grain and domain features discussed below are sufficiently uniformly distributed through a polycrystalline sample, a single polished section is a good representation of its three-dimensional characteristics. The quantitative microscopy counts require that a grid be superimposed on the polished section and a count taken of the juxtaposition of grid points and lines with geometric elements seen in the section. For example, it can be shown[23] that the average number fraction of grid points, $\overline{P}_P$, falling within a given phase, α, is directly proportional to the volume fraction of that phase,

$$V_V^\alpha = \overline{P}_P, \text{ where } \sum_i \overline{V}_V^i = \sum \overline{P}_P^i = 1$$

This is the point-count, P_P. Another count of interest is the line-intercept count P_L^α, defined as the number of intersections a grid line makes with the boundary (or partial boundary) of the phase of interest, divided by the total length of grid line used. The average intercept count with the boundary (or the α-β two-phase boundary) can be shown[23] to be proportional to the area per volume of this interface in three-dimensions.

$$S_V^\alpha = (\tfrac{1}{2}) \, \rho_L^\alpha \; ; \; S_V^{\alpha\beta} = (\tfrac{1}{2}) \, \rho_L^{\alpha\beta}$$

Thus, this count can be applied to a complete phase boundary or to only a particular boundary between two phases. A parameter that may be derived from these quantities is the mean intercept, $\overline{\lambda}$, or the average surface - to-surface distance in a structure and may be defined for a total phase,

$$\overline{\lambda}^{\alpha} = \frac{4V_V^{\alpha}}{S_V^{\alpha}}$$

or for the grains within a phase,

$$\overline{\lambda}_g^{\alpha} = \frac{4V_V^{\alpha}}{S_V^{\alpha\beta} + 2S_V^{\alpha\alpha}}$$

The common $\alpha-\alpha$ interface area is entered twice since it bounds two volumes but it is only counted by one intercept with the grid line. This $\overline{\lambda}$ parameter is not necessarily equal to a grain diameter or crystal edge length but is a measure of scale that depends on the surface-to-volume ratio of the geometry being analyzed; $\overline{\lambda}^{\alpha}$ for monosized, spherical α particles in a β matrix would equal 2/3 of the sphere diameter. Thus, the use of the $\overline{\lambda}$ parameter is not limited to distinct close shapes but may even be applied to multiply connected geometries, e.g., a sintered-body with interconnected solid and porosity.

The accuracy of these measurements increases with the number of points in the grid and the number of grid placements made. This increased accuracy must be balanced with the greater effort to get more counts. The resolution of the imaging technique used also limits the accuracy. These considerations are disucssed by Moore.[25]

There are other section counts that can be made that provide information on length of line per volume, interface curvature per volume, curvature and torsion of a line in three-dimensions, and particle size distributions of assumed simple particle shapes. With serial section analysis the number per volume and connectivity of a microstructure may be determined.[23]

Choice of Model Systems

Ceramics based on polycrystalline Al_2O_3 were chosen for our primary study because: 1) alumina ceramics are commercially important; 2) the electrical properties of pure, single crystal Al_2O_3 are relatively well known; 3) samples could be fabricated in a wide range of microstructures; and 4) the results could be compared with the extensive literature data on Al_2O_3.

To simplify the microstructural problem, two levels of complexity were selected: (1) Al_2O_3-porosity; and (2) Al_2O_3-SiO_2. It was thought that such a series would allow us to work progressively from an idealized system with relatively simple microstructures up to those which are more nearly character-istic of real insulators. However, as we discovered, even the supposedly simple Al_2O_3-porosity system is sufficiently complicated microstructurally that the effort to understand it occupied us for the major portion of the contract period, leaving less time for investigation of the more complex systems. Thus, we were able to obtain fairly complete results for the Al_2O_3-porosity system, with somewhat fewer data for Al_2O_3-SiO_2.

Sometime after initiation of this research, ONR requested that we consider the problem of ageing of sonar transducers to determine if the effect could be related quantitatively to changes in microstructure. Although not in the original contract, the problem was considered potentially amenable to the techniques of quantitative microscopy and a small effort was begun. $BaTiO_3$ ceramics with different average grain sizes were prepared and then analyzed microstructurally. The experience gained with those samples allowed formulation of experiments on commercial PZT sonar transducer materials. These results are presented in a separate section of this report.

Experimental

Preparation of Al_2O_3-Porosity Specimens:

The concept of "the path of microstructural change" as developed by DeHoff and co-workers[26] was used to produce several series of samples with systematically related structures. DeHoff, et al.[26] previously found that in the sintering of a powder the microstructural variables for successive stages of densification are simply related only for certain combinations of time, temperature and pressure. For our system, specimens hot pressed at constant temperature and pressure for varying times are on the same path of microstructural change. Altering the temperature or the pressure may produce samples on different paths. Figure 1 shows a schematic relation between the volume fraction, V_v, and the surface area, S_v, of a particular phase for different microstructural paths.

All the samples for this portion of the study were made by hot pressing either Dupont K-θ alumina (cationic impurities <150 ppm, surface area $= 8 m^2/g$) or Linde A alumina for various combinations of time, temperature and pressure under vacuum in graphite dies. During the sample warm-up period initial pressures of 300 psi were applied to the powder compacts; once the desired temperature was reached, full pressure was applied. These hot pressing conditions produced a series of states in which the microstructural variables characteristic of samples in the same state are simply related.

Figure 2 is a plot of sample density versus hot pressing time for specimens in the Al_2O_3-porosity system in which samples belonging to the same microstructural path are shown connected by solid lines. Table III lists the preparation conditions and properties measured for these samples.
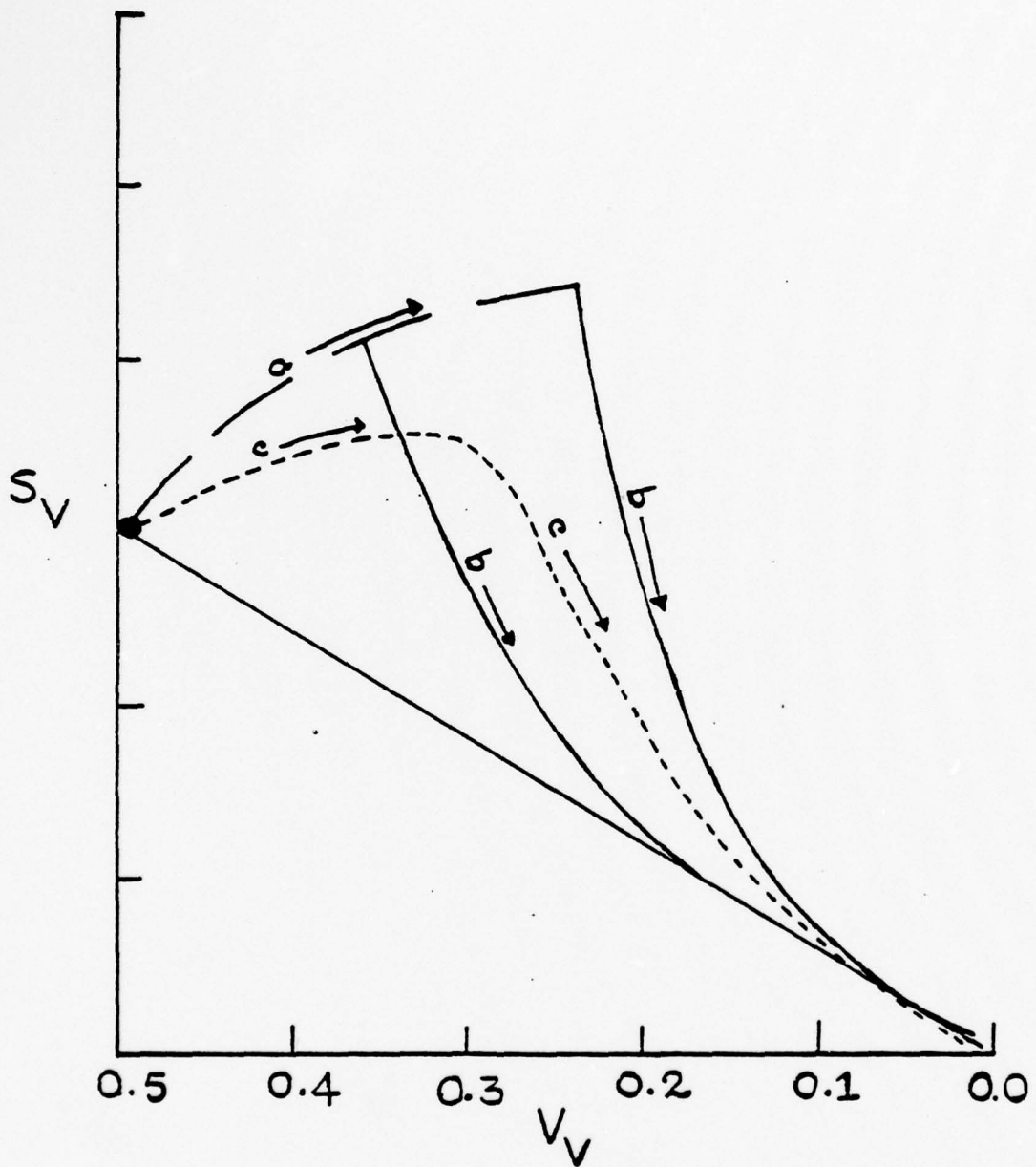
Figure 1. Paths of surface area change for cold pressed
(a) samples, followed by sintering (b) are compared
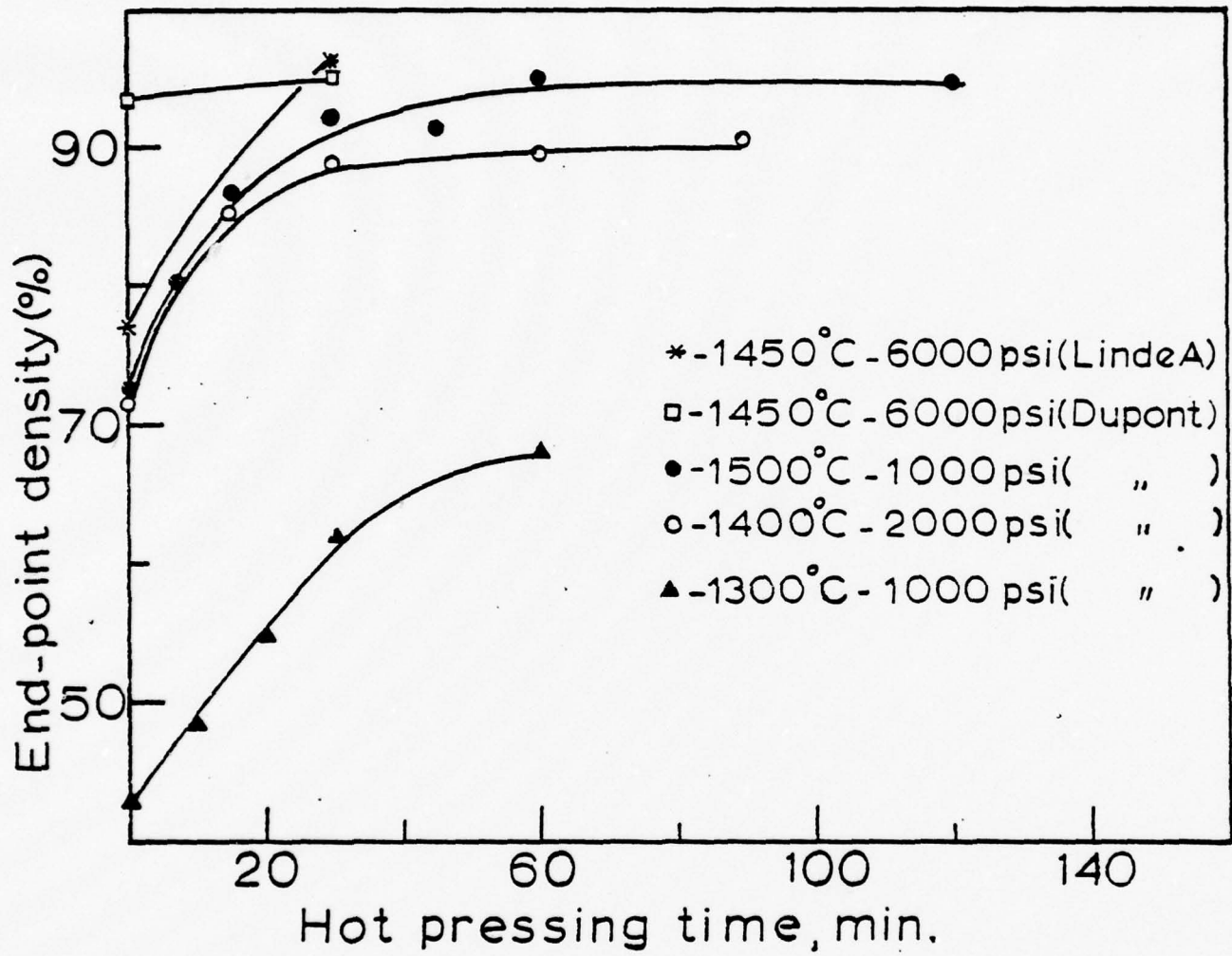with the path obtained by hot pressing(c).

Figure 2. Plot of relative density versus hot pressing time for specimens in the Al_2O_3-porosity system.

TABLE III

Al_2O_3 - Porosity

Sample	Prep (°C/psi/min)	Relative* Density (%)	σ	k'	k"	SEM Fracture	Polish	Q.M
90	1500-1000-0	73	X	X	X	X		
98	1500-1000-7	80	X	X	X	X		X
99	1500-1000-15	87	X	X	X	X		X
91	1500-1000-30	92	X	X	X	X		X
134	1500-1000-45	92	X	X	X	X		X
92	1500-1000-60	95	X	X	X	X		X
93	1500-1000-120	95	X	X	X	X		X
43B	1450-1000-30	64	X	X	X	X		
44A	1450-6000-0	94	X	X	X	X	X	X
37	1450-6000-30	95	X	X	X	X	X	X
47	1450-6000-0 (Linde A)	77	X	X	X		X	X
40B	1450-6000-30 (Linde A)	96	X	X	X		X	X
76	1400-2000-0	71	X	X	X		X	X
105	1400-2000-15	85	X	X	X		X	X
75	1400-2000-30	89	X	X	X		X	X
78	1400-2000-60	90	X	X	X		X	X
77	1400-2000-90	91	X	X	X		X	X
61	1350-4000-0	78						
60	1350-4000-34	95						
96	1300-1000-0	43						
101	1300-1000-10	49						
102	1300-1000-20	55						
103	1300-1000-30	62	X	X	X	X		
100	1300-1000-60	68						
54	1300-4000-0	78						
59	1300-4000-30	91						
52	1300-6000-0	90						
55A	1250-4000-0	64						
58	1250-4000-5	73						
57	1250-4000-10	78						
56	1250-4000-30	89	X	X	X	X		
45A	1200-6000-30	82	X	X	X		X	

* w.r. to bulk density of Al_2O_3 as $3.987 g/cm^3$

X's denote the particular measurements made.

Q.M. denotes Quantitative Microscopy

Preparation of Al_2O_3-SiO_2 Specimens:

Samples were prepared from mixtures of the same DuPont K-θ Al_2O_3 described earlier and Cab-O-Sil fumed silica (Cabot Corp., Boston, Mass). Twenty gram batches in proportions to span the 0 to 28 wt.% SiO_2 range were weighed into 250 ml polyethylene bottles, ball milled over night in methanol using high density Al_2O_3 balls as the milling medium and then dried at 120°C. The alumina balls were weighed before and after milling and the compositions were adjusted to compensate for any weight loss.

Hot pressing at 1700°C in graphite or BN-coated graphite resulted in sample reaction with the dies. To avoid this, samples first were hot pressed in graphite dies at 1450°C-6000psi-30 min and subsequently sintered under vacuum at 1700°C for 30 min while immersed in powder of the same composition. In this manner specimens free of cracks or other flaws were produced. The resulting microstructures ranged from Al_2O_3 grains with a mullite inter-granular phase at 0.5 wt.% SiO_2, to a continuous mullite matrix with dispersed Al_2O_3 at the highest SiO_2 content. Figure 3 is the Al_2O_3-SiO_2 phase diagram with the compositions made by us indicated on it.

Electrical Properties Measurements:

Dielectric properties were routinely measured from 200 Hz to 20KHz in the temperature range form 400 to 1100°C using standard electronics consisting of a Wayne-Kerr B221 Universal Bridge, a Hewlett-Packard 651A Test Osillator, a Monsanto Model 100B frequency counter and a General Radio Type 1232-A null detector. The electrical properties were measured on thin disc-shaped samples using a high temperature, Kanthal wound conductivity cell
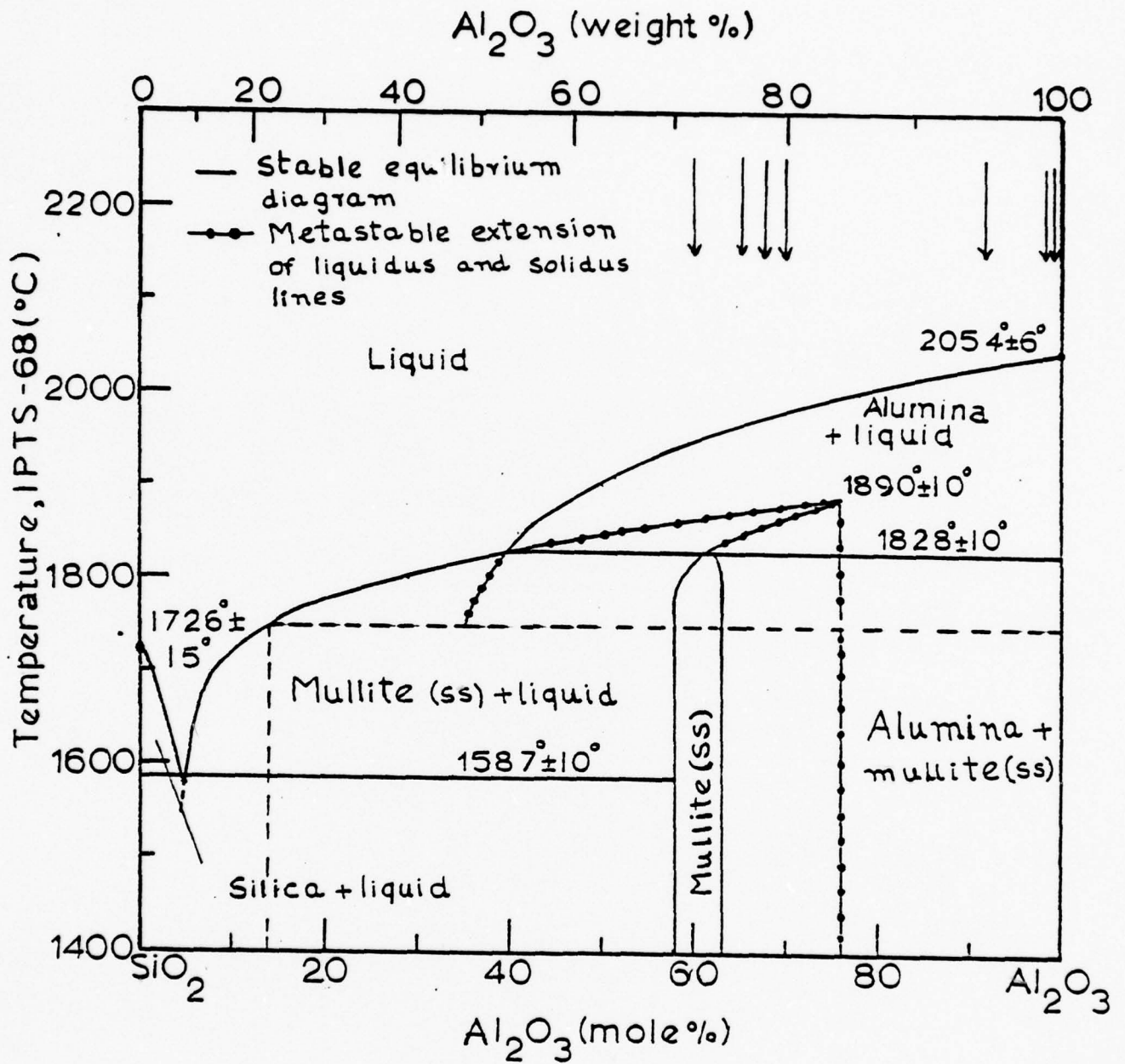
Figure 3. Al$_2$O$_3$-SiO$_2$ phase diagram; the arrows at the top section indicate the compositions of the samples prepared. Ref: I. A. Aksay and J. A. Pask, Science 183. 69 (1974).

fabricated in this laboratory (Fig. 4) utilizing principles discussed in the literature[27,28]. The samples were held in the center position of the cell by platinum guard-cylinders mounted on alumina tubes which were spring-loaded at the ends of the furnace. The platinum electrode pressure contacts used in the measurements were shielded by the Pt guard-cylinders on either side of the sample and were also spring-loaded.

The electrodes were painted on the samples with Englehard #6082 Pt paste in a guarded, three terminal configuration using a special jig to insure reproducible geometry. They were covered with thin (.001"), perforated Pt foil disks and then fired in air to produce a conductive, adherent, abrasion resistant electrode.

After the sample was mounted in the conductivity cell, it was cycled through the temperature range of study (400-1100°C) at least three times prior to taking data to eliminate drift due to electrode annealing effects. In all cases where the samples were properly annealed before measurement, no hysteresis was found over several heating and cooling cycles. Variability due to specimen size effects was checked by removing one sample after electrical measurements, grinding it to half its original thickness, reapplying the electrodes and remeasuring the electrical properties. We found no significant difference between the two measurements.

Quantitative Microscopy Measurements:

Quantitative microscopic analysis requires polished sections in which there is sufficient contrast between microstructural features to permit the counting measurements which are the basis of the technique. Futhermore, the
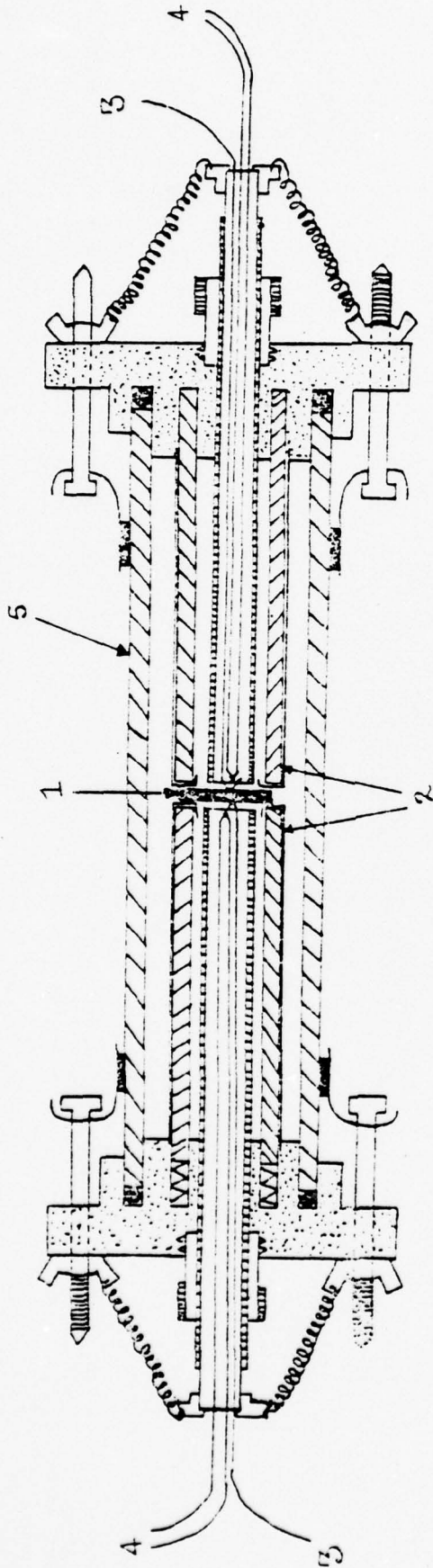
Figure 4. Schematic diagram of the electrical conductivity cell.

1. Sample
2. platinum guard cylinders
3. platinum electrode leads
4. pt-pt(10% Rh) thermocouples
5. furnace tube (winding not shown)

features exposed in the polish plane must be representative of the bulk microstructure in order for the counting measurements to quantify the microstructure accurately. These two requirements, contrast and statistical accuracy, are the cause of many of the delays and frustrations we experienced in this work. The techniques finally developed are described below.

After completion of the dielectric measurements, the specimen was taken from the conductivity cell and abraded with 120 grit silicon carbide to remove the electrodes. The sample was mounted in polymethylmethacrylate, and polished successively on 240,320,400 and 600 grit silicon carbide and final polished with 6 and 1.0µ Buehler's diamond compound. The sample was then cut free from the mount and any remaining mounting material was dissolved away with acetone.

Three methods for revealing the microstructures exposed by the polished sample surface were investigated: 1) chemical etching[29], 2) relief polish, and 3) thermal etching[30]. The degree of etch obtained with the hot sulphuric acid treatment was very difficult to control; a less than optimum etch produced specimens with insufficient contrast, whereas with too long an etch the surface was so contaminated with spurious features (etch pits, accentuated polishing scratches, etc.) that microstructural measurements could not be made accurately. It proved impossible to achieve the optimum etch consistently. Relief polishing failed to produce the contrast required for our measurements. The thermal etching technique that finally proved successful is as follows:

Sample	Hot-pressing conditions	Thermal etching conditions		
		Temperature	Time	Atmosphere
Al_2O_3-porosity	1500°C-1000 psi-t (0-120 min)	1400°C	10 min	Argon
Al_2O_3-porosity	1400°C-2000 psi-t (0-90 min)	1600°C	4 min	Argon
Al_2O_3-porosity	1450°C-6000 psi-t (0-30 min)	1600°C	4 min	Argon
Al_2O_3-SiO_2	1450°C-6000psi- 30 min followed by 1700°C-1 atm- 30 min	1600°C	2-5 min	Argon

Thermal etching had the additional advantage of not accentuating the slight scratches remaining on the specimen. The possibility that thermal etching altered the microstructure was tested by checking the specimen surface after successively higher temperature and longer heat treatment times. Also, in several cases a chemically etched surface was measured, repolished, thermally etched and then remeasured. In all cases, no microstructural changes due to the etching treatment could be detected.

One significant disadvantage of the sample systems chosen for this study is that the scale of the microstructures we obtained were below the optical resolution limit of the Quantimet 720 image analyze computer. Thus time consuming manual counting measurements[23,26] using a scanning electron microscope were required to obtain the quantitative microstructural data.

RESULTS AND DISCUSSION

Microstructural Development in Hot Pressed Alumina

It is convenient to discuss our results using the concept of the "path of microstructural change" introduced in the Experimental Section and illustrated for our specific system by Fig. 2. Although the 1300°C-1000psi-t series shown in Fig. 2 represents a wide variation in densities and would have been an interesting study, the samples produced were very fragile and exhibited unacceptable levels of polishing pullout that could not be overcome by even the most careful metallography. Since reliable quantitative microstructural data could not be obtained on those samples, no further measurements were made. The following d-scussion focusses upon results for the remaining series.

1500°-1000psi-t specimens: A qualitative view of microstructural development in this system is given by the scanning electron micrographs of fracture surfaces presented in Fig. 5. They show the expected progressive increase in grain size as densification proceeds. The quantitative microstructural data calculated from thermally etched, polished surfaces using the SEM at 0° tilt angle are given in Table IV. The relatively good agreement between the calculated volume fraction of porosity, V_V^O, and that determined from the densities is evidence that the features exposed by the sample surface were representative of the microstructure as a whole.

The path of microstructural change for this hot pressing process is summarized in Figures 6 and 7. The variation of surface area and total curvature of the pore-solid interface with porosity is consistent with previous observations on hot pressed ceramic powders.[31,32] Variation of the properties of the grain structure, including surface area of grain boundaries,
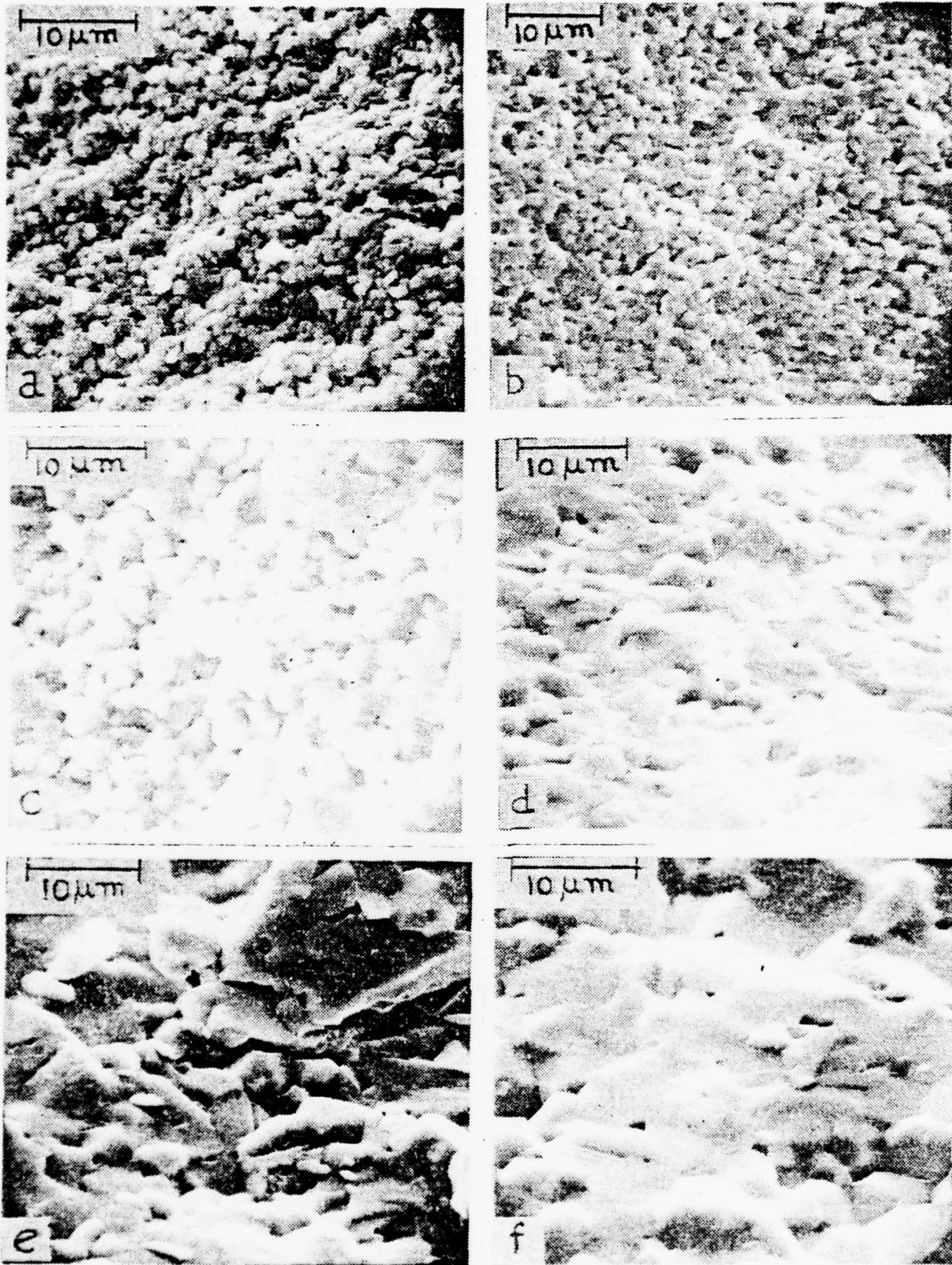
Figure 5. Scanning electron micrographs of the fractured surfaces of
samples: (a) #90, (b) #98, (c) #99, (d) #91, (e) #92 and (f) #93.

TABLE IV

Polycrystalline Al_2O_3
1500°C-1000 psi-t Series
Quantitative Microstructural Properties

Sample	Sintering Time	Rel. Density	V_V^ρ	$S_V^{\alpha\rho}$, cm^{-1}	$S_V^{\alpha\alpha}$, cm^{-1}	$M_V^{\alpha\rho}$, cm^{-2}
#93	120 m	94.53	.03	7.5×10^2	4.78×10^3	1.50×10^7
#92	60 m	95.01	.05	1.32×10^3	4.66×10^3	2.18×10^7
#134	45 m	91.51	.07	9.67×10^2	5.30×10^3	1.223×10^7
#91	30 m	92.27	.09	3.14×10^3	1.01×10^4	8.11×10^7
#99	15 m	86.72	.11	4.09×10^3	8.93×10^3	1.25×10^8
#98	7 m	80.25	.18	5.11×10^3	1.37×10^4	2.64×10^8
#90	0	72.56	[Quantitative Microstructural Data could not be obtained due to excessive pull out in polishing]			

TABLE IV (Cont.)

Sample	$\rho_A^{\alpha\alpha\rho}$, cm^{-2}	$\rho_A^{\alpha\alpha\alpha}$, cm^{-2}	$L_V^{\alpha\alpha\rho}$, cm^{-2}	$L_V^{\alpha\alpha\alpha}$, cm^{-2}	$\overline{\lambda}_\rho = \dfrac{4V_V}{S_V^{\alpha\rho}}$, cm
#93	5.94×10^6	8.45×10^6	1.19×10^7	1.69×10^7	1.6×10^{-4}
#92	9.03×10^6	7.08×10^6	1.81×10^7	1.42×10^7	1.52×10^{-4}
#134	5.05×10^6	1.22×10^7	1.009×10^7	2.44×10^7	2.90×10^{-4}
#91	3.18×10^7	4.33×10^7	6.36×10^7	8.67×10^7	1.146×10^{-4}
#99	4.86×10^7	3.07×10^7	9.72×10^7	6.14×10^7	1.076×10^{-4}
#98	9.48×10^7	6.64×10^7	1.90×10^8	1.33×10^8	1.409×10^{-4}
#90	[Quantitative Microstructural Data could not be obtained due to excessive pull out in polishing]				

TABLE IV (Cont.)

Sample	$\bar{H} = \dfrac{M_V^{\alpha o}}{S_V^{\alpha \rho}}$, cm^{-1}	$\bar{H} \cdot \bar{\lambda}$	$M_V \cdot \bar{\lambda}^2$	$S_V^{grain} = S_V^{\alpha\rho} + 2S_V^{\alpha\alpha}$, cm^{-1}	$[S_V^{\alpha\rho}]^2$, cm^{-2}	$\dfrac{1}{S_V^{\alpha\alpha}}$, cm	$\dfrac{1}{S_V^{\alpha\rho}}$, cm
#93	2.00×10^4	3.2	3.84×10^{-1}	1.03×10^4	5.63×10^5	2.09×10^{-4}	1.33×10^{-3}
#92	1.652×10^4	2.5	5.00×10^{-1}	1.06×10^4	1.74×10^6	2.15×10^{-4}	7.58×10^{-4}
#134	1.265×10^4	3.67	1.03×10^0	1.16×10^4	9.35×10^5	1.89×10^{-4}	1.03×10^{-3}
#91	2.583×10^4	2.96	1.07×10^0	2.33×10^4	9.86×10^6	9.90×10^{-5}	3.18×10^{-4}
#99	3.056×10^4	3.29	1.45×10^0	2.20×10^4	1.67×10^7	1.12×10^{-4}	2.44×10^{-4}
#98	5.166×10^4	7.28	5.24×10^0	3.25×10^4	2.61×10^7	7.30×10^{-5}	1.96×10^{-4}

#90   [Quantitative Microstructural Data could not be obtained due to excessive pull out in polishing]
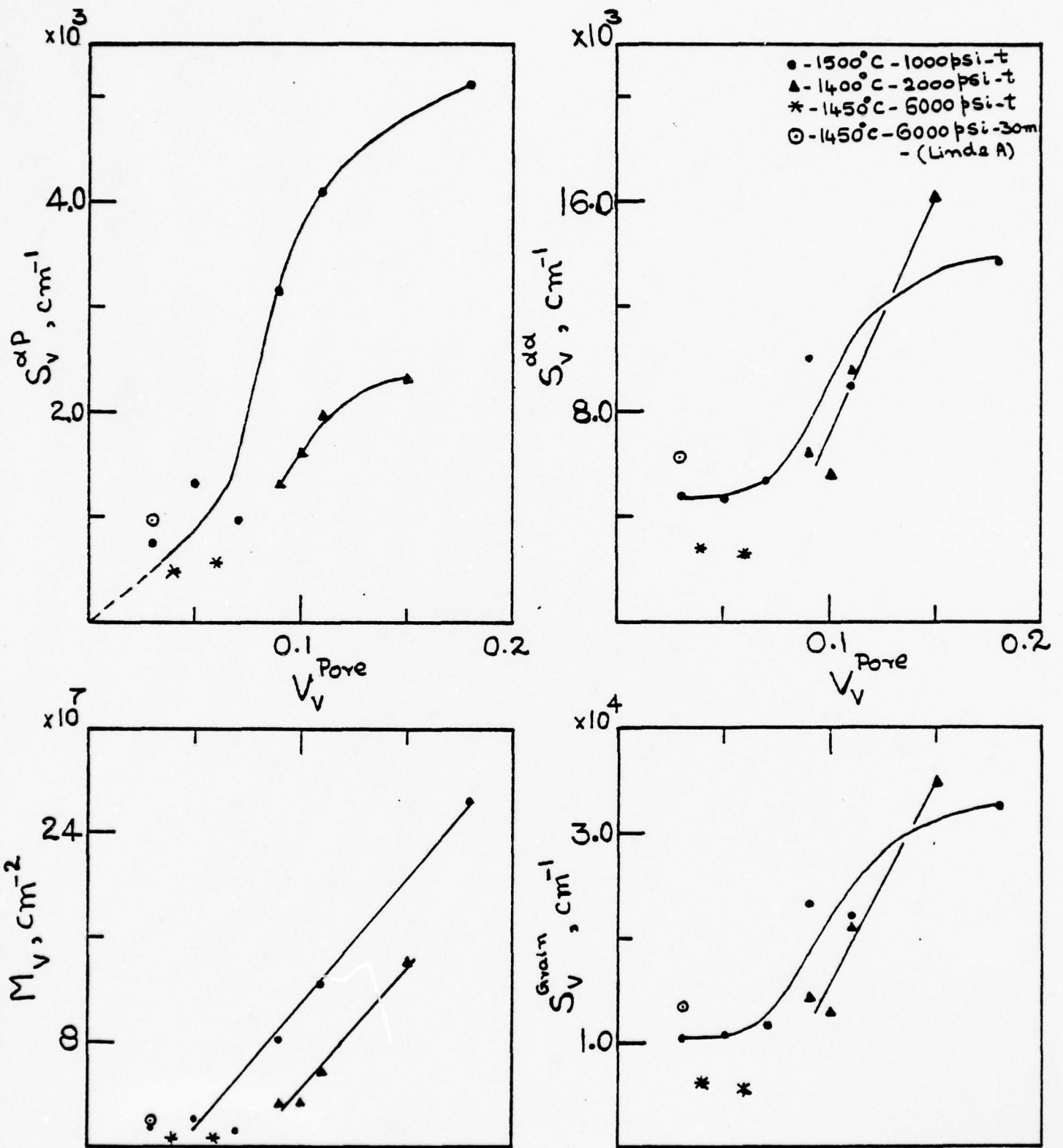
Figure 6. Plot of the microstructural variations versus porosity (hot pressing process) of different samples studied in the Al_2O_3-porosity system.
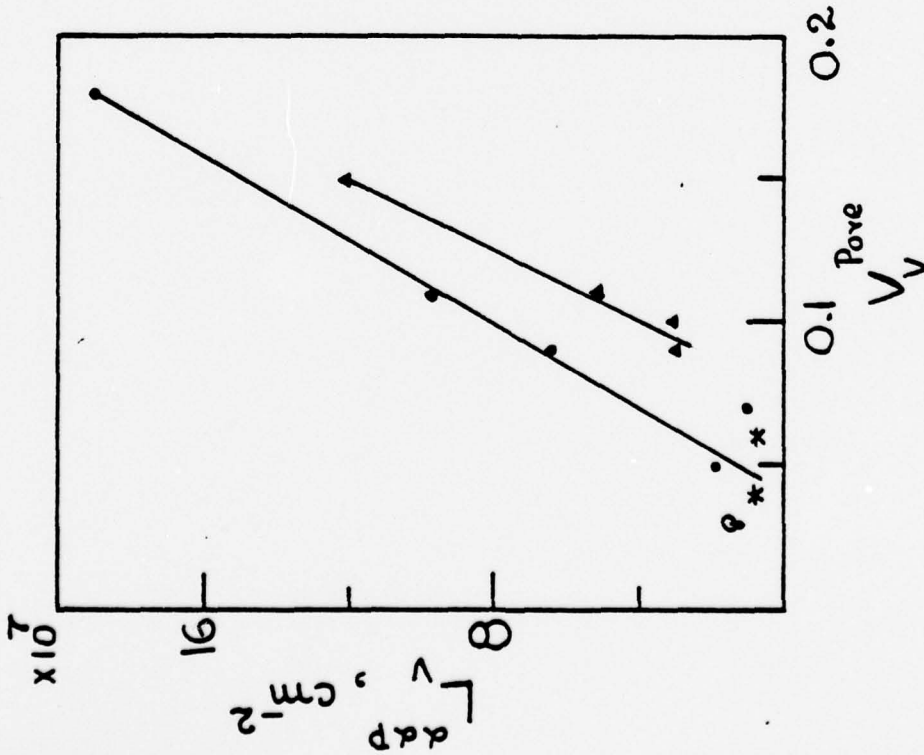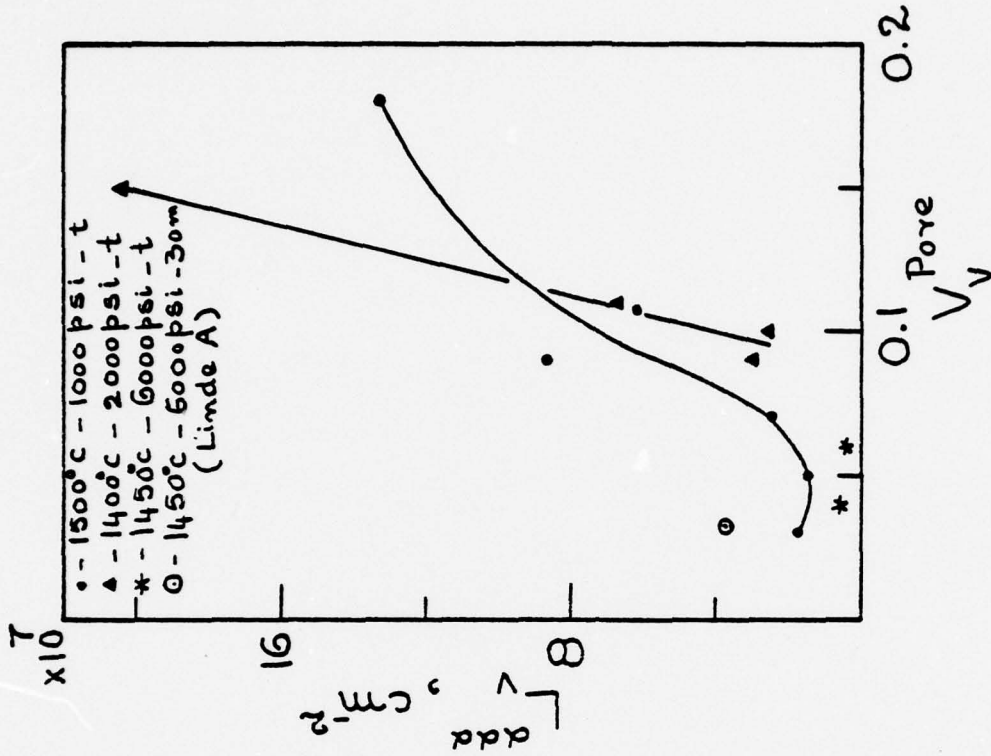
Figure 7. Plot of the microstructural variations versus porosity (hot-pressing process) of different samples studied in the Al_2O_3-porosity system

length of grain edges, and length of the intersection of grain boundaries with the pore-solid interface, with the volume fraction of porosity,(Figures 6 and 7)are also qualitatively consistent with reported observations, although such information is very limited.[31]

1400°C-2000psi-t specimen: This series of samples was prepared to permit exploration of the effect of pressing conditions on the path of microstructural change, and ultimately the electrical properties of the system. The range of densities achieved was somewhat smaller than the previous series, (Figure 2). The quantitative microstructural states, and the path of microstructural change characteristic of these hot pressing conditions are summarized in Table V and Figures 6 and 7. In general, the paths are qualitatively similar to those observed for the 1500°C series, and hence in agreement with previous observations: the paths are quantitatively different.

The Path of Microstructural Change. In the present work the microstructural state of each sample has been characterized by the determination of six potentially independent parameters,(Tables IV and V). Three of these (V_V, $S_V^{\alpha\rho}$ and $M_V^{\alpha\rho}$) characterize the pore phase and its boundary; two characterize the grain structure ,($S_V^{\alpha\alpha}$ and $L_V^{\alpha\alpha\alpha}$), and one ($L_V^{\alpha\alpha\rho}$) gives information about the interaction between the grain boundary network and the pore phase. The state of the system may be visualized as a point in a six-dimensional space whose axes are these variables. The path of microstructural change for a process, such as hot pressing, may be visualized as a connected sequence of points in that space. The form of this curve in six dimensional space must be inferred by projecting it upon various base planes in the space; most commonly, projections on planes involving the V_V axes are used, because

Table V

Polycrystalline Al_2O_3
1400°C-2000psi-t Series
Quantitative Microstructural Properties

Sample No.	Time of sintering	Rel. Density	V_v^ρ	$S_v^{\alpha\rho}$, cm^{-1}	$S_v^{\alpha\alpha}$, cm^{-1}	$M_v^{\alpha\rho}$, cm^{-2}
# 77	90m	90.6	.094	1.30×10^3	6.39×10^3	3.25×10^7
# 78	60	89.5	0.105	1.60×10^3	5.58×10^3	3.36×10^7
# 75	30	88.8	0.112	1.95×10^3	9.46×10^3	5.74×10^7
#105	15	85.0	0.150	2.30×10^3	1.62×10^4	1.40×10^8

Table V (Cont.)

Sample No.	$\rho_A^{\alpha\alpha\rho}$, cm^{-1}	$\rho_A^{\alpha\alpha\alpha}$, cm^{-2}	$L_v^{\alpha\alpha\rho}$, cm^{-2}	$L_v^{\alpha\alpha\alpha}$, cm-2	$\bar{\lambda}=\dfrac{4V_v}{\rho_{S_v}^{\alpha\rho}}$, cm^{-1}	$\bar{H}=\dfrac{M_v^{\alpha\rho}}{S_v^{\alpha\rho}}$, cm^{-1}
# 77	1.43×10^7	1.5×10^7	2.86×10^7	3.01×10^7	2.769×10^{-4}	2.50×10^4
# 78	$1.49.10^7$	1.27×10^7	2.98×10^7	2.54×10^7	2.50×10^{-4}	2.10×10^4
# 75	2.53×10^7	3.37×10^7	5.06×10^7	6.73×10^7	2.26×10^{-4}	2.94×10^4
#105	6.06×10^7	1.02×10^8	1.21×10^8	2.05×10^8	2.61×10^{-4}	6.09×10^4

Table V (Cont.)

Sample No.	$\overline{H}.\overline{\lambda}$	$M_v \cdot \overline{\lambda}^2$	$S_v^{grain} = S_v^{\alpha\rho} + 2S_v^{\alpha\alpha}$, cm^{-1}	$[S_v^{\alpha\rho}]^2$, cm^{-2}	$\dfrac{1}{S_v^{\alpha\alpha}}$, cm	$\dfrac{1}{S_v^{\alpha\rho}}$, cm
# 77	6.92x0	24.9x10^{-1}	1.41x10^4	1.69x10^6	1.56x10^{-4}	7.69x.0^{-4}
# 78	5.25	21x0x10^{-1}	1.28x10^4	2.56x10^6	1.79x10-^{4}	6.25x10^{-4}
# 75	6.64	29.3x10^{-1}	2.09x10^4	3.80x10^6	1.06x10^{-4}	5.13x10^{-4}
#105	15.89	95.4x10^{-1}	3.47x10^4	5.29x10^6	6.17x10^{-5}	4.35x10^{-4}

volume fraction is the most direct measure of progress through the process. These projections are shown in Figures 6 and 7 for the processes and powders under investigation.

Projections in other directions are also potentially informative, as well as plots of combinations of the variables against each other. Figure 8 shows a plot of $L_V^{\alpha\alpha\rho}$ versus $M_V^{\alpha\rho}$. It is observed that all of the data for all conditions are well-described by a single straight line with the equation:

$$L_V^{\alpha\alpha\rho} = \frac{3}{4} \quad M_V^{\alpha\rho} \tag{1}$$

This behavior can be rationalized if it is assumed that the pores are all the same shape, such as might be fixed by surface tension requirements, and they lie along grain edges in the solid phase. For a size distribution of pores, the intergral mean curvature is proportional to the first moment of the size distribution:

$$M_V^{\alpha\rho} = k_M(\theta)N_V\overline{D} \tag{2}$$

The length of grain edge on pores is similarly proportional to the first moment:

$$L_V^{\alpha\alpha\rho} = k_L(\theta)N_V\overline{D} \tag{3}$$

where $k_M(\theta)$ and $k_L(\theta)$ are shape factors whose values depend upon the contact dihedral angle (θ) at the $\alpha\alpha\rho$ edges and N_V is the number of pores per unit volume Eliminating $\overline{D}$ gives:

$$L_V^{\alpha\alpha\rho} = \frac{k_M}{k_L} \quad M_V^{\alpha\rho} \tag{4}$$

Comparison with equation (1) shows that, for these systems,

$$\frac{k_M}{k_L} = \frac{3}{4}$$
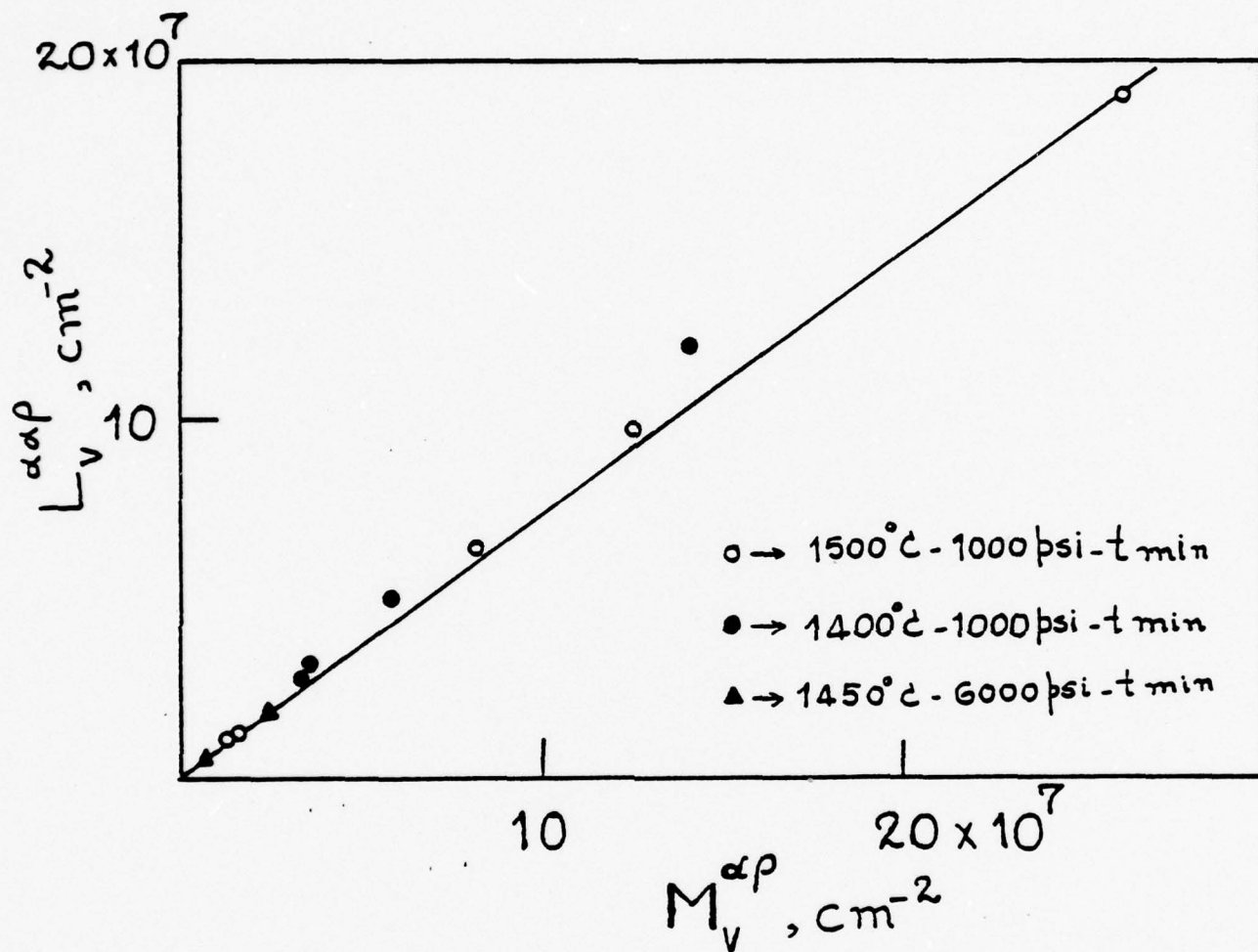
Figure 8. Plot of $L_v^{\alpha\alpha\rho}$ versus $M_v^{\alpha\rho}$ for the samples in the Al_2O_3-porosity system.

Exploration of a variety of model shapes revealed that, for example, lense-shaped pores sitting on the grain faces in the structure cannot give a value of k_M/k_L greater than 1/2. On the other hand, a connected pore network lying exclusively along the grain edges gives a value for this ratio of $(3/\pi)$ or 0.95. It thus appears that an intermediate model, consisting primarily of disconnected pores along the grain edges, is consistent with the observed relation expressed in Figure 8.

Further evidence for the strong interaction between the porosity and the grain structure may be obtained by comparing the measured value of $L_V^{\alpha\alpha\rho}$ with the value that would be expected if the spatial distribution of the grain boundary network and the pore surface area were independent of one another. For such a random structure, it has been shown that[33]:

$$L_V{}_{random}^{\alpha\alpha\rho} = \frac{S_V^{\alpha\rho}S_V^{\alpha\alpha}}{4(1-V_V^P)} \tag{5}$$

Figure 9 shows a comparison of the measured values of $L_V^{\alpha\alpha P}$ with the values computed for this random structure. While there is a relationship between these parameters,

$$L_V{}_{random}^{\alpha\alpha\rho} = 0.11L_V^{\alpha\alpha\rho} \tag{6}$$

they are clearly not equal. Indeed, there is roughly ten times as much $\alpha\alpha P$ triple line in the structure as would exist in a random structure. This result is consistent with the conclusion expressed above, i.e., that virtually all of the porosity lies along triple lines in the grain edge network.
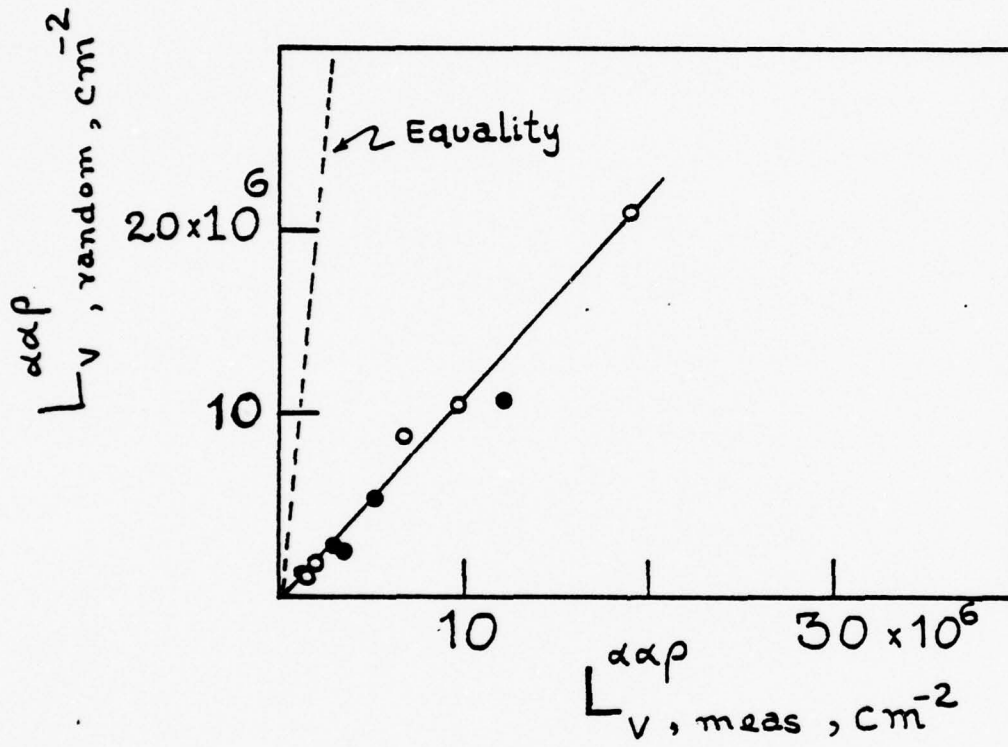
Figure 9. Plot of $L_v^{\alpha\alpha\rho}$ (measured) versus $L_v^{\alpha\alpha\rho}$ (random) computed for random distribution of pores.

Variation of the Path with Hot Pressing Conditions: Each of the paths shown in Figures 6 and 7 compares observations for the 1500°C-1000psi series with the 1400°C-2000psi series, as well as isolated observations for other conditions. Previous work suggests that in hot pressing, the path is insensitive to the hot pressing temperature, and, for progressively higher hot pressing pressures, is displaced upward in surface area.[31] Figure 6 shows that, in sintering alumina under the conditions explored in this study, the path is affected by hot pressing temperature; indeed a large effect is implied, sufficient to overcome the oppositely directed shift associated with increasing the hot pressing pressure.

Qualitatively, the path observed for the 1400°C-2000psi series is characteristic of a structure which, at each step of the process, is coarser than that observed for the 1500°C-1000psi. The tendency is reflected in essentially all of the microstructural information shown in Figures 6 and 7. This behavior is contrary to previous observations on other systems, and contrary to intuition. Further systematic study of the effects of processing conditions upon the path is needed to provide a perspective for these observations.

Microstructural Development in Hot Pressed Al_2O_3-SiO_2 Mixtures:

Table VI lists the samples prepared for this portion of the study with some of their measured properties. Figure 10 is a plot of relative density as a function of SiO_2 content. The resulting microstructures range from Al_2O_3 grains with a mullite intergranular phase at 0.5 wt% SiO_2 to a continuous mullite matrix with dispersed Al_2O_3 at 20 wt% SiO_2. Micrographs of some of these structures are presented in Fig. 11. The 5% and 20% SiO_2 compositions are of particular interest since apparently in the former case the mullite

Table VI

$$Al_2O_3-SiO_2$$
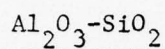
Sample	Weight Fraction of SiO_2	Preparation (°C/psi/min)	Relative* Density (%)	σ	K'	K"	SEM Fracture	SEM Polish	Q.M.
114	0.0	1400-6000-30 and 1700--30	98.81	X	X	X		X	X
85	0.005	1400-6000-30 1700---30	96.38	X X	X X	X X	X	X	X
119	0.01	"	93.35	X	X	X			could not be done
108	0.05	"	97.60	X	X	X		X	X
110	0.20	"	94.44	X	X	X		X	X
130	0.22	"	93.37	X	X	X		X	X
122	0.239	"	94.56	X	X	X		X	X
126	0.28	"	95.99	X	X	X		X	X

*Relative densities are caluclated with respect to the respective component densities as follows:

Density of Al_2O_3 = 3.987g/cm^3

Density of mullite ($3Al_2O_3 \cdot 2SiO_2$) = 3.16 g/cm^3

Density of SiO_2 = 2.648g/cm^3
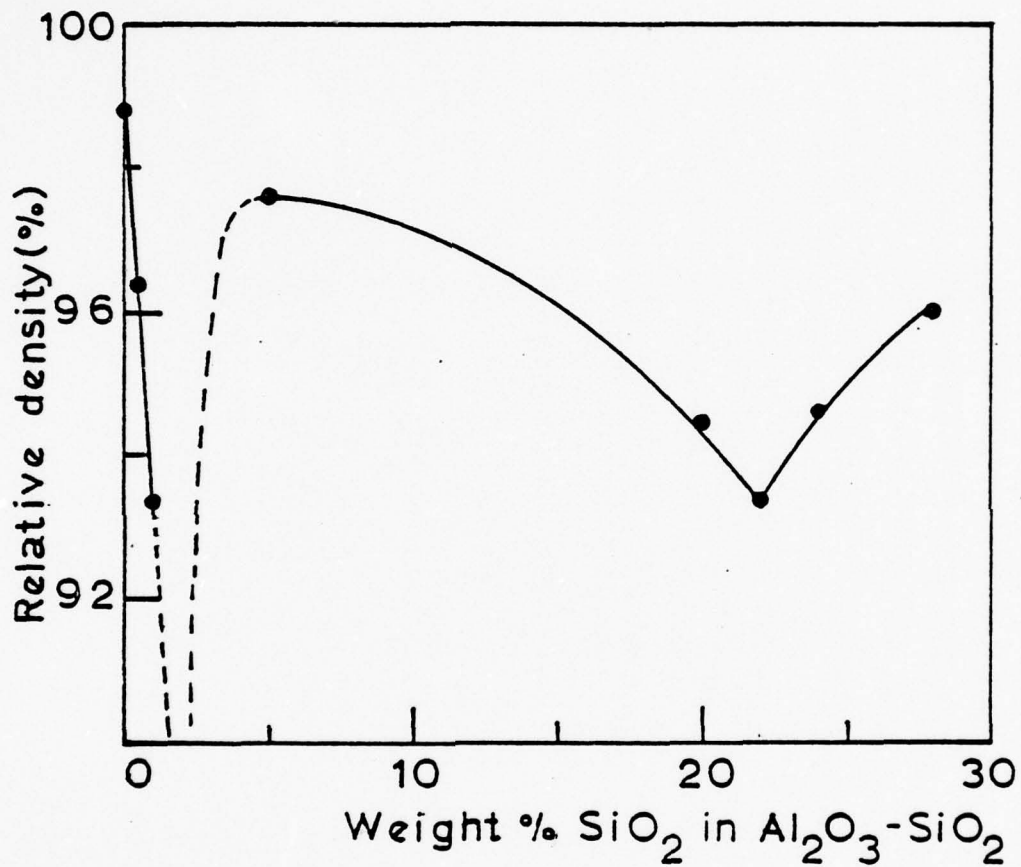
Figure 10. Plot of relative density versus weight% SiO_2 content of the samples studied in the Al_2O_3-SiO_2 system.
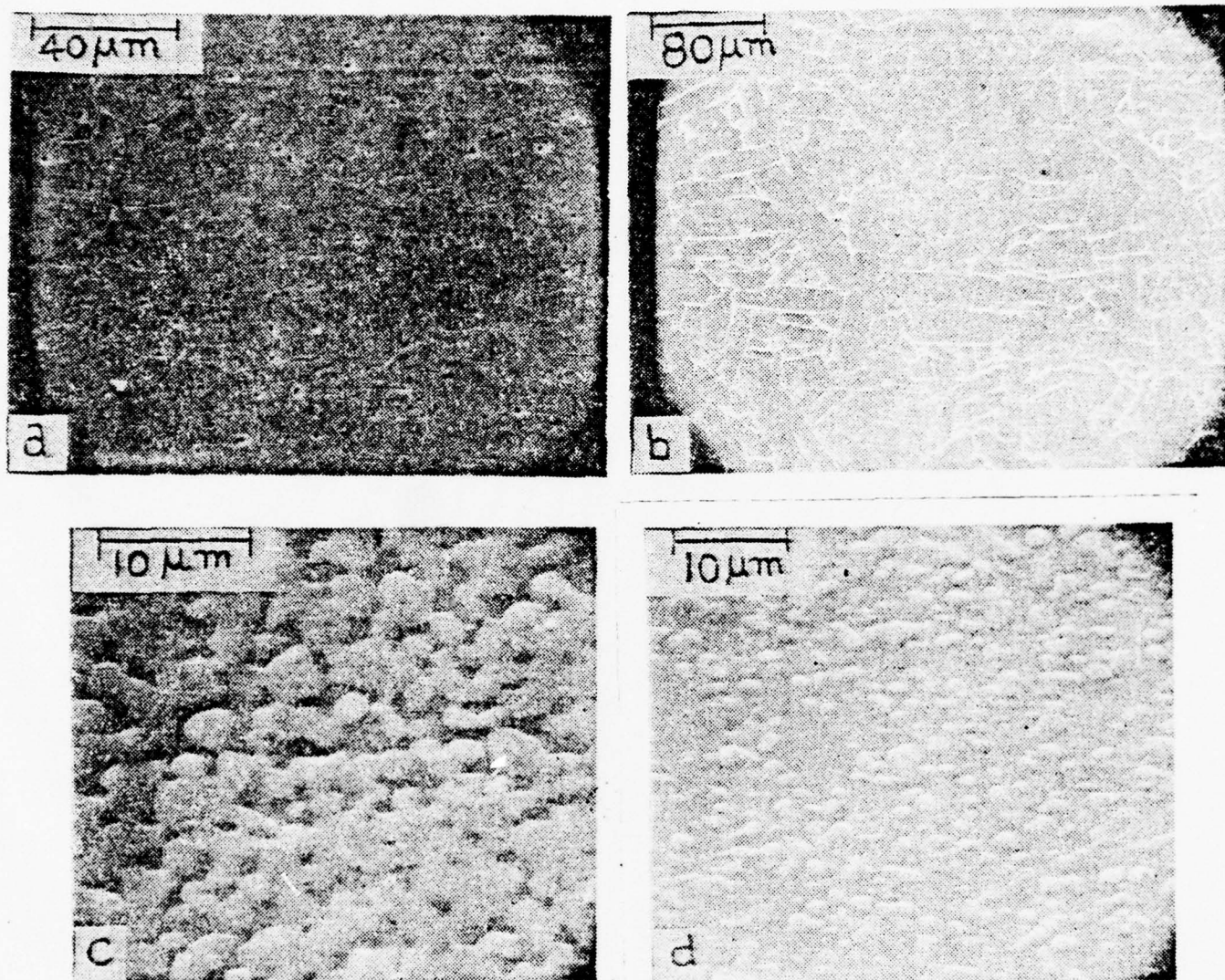
Figure 11. Scanning electron micrographs of polished and etched samples in the Al_2O_3-SiO_2 system: (a) sample #114, pure Al_2O_3, (b) sample #85, 0.5% SiO_2, (c) sample #108, 5% SiO_2 and (d) sample #110, 20% SiO_2.

and Al_2O_3 phases are interpenetrating whereas for 20 wt% SiO_2, the Al_2O_3 phase is discontinuous. Figure 12 presents a comparison of the 5 and 20 wt% SiO_2 samples prepared by relief polishing, chemical etching and thermal etching. The microstructures are most strongly developed by relief polishing although there seems to be some rounding and loss of edge definition in the harder Al_2O_3 phase. Samples with higher SiO_2 contents exhibited non-uniform micro-structures with evidence of discontinuous grain growth. This is illustrated by the micrographs of acid-etched 22 and 24 wt% SiO_2 samples in Fig 13. Table VII presents the quantitative microstructural data calculated from manual counting measurements on the SEM.

Microstructural data obtained for this series of structures should be compared with great caution; the samples examined do not lie along a single path of microstructural change. All were prepared under identical processing conditions, but the initial states of the structures were, of course, different. Thus, it would be misleading, although it is often done, to plot these quantitative microstructural results as a function of composition, and connect the data points in curves that imply a variation of structure with composition. The fact that the processing conditions were identical is the single link between these microstructural states; scientifically, this does not provide a justification for direct comparisons. A real understanding of the context of these structural states would require the determination of the path of microstructural evolution for each starting state, i.e., a series of micro-structural conditions as a function of time for each composition studied. This level of effort was not intended in the present program. The following discussion of these microstructural states is made with this perspective in mind.
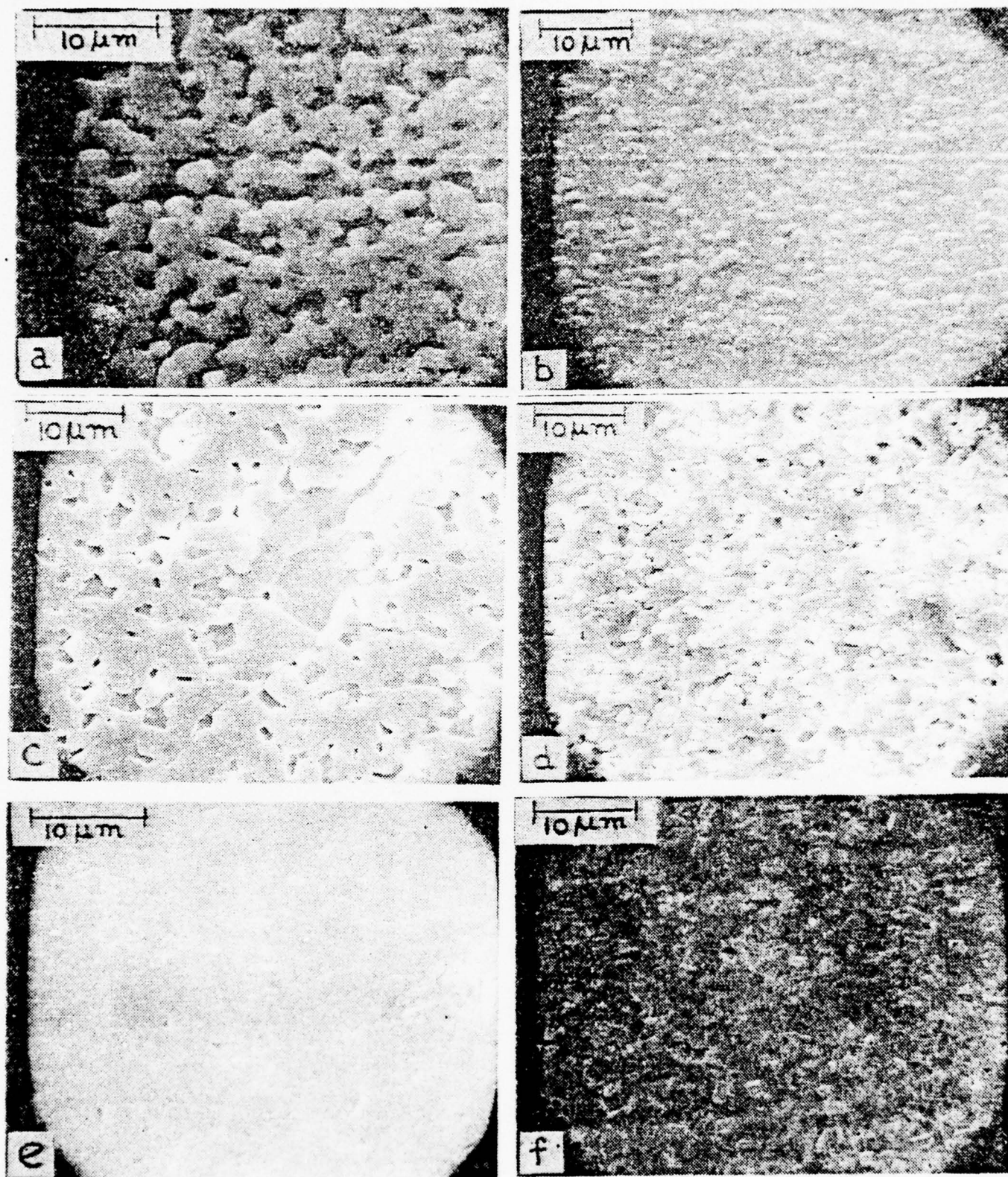
Figure 12. Scanning electron micrographs of 5 weight % (Sample #108) and 20 weight % (Sample #110) SiO₂ samples, prepared by relief polishing (a and b), chemical etching (c and d) and thermal etching (e and f).
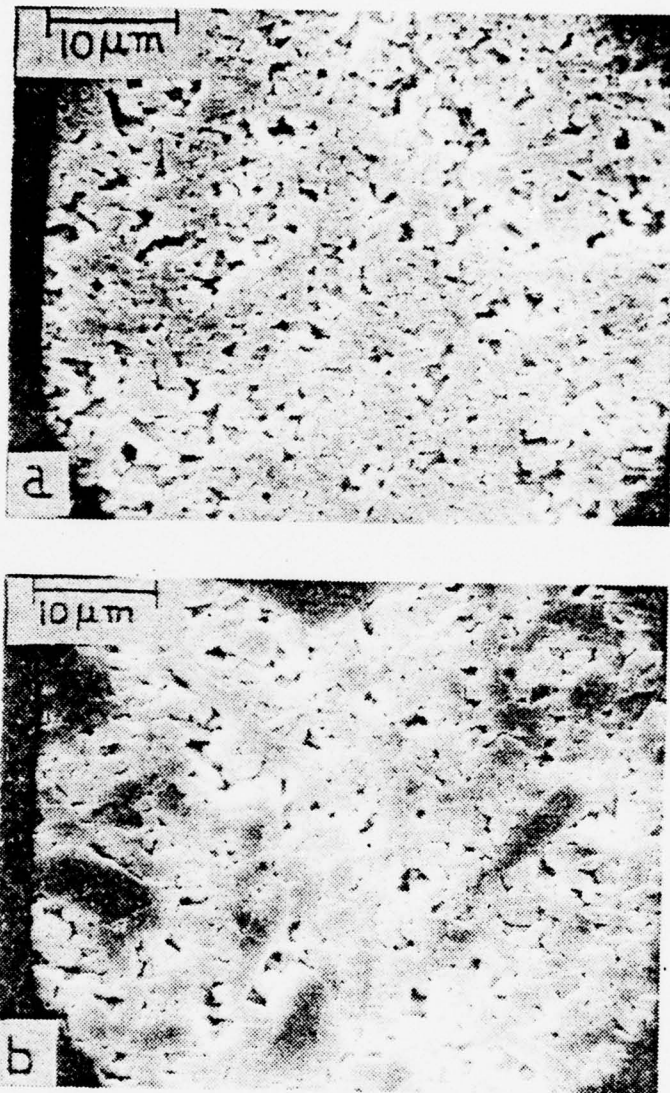
Figure 13. Scanning electron micrographs of polished surfaces etched
            in 49%HF for 3 hours; (a) Al_2O_3 + 22 weight% SiO_2 and
            (b) Al_2O_3 + 24 weight%SiO_2.

Table VII

Quantitative Microstructural Data for Al_2O_3-SiO_2 System

Sample	Weight Fraction SiO_2	Relative Density	V_v^ρ	$\bar{\lambda}^\rho, \mu m$	V_v^β	$S_v^{\alpha\rho}, cm^{-1}$
#114	0.0	98.8	0			1.31×10^2
# 85	0.005	96.4	0.016	1.5		4.20×10^2
#119	0.01	93.4	[Quantitative Microstructural Data could not be obtained due to excessive pull-out in polishing]			
#108	0.05	97.6	0.01		0.26	2.99×10^2
#110	0.20	94.4	0.04	2.5	0.71	–
#130	0.22	93.4	0.05	2.9		
#122	0.239	94.6	0.04	1.4		
#126	0.28	96.0	0.04	0.8		

ρ = pore; α = alumina; and β = mullite

$$\bar{\lambda}_g^\alpha = \frac{4(1-V_v^\rho)}{S_v^{\alpha\rho} + 2S_v^{\alpha\alpha}} \qquad ; \qquad \bar{\lambda}_g^\beta = \frac{4(1-V_v^\rho)}{S_v^{\beta\rho} + 2S_v^{\beta\beta}}$$

Table VII (Cont.)

Sample			$S_v^{\alpha\alpha}$, cm^{-1}	$\bar{\lambda}_g^\alpha$, µm
#114			1.54×10^3	12
# 85			1.53×10^3	11
#119			[Quantitative Microstructural Data could not be obtained due to excessive pull-out in polishing	

Sample	$S_v^{\beta\rho}$, cm^{-1}	$S_v^{\alpha\beta}$, cm^{-1}	$\bar{\lambda}^\alpha$, µm	$\bar{\lambda}^\beta$, µm	$S_v^{\beta\beta}$, cm^{-1}	$\bar{\lambda}_g^\beta$, µm
#108	−	6.11×10^3	4.8	1.7	−	−
#110	6.42×10^2	7.02×10^3	1.4	3.7	−	−
#130	6.96×10^2				1.02×10^4	1.8
#122	1.18×10^3				1.15×10^4	1.6
#126	1.88×10^3				1.64×10^4	1.1

Table VII (Cont).

Sample	$M_v^{\alpha\rho}$, cm^{-2}	$L_v^{\alpha\alpha\rho}$, cm^{-2}	$\dfrac{L_v^{\alpha\alpha\rho}}{M_v^{\alpha\alpha\rho}}$	$L_v^{\alpha\alpha\alpha}$, cm^{-2}
#114	2.74×10^6	6.37×10^5	0.23	1.90×10^6
# 85	9.79×10^6	2.14×10^6	0.22	1.20×10^6
#119				

Sample	$M_v^{\beta\rho}$, cm^{-2}	$M_v^{\alpha\beta}$, cm^{-2}	$L_v^{\beta\beta\rho}$, cm^{-2}	$\dfrac{L_v^{\beta\beta\rho}}{M_v^{\beta\rho}}$	$L_v^{\beta\beta\beta}$, cm^{-2}
#108	2.57×10^7	4.65×10^7	-	-	-
#110	2.02×10^7	$M_v^{\beta\alpha}$, cm^{-2} 8.76×10^7	-	-	-
#130	4.54×10^7		2.83×10^7	0.62	3.66×10^7
#122	3.04×10^7		2.75×10^7	0.90	4.58×10^7
#126	1.21×10^8		9.36×10^7	0.77	1.83×10^8

Although minor additions of silica to alumina clearly slow the rate of densification attainable(Figure 10),the effect upon the path of microstructural evolution is not so clear. The low value of the ratio $L_V^{\alpha\alpha\rho}/M_V^{\alpha\rho}$ indicates that there is much less of a tendency for the porosity to be located at the grain edges in these structures as compared to those discussed previously,(Fig. 8).

The structures obtained at the high silica end, which are nearly 100% mullite, are much finer than those at the alumina end; the grain size is an order of magnitude smaller,(Table VII). At the same time, these structures exhibit values of the ratio of $L_V^{\beta\beta\rho}/M_V^{\beta\rho}$ which are essentially in line with those observed in hot pressed pure alumina,(Figure 8). Thus, in the hot pressed and sintered mullite structures, the porosity also lies primarily along the triple lines in the mullite grain network.

The two examples of the two-phased structures(#108 and #110)qualitatively are mirror images of each other. In the low mullite case(#108), the mean intercept of the alumina is about four times that of the mullite; in the high mullite sample,(#110), the reverse is true. While the volume fractions essentially exchange values in going from one sample to the other, the surface areas remain the same. The primary difference in the exchange is the value of M_V, which is about twice as large in the predominantly mullite sample as it is in the other case. This larger value of M_V, for two structures that have the same volume fraction and the same scale, indicates, but by itself does not demonstrate, that the high mullite structure is disconnected, i.e., is an array of separate alumina particles dispersed in a mullite matrix. The low mullite structure is a network structure, with both phases interpenetrating.

Although it is necessary to be cautious in describing the effect of concentration on microstructural evolution on the basis of these isolated microstructural states, it is possible to infer at least a plausible description from this information. As silica is added, the relative amount of mullite is of course increased as required by the phase diagram. As silica is added, under similar processing conditions, the mullite phase forms an interconnected network at relatively low volume fractions, perhaps reflecting a tendency to appear along alumuna grain edges in the parent structure. At higher mullite contents, the alumina grains become disconnected from each other, again perhaps reflecting the tendency for mullite to spread on the alumina grain boundaries. The structures that are essentially all mullite are significantly finer than the alumina structures at the other end of the composition range. This observation probably reflects the fact that the silica powder used in these studies is much finer than the alumina powder. However, to obtain a clear idea of how this final state comes about, it would be necessary to follow the path for this composition from the beginning.

Dielectric Properties of Hot-Pressed Alumina and Alumina-Silica:

1500°C-1000psi-t Specimens: Figures 14-20 present plots of log σ_{AC} versus $10^3/T$ at applied frequencies of 200 Hz to 20 KHz for this entire series of microstructures. Figures 21-24 gives K' and K" data as a function of inverse temperature for the end members of the 1500°C-1000psi-t series. Above about 700°C the results for all samples are within the range of values reported in the literature.[34-36] The most remarkable feature is the discontinuity in the conductivity curves which occurs for the samples with highest $V_V^{porosity}$ values. Considering for example sample 90, the conductivity drops with increasing temperature, reaching values below the range of the bridge around 600-700°C; at higher temperatures the conductivity reading is again
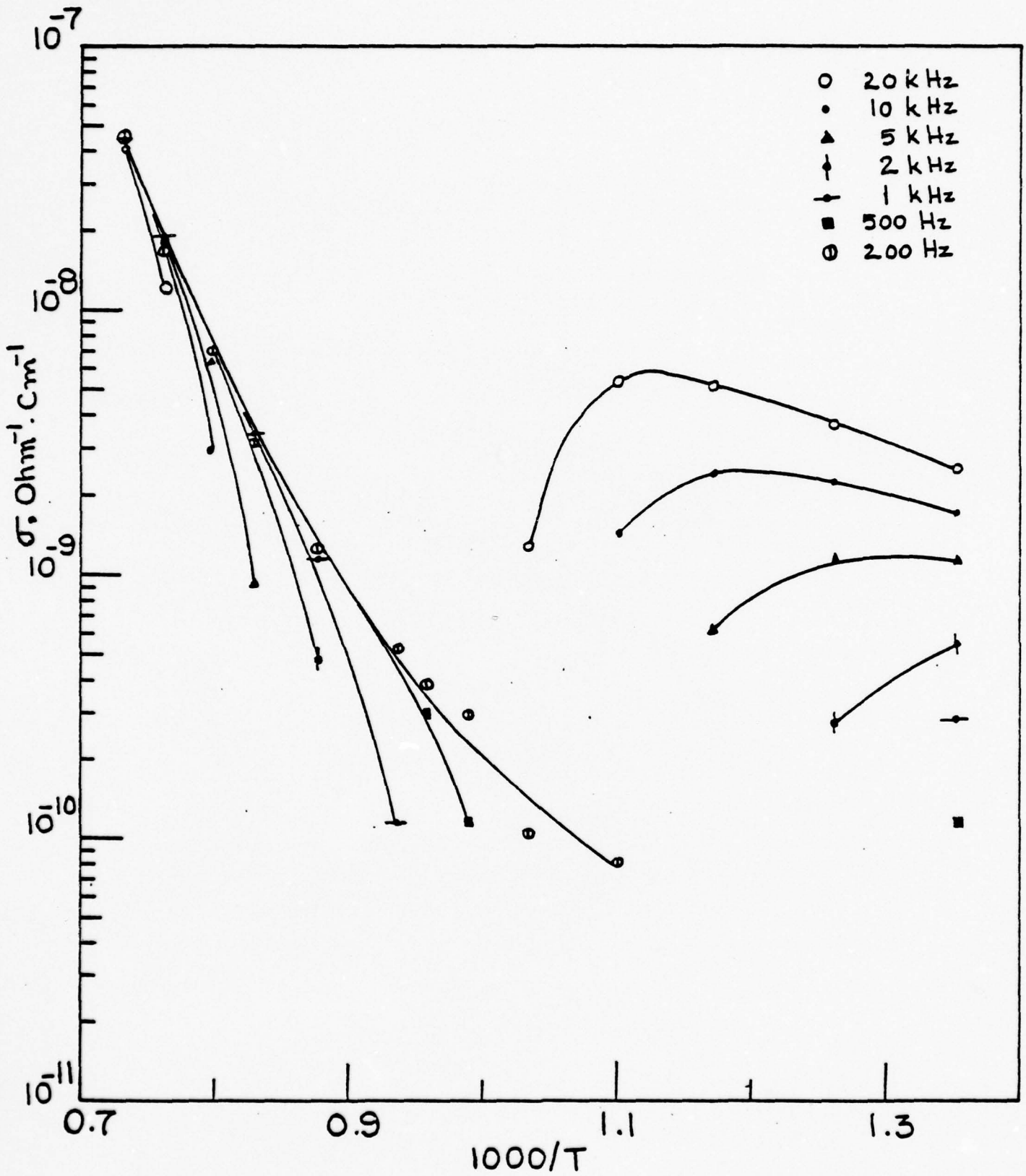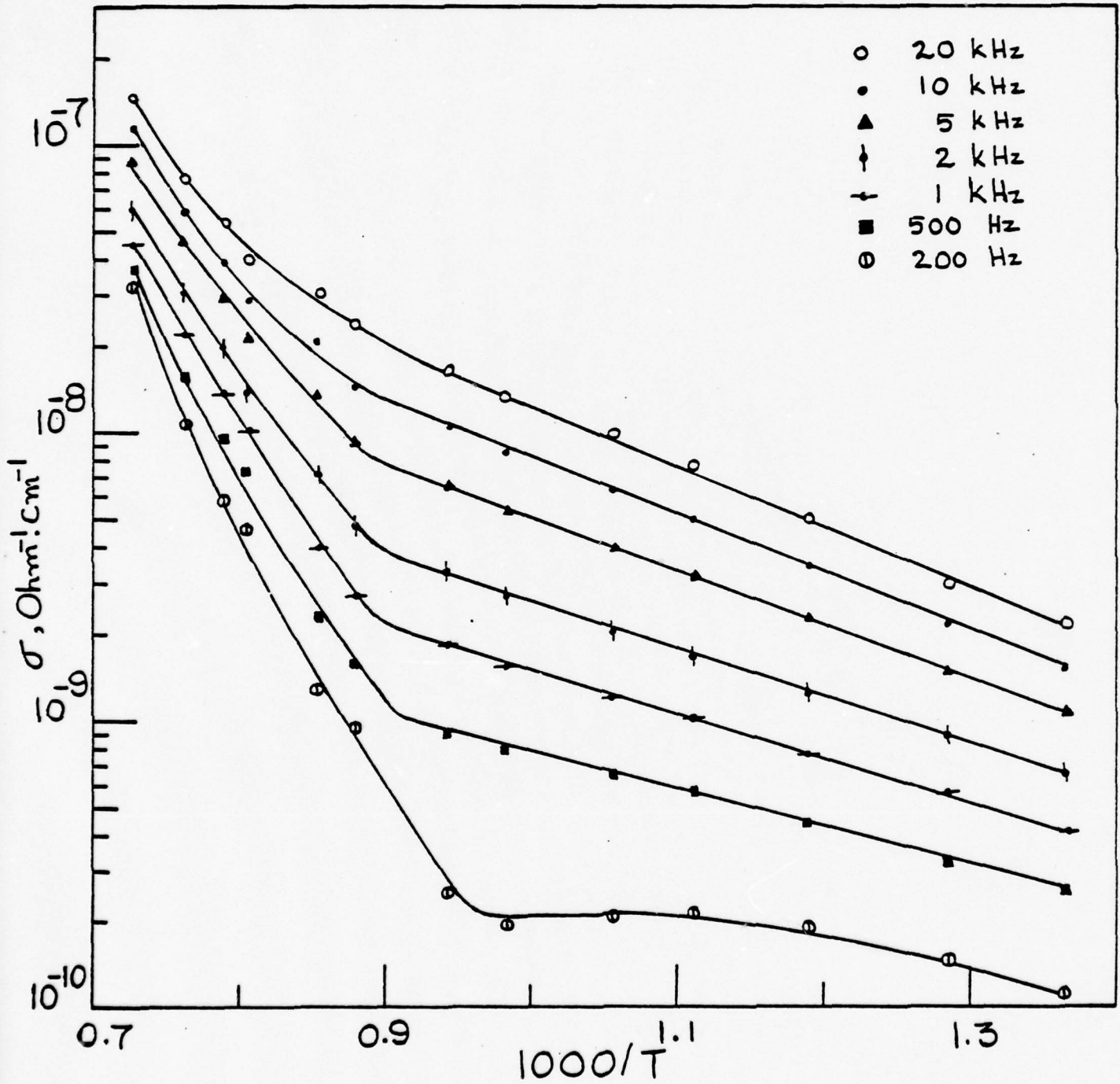
Figure 14. Plot of the electrical conductivity versus reciprocal temperatrue of sample (#90) hot pressed at 1500°C-1000psi-0 minutes.
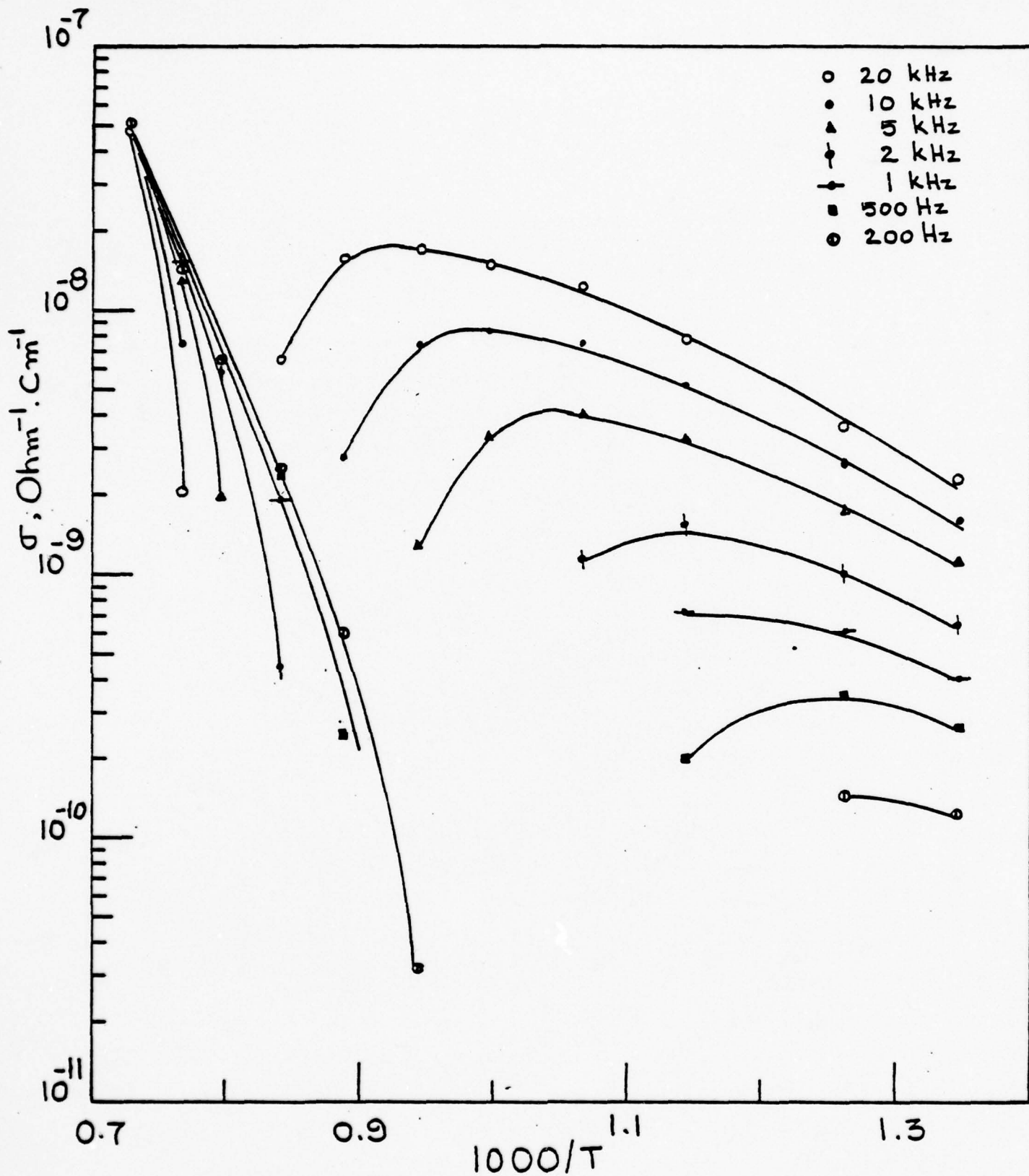
Figure 15. Plot of the electrical conductivity versus reciprocal temperature of sample (#98) hot pressed at 1500°C-1000psi-7 minutes.
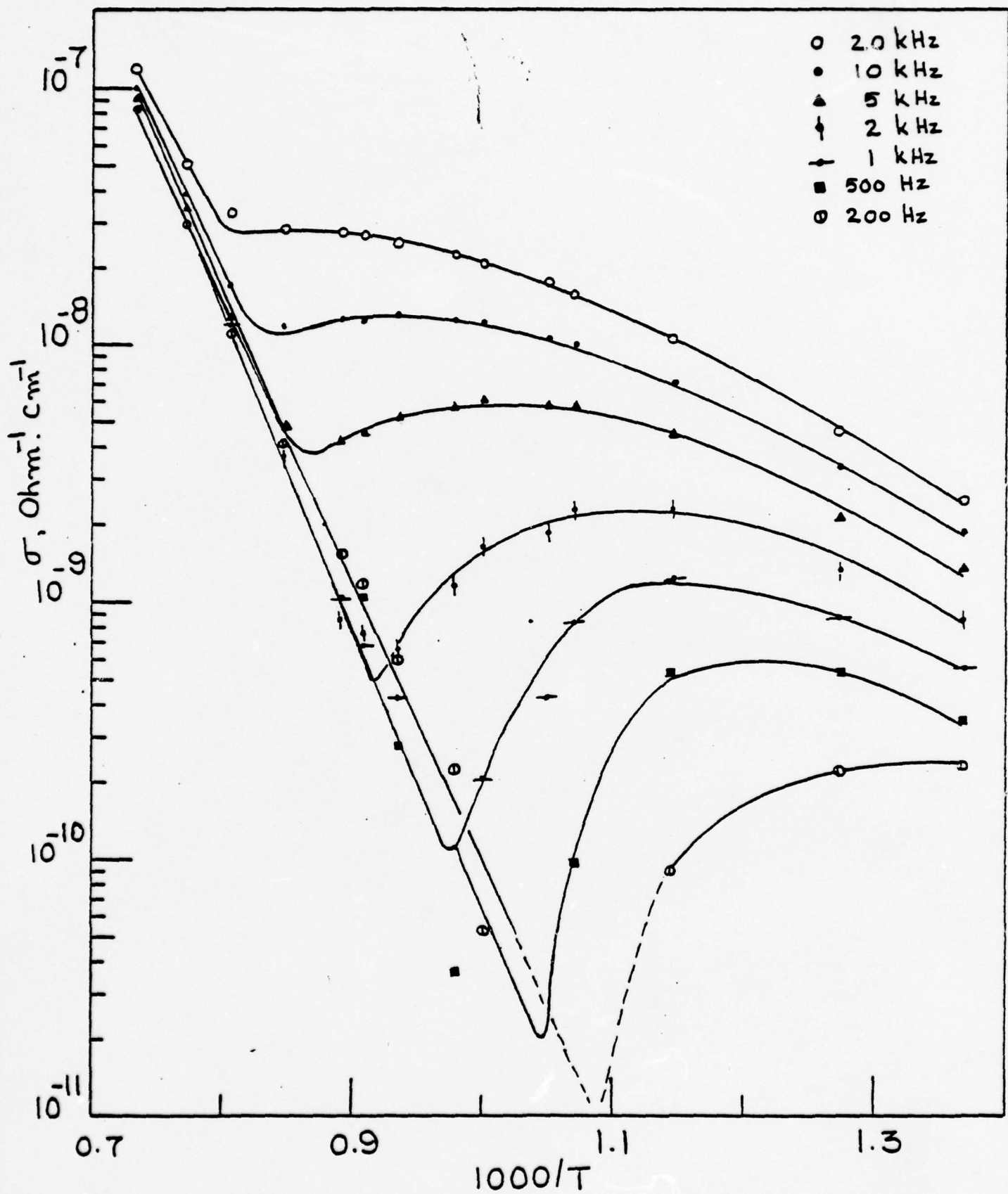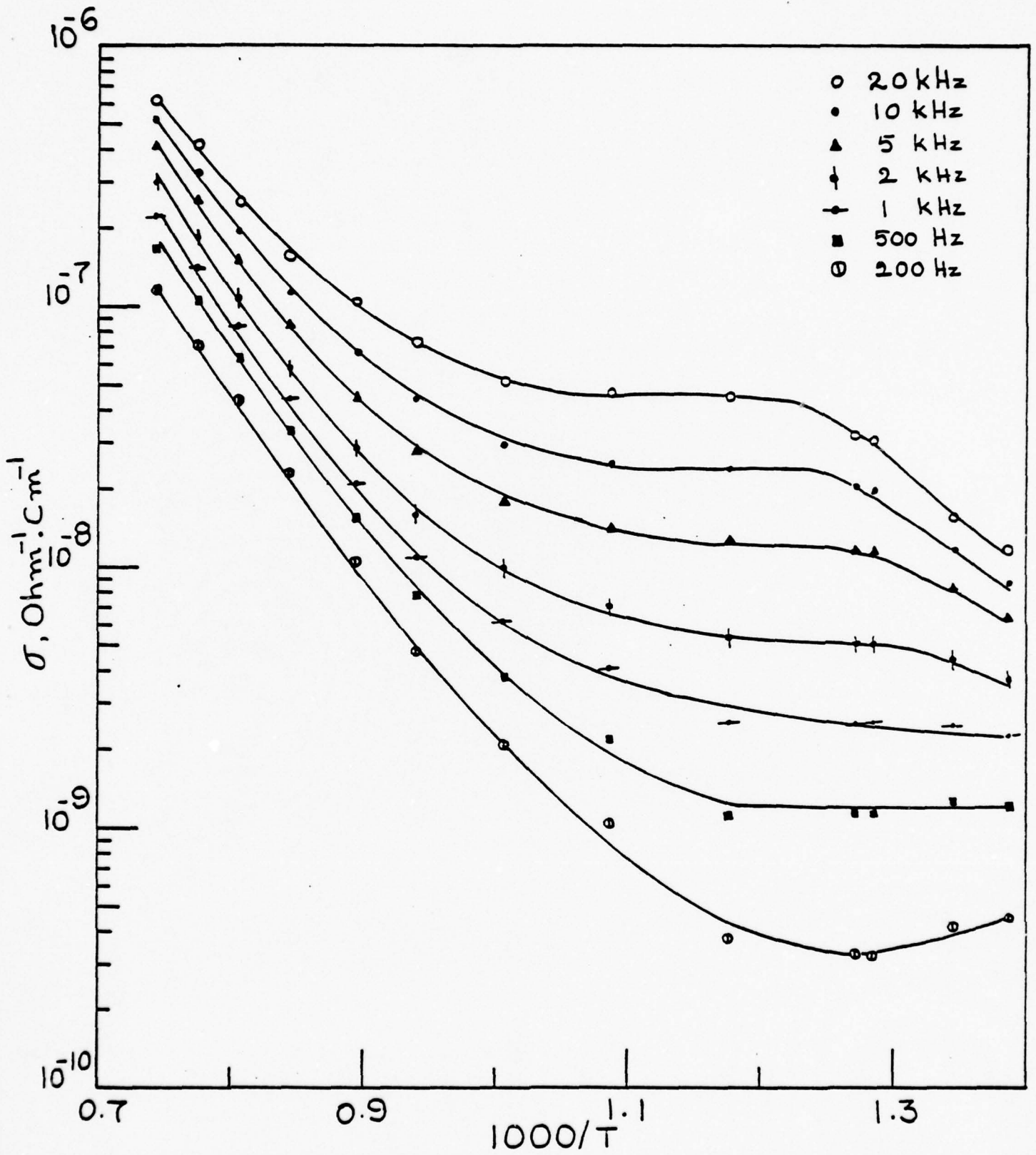
Figure 16. Plot of the electrical conductivity versus reciprocal temperature of sample (#99) hot pressed at 1500°C-1000psi-15 minutes.
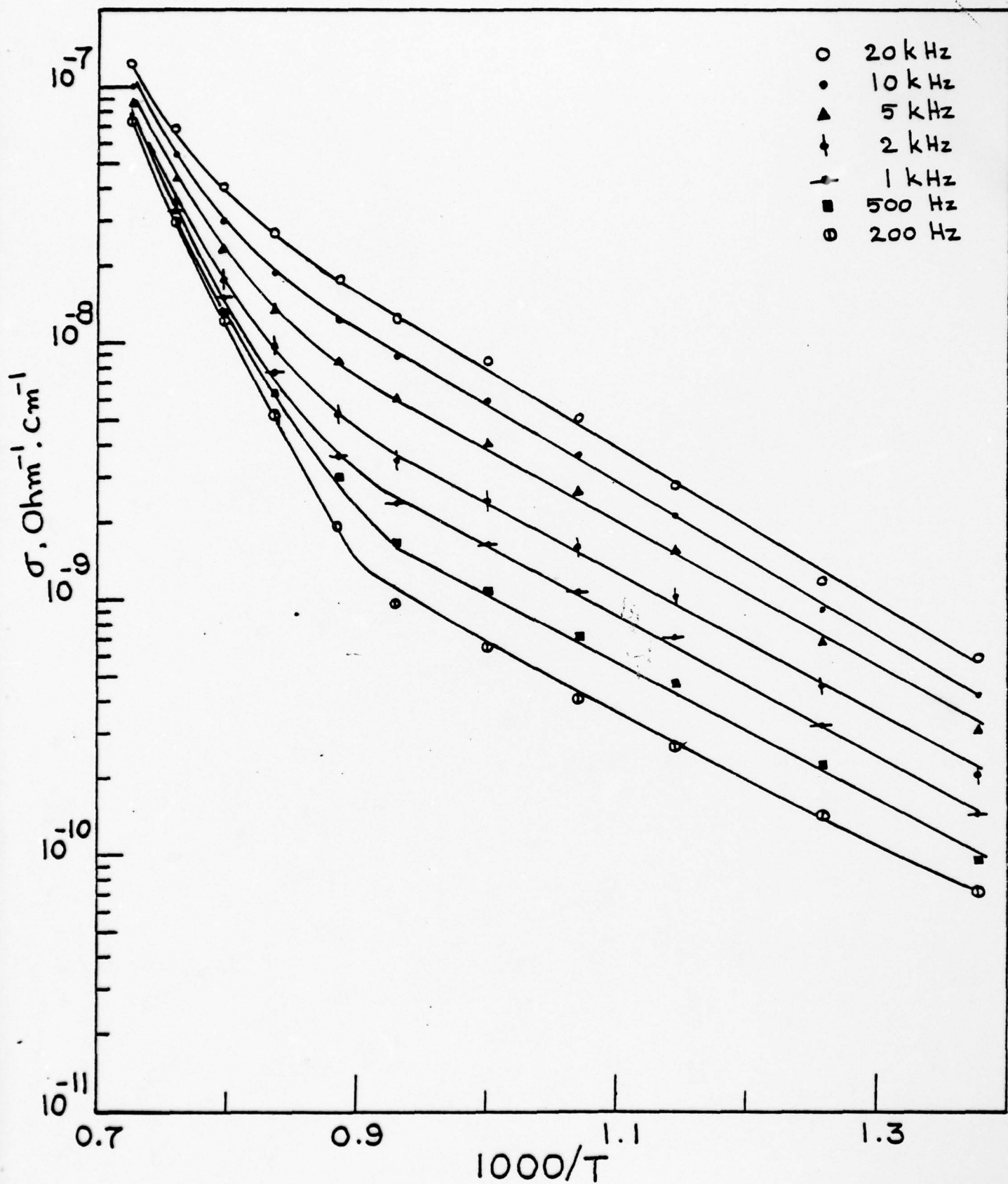
Figure 17. Plot of the electrical conductivity versus reciprocal temperature of sample (#91) hot pressed at 1500°C-1000psi-30 minutes.
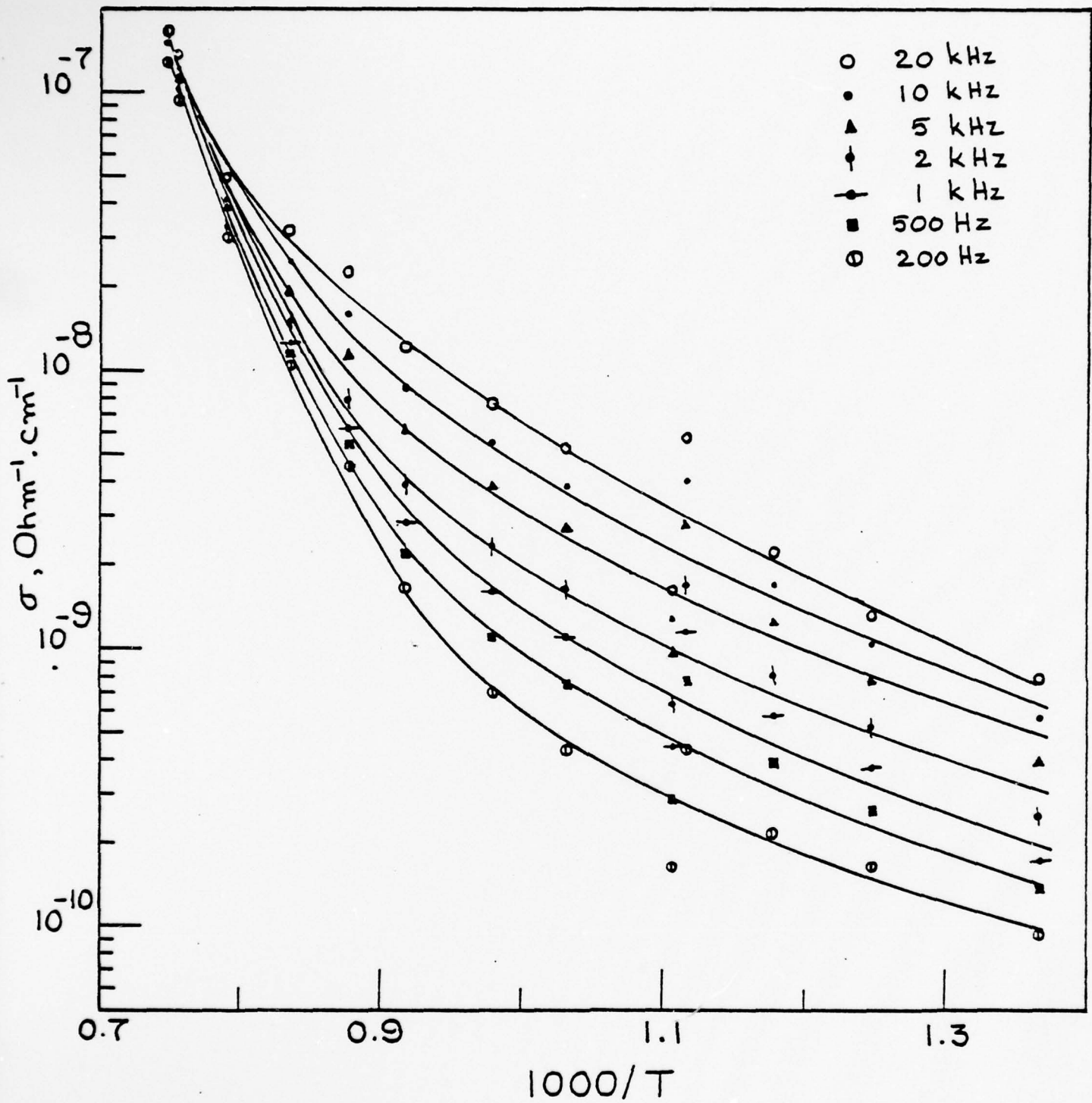
Figure 18. Plot of the electrical conductivity versus reciprocal temperature of sample (134) hot pressed at 1500°C-1000psi-45 minutes.

Figure 19. Plot of the electrical conductivity versus reciprocal temperature of sample (#92) hot pressed at 1500°C-1000psi-60 minutes.

Figure 20. Plot of the electrical conductivity versus reciprocal temperature of Sample (#93) hot pressed at 1500°C-1000psi-120 minutes.
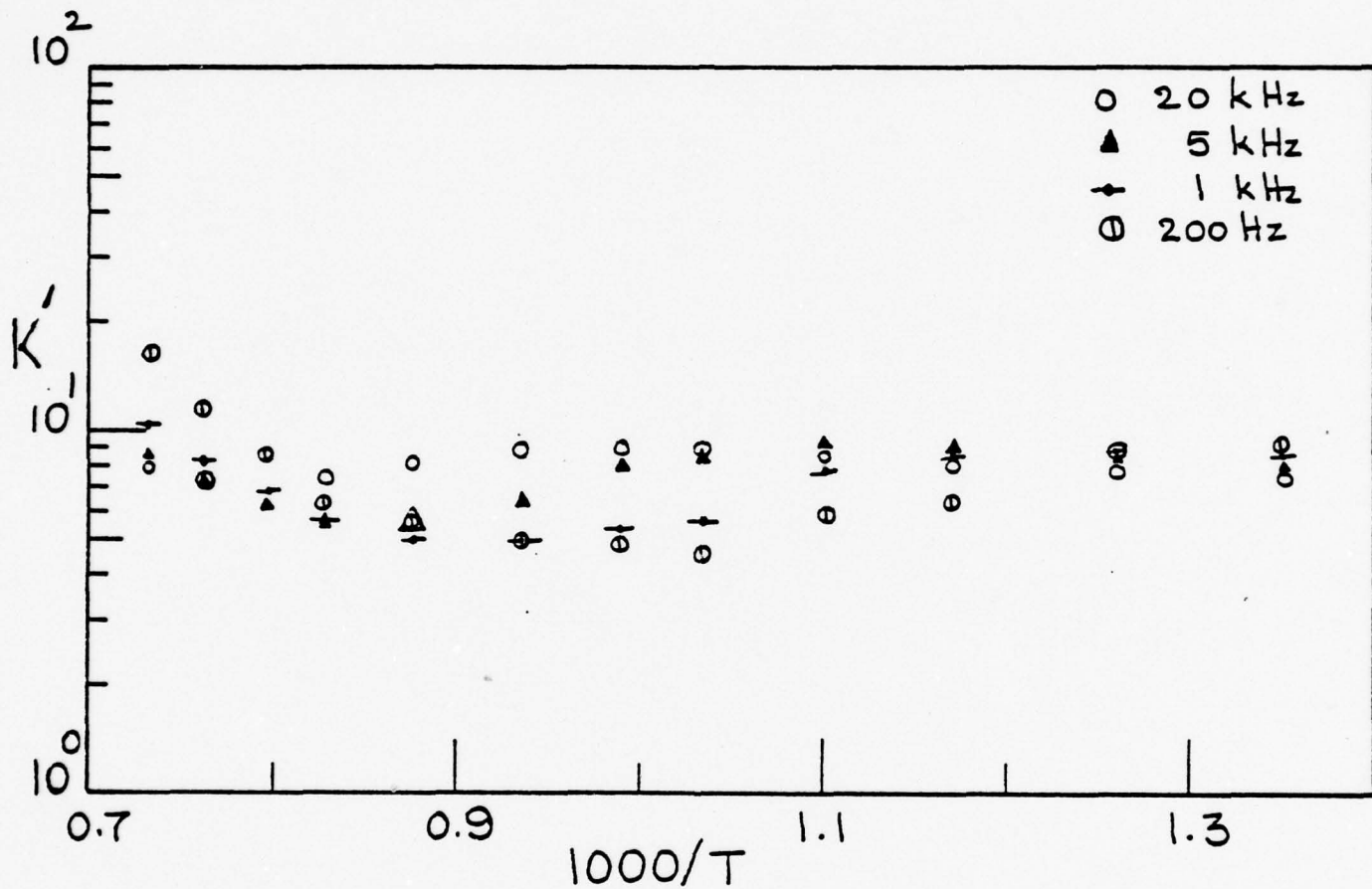
Figure 21. Plot of the relative dielectric constant (K') versus reciprocal
temperature of sample (#90) hot pressed at 1500°C-1000psi-
0 minutes.
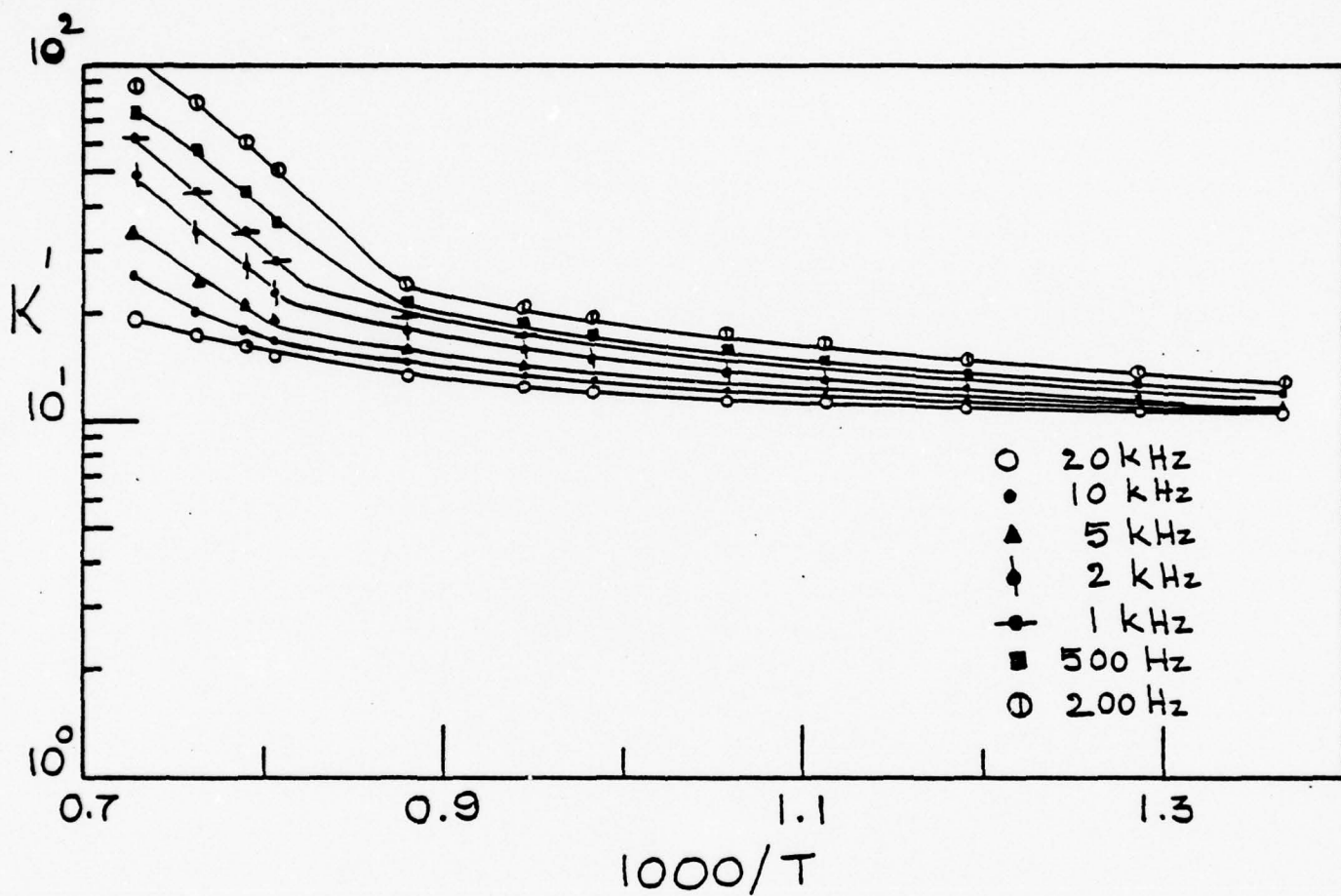
Figure 22. Plot of the relative dielectric constant (K') versus reciprocal
temperature of sample (#92), hot pressed at 1500°C-1000psi-
60 minutes.
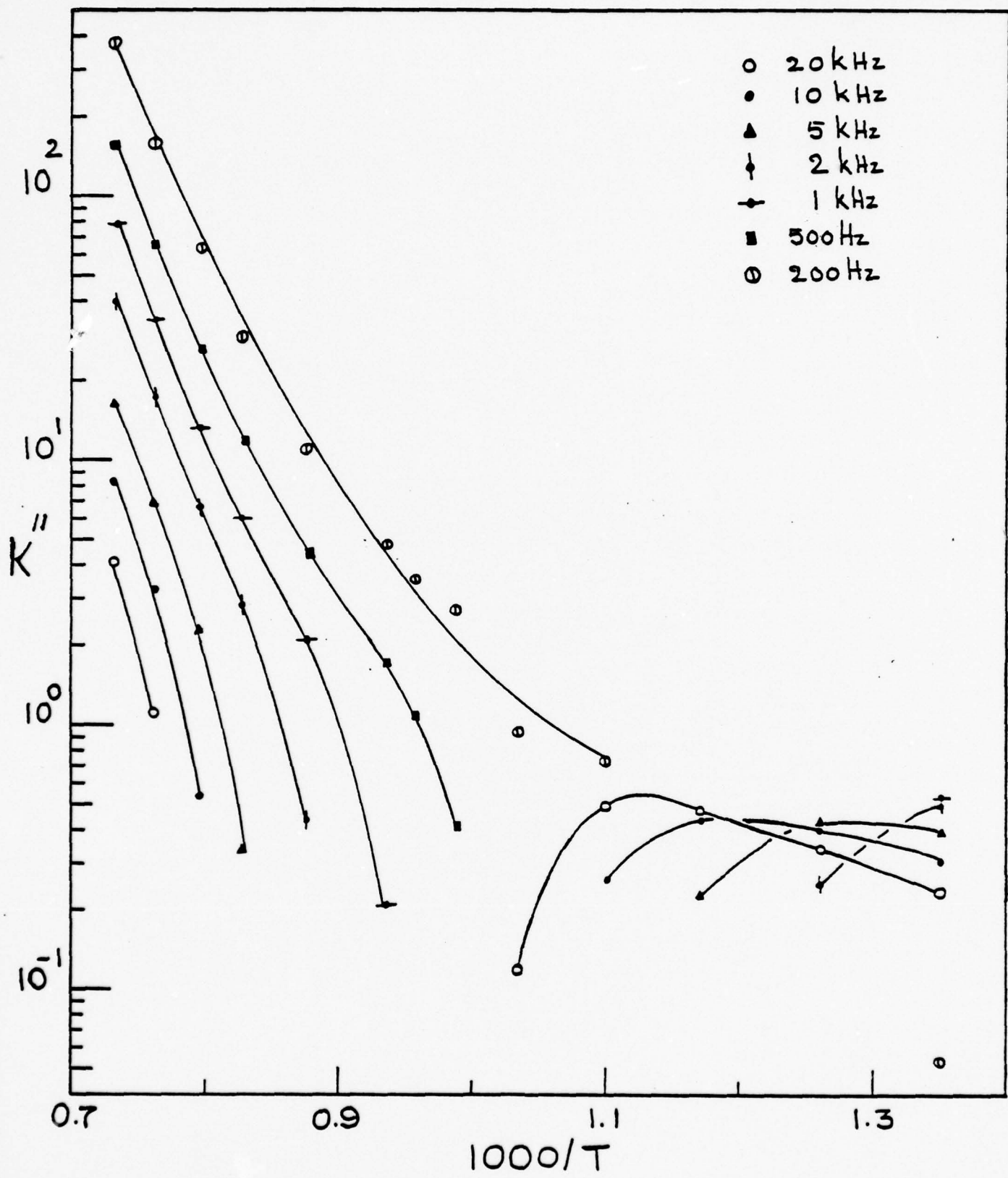
Figure 23. Plot of the loss factor (K") versus reciprocal temperature of sample (#90) hot pressed at 1500°C-1000psi-0 minutes.
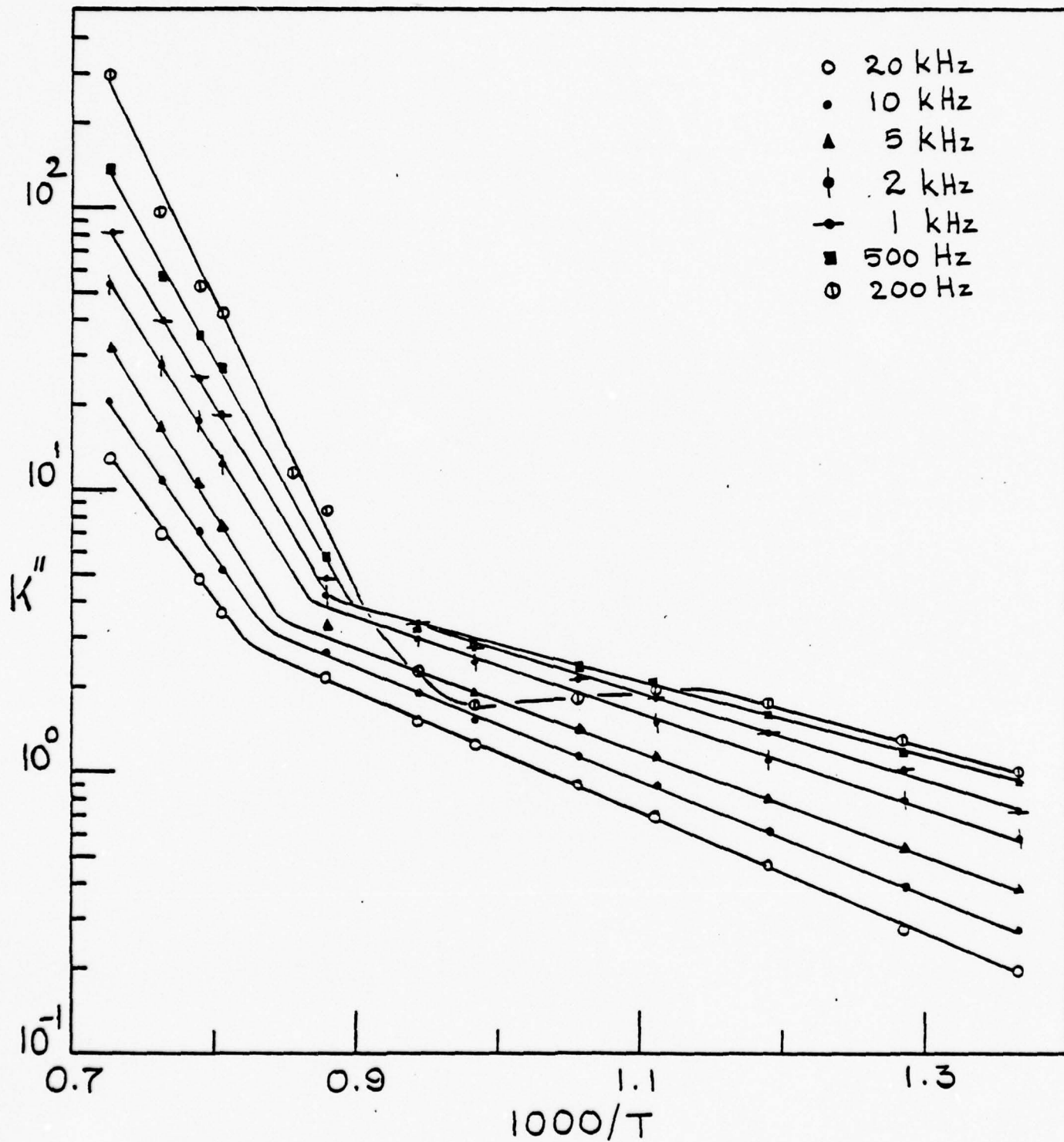
Figure 24. Plot of the loss factor (K'') versus reciprocal temperature of sample (#92) hot pressed at 1500°C-1000psi-60 minutes.

on-scale and the data behave normally. The temperature at which the discontinuity appears increases with measuring frequency; the effect becomes progressively weaker with decreasing $V_V^{porosity}$ and is absent for samples 91, 134, 92, and 93. The discontinuity clearly seems to be microstructurally related since it always occurs in samples which have been sintered for short times and have high $V_V^{porosity}$ and is absent otherwise.

1400°C-2000psi-t Specimens: The log σ_{AC} vs $10^3/T$ plots for these samples are presented in Fig. 25-28. The curves for the samples are virtually identical to each other and to samples sintered 30 min or longer in the 1500°C-1000psi-t series.

$Al_2O_3-SiO_2$ Specimens: Dielectric data for the samples are given in Figs. 29-35. The conductivity of the 0.5 weight % silica sample at the highest temperature measured is half-an-order of magnitude higher than that of pure alumina made under identical conditions. The magnitude of the conductivity drops with increasing silica fraction, as can be seen in Fig. 29 and 30. The high-temperature conductivity of the samples also exhibits a dependence on silica content that is qualitatively similar to that observed for the relative density. In addition, the intermediate temperature conductivity discontinuity is observed in the 500-900°C temperature range for the 5 and 20 wt % silica samples, respectively. The discontinuity is reproducible from sample to sample with different electrodes as long as the sample composition falls in the right range. The discontinuity disappears and the conductivity increases progressively through the compositions of 22, 24 and 28% silica, as can be seen in Figs. 33-35. At 28% silica, the conductivity vs. reciprocal temperature curve is again similar to that of 0.5 or 1% silica sample, though the magnitude of the conductivity is not the same.
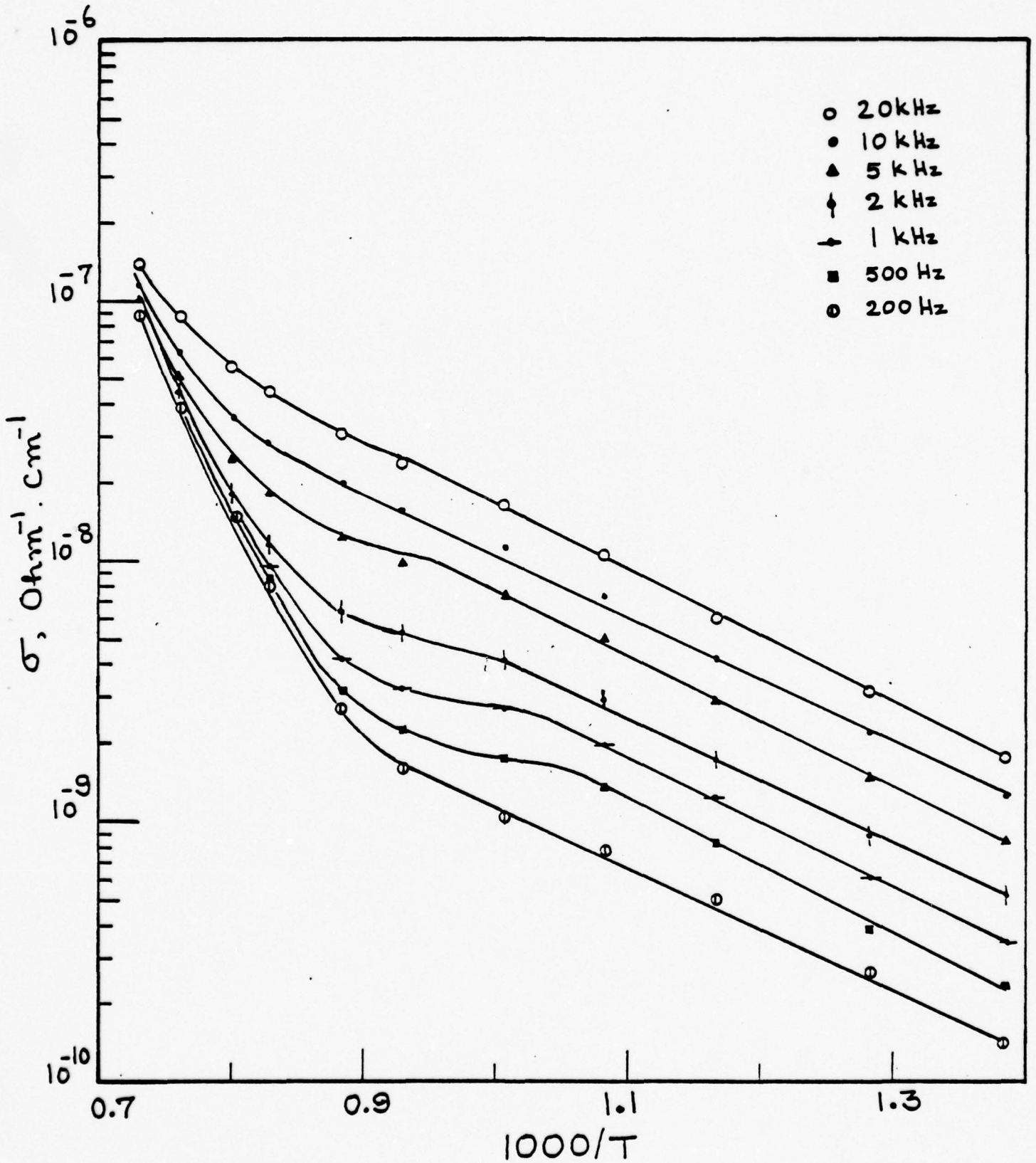
Figure 25. Plot of the electrical conductivity versus reciprocal temperature of sample (#105) hot pressed at 1400°C-2000psi-15 minutes.
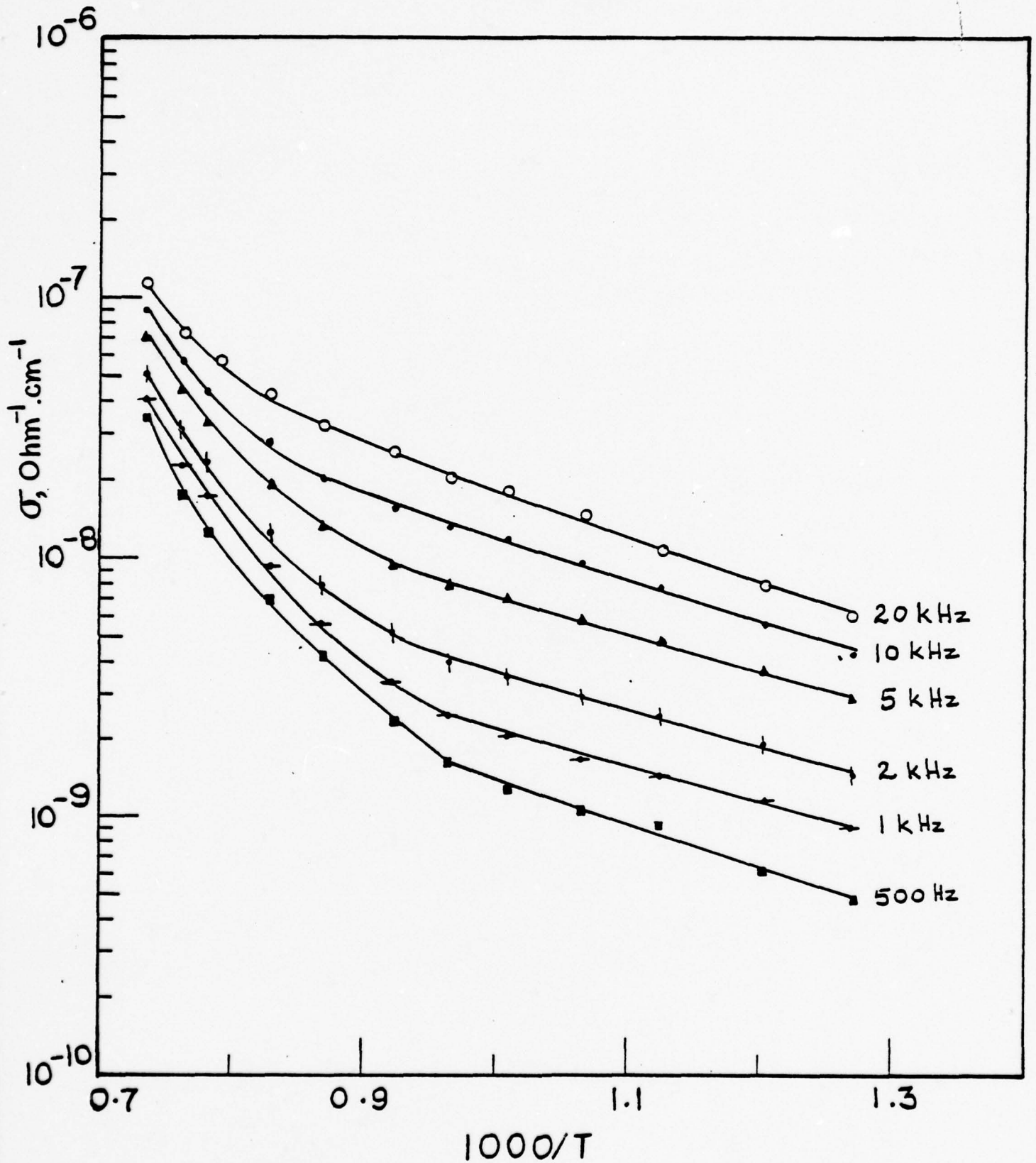
Figure 26. Plot of the electrical conductivity versus reciprocal temperature of sample (#75) hot pressed at 1400°C-2000psi-30 minutes.
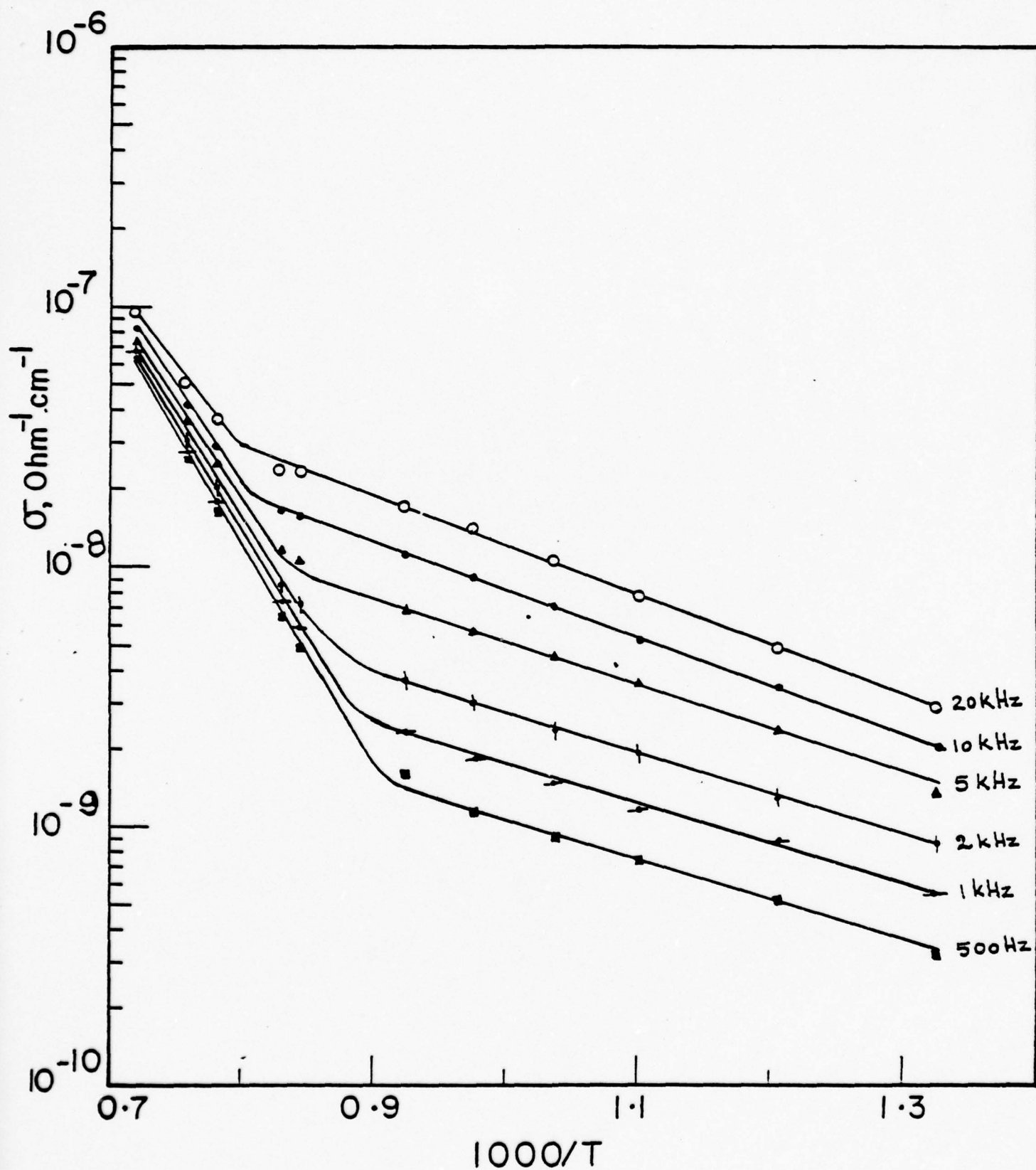
Figure 27. Plot of the electrical conductivity versus reciprocal temperature of sample (#78) hot pressed at 1400°C-2000psi-60 minutes.
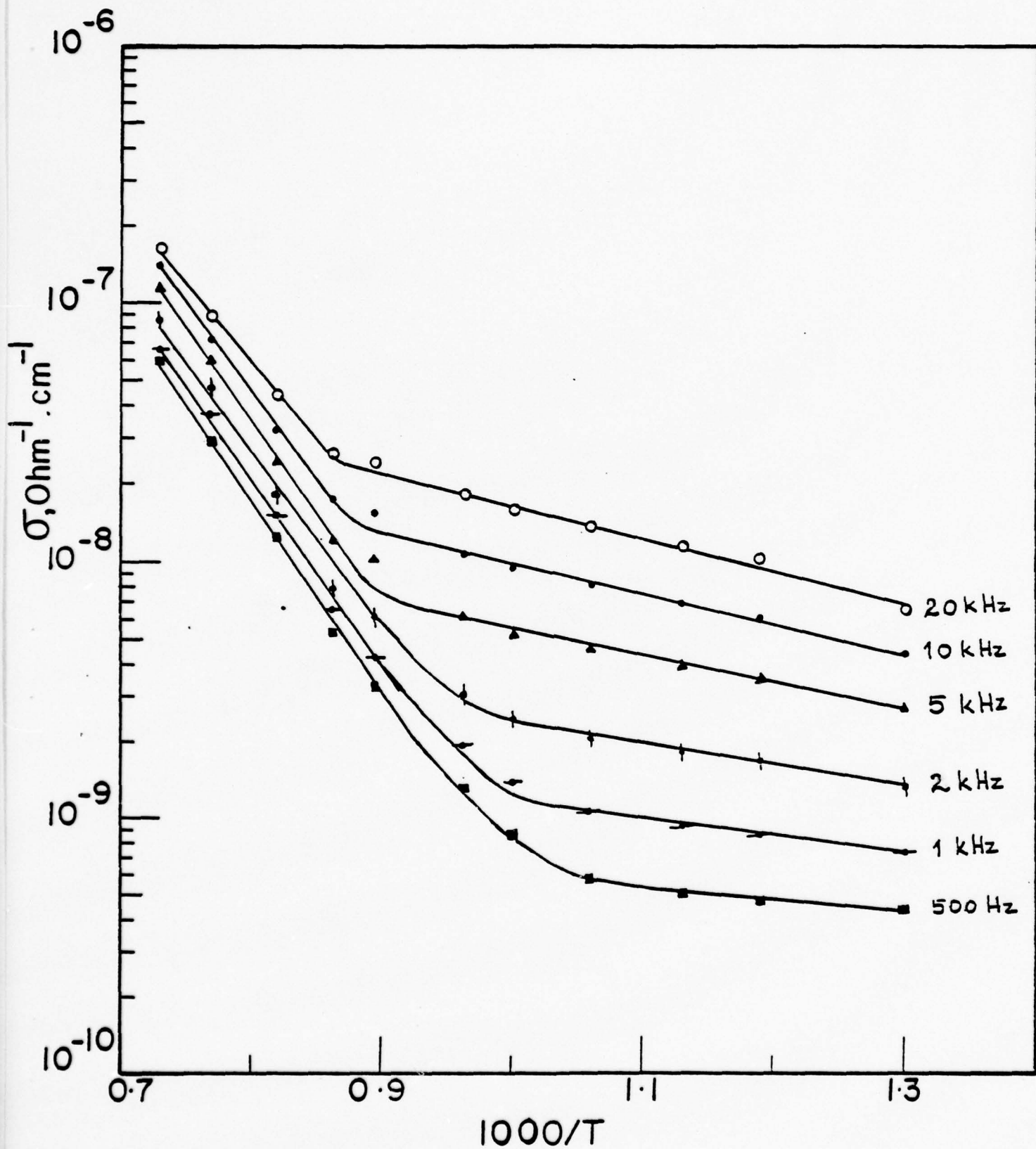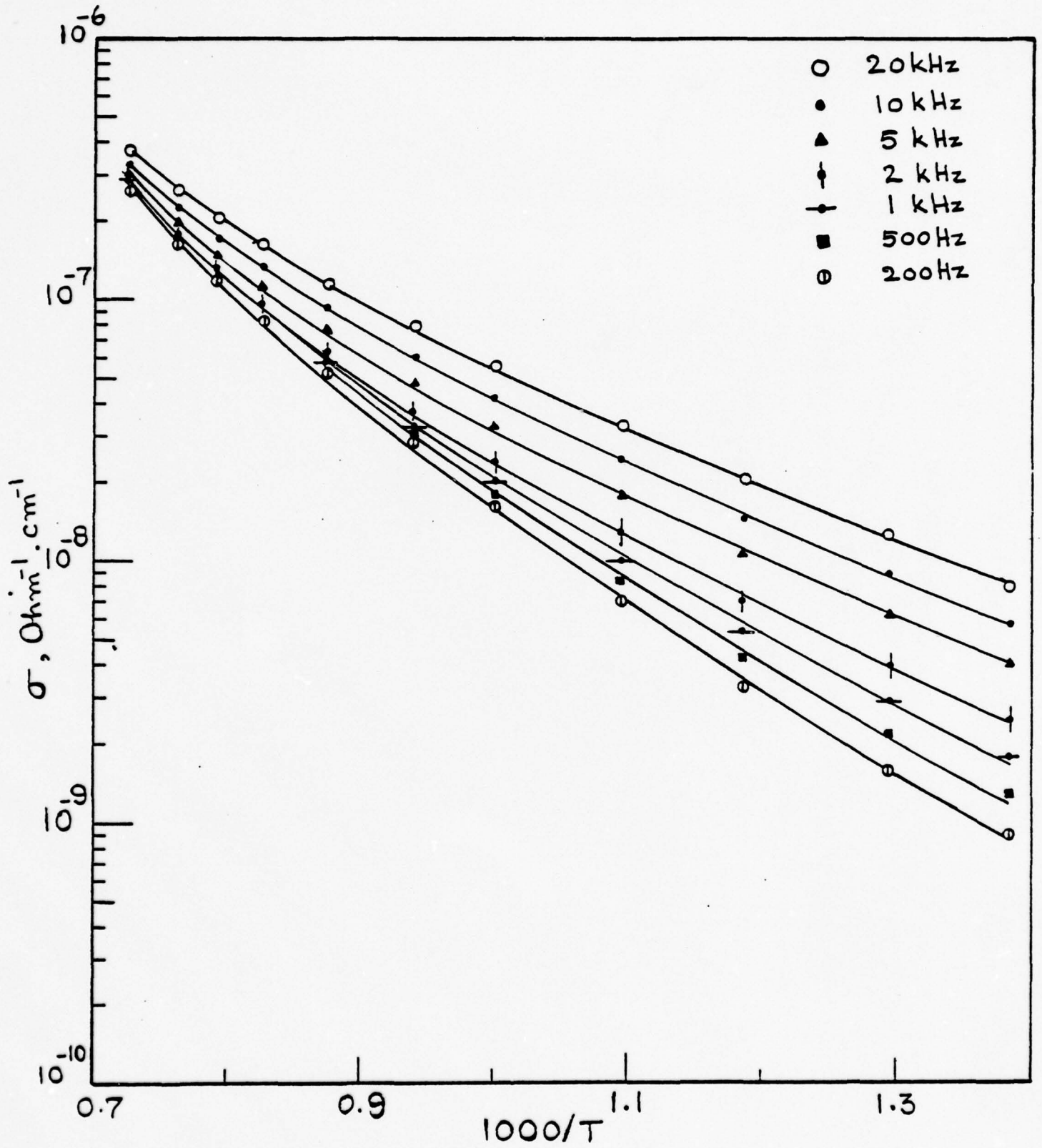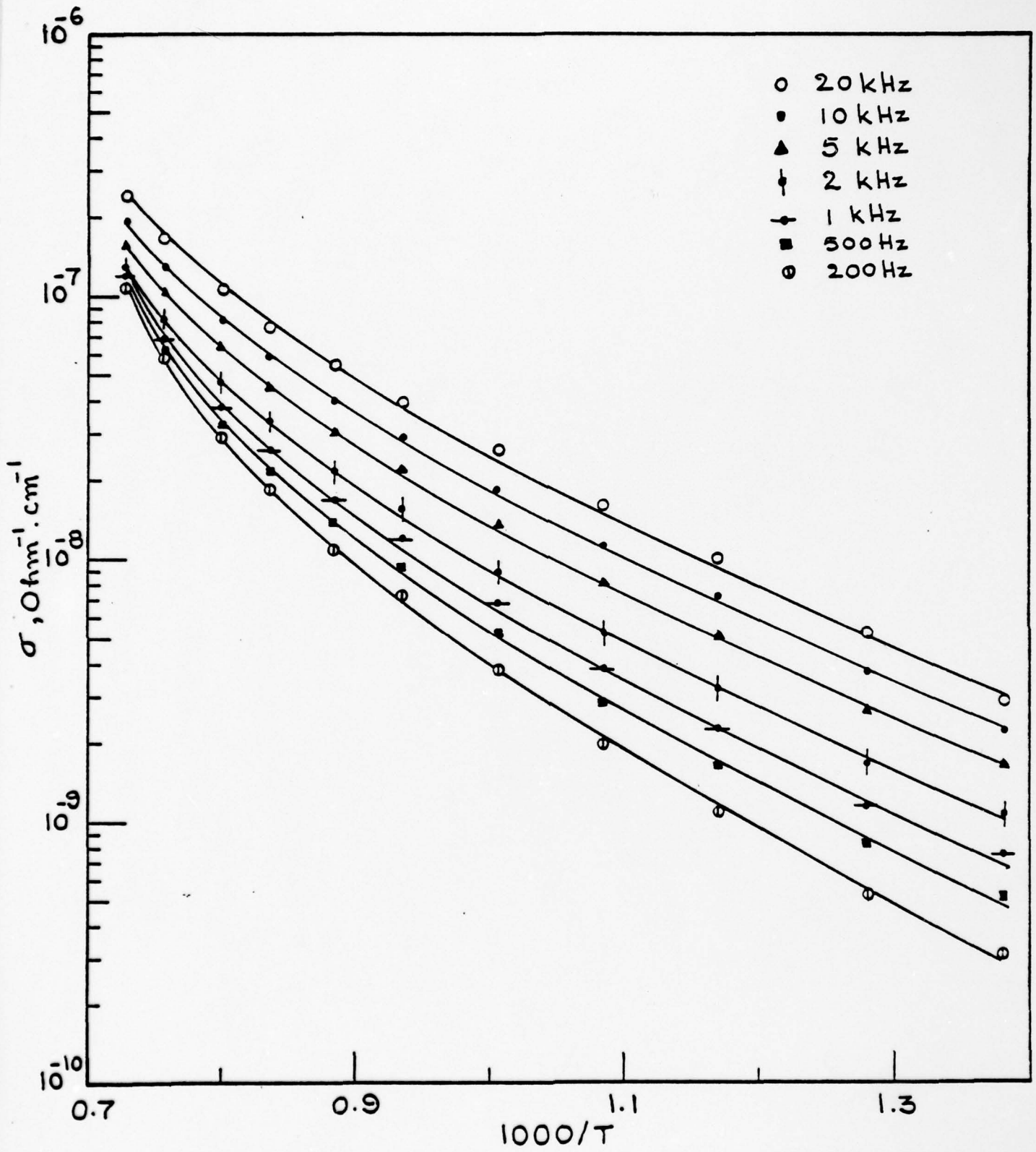
Figure 28. Plot of the electrical conductivity versus reciprocal temperature of sample (#77) hot pressed at 1400°C-2000psi-90 minutes.
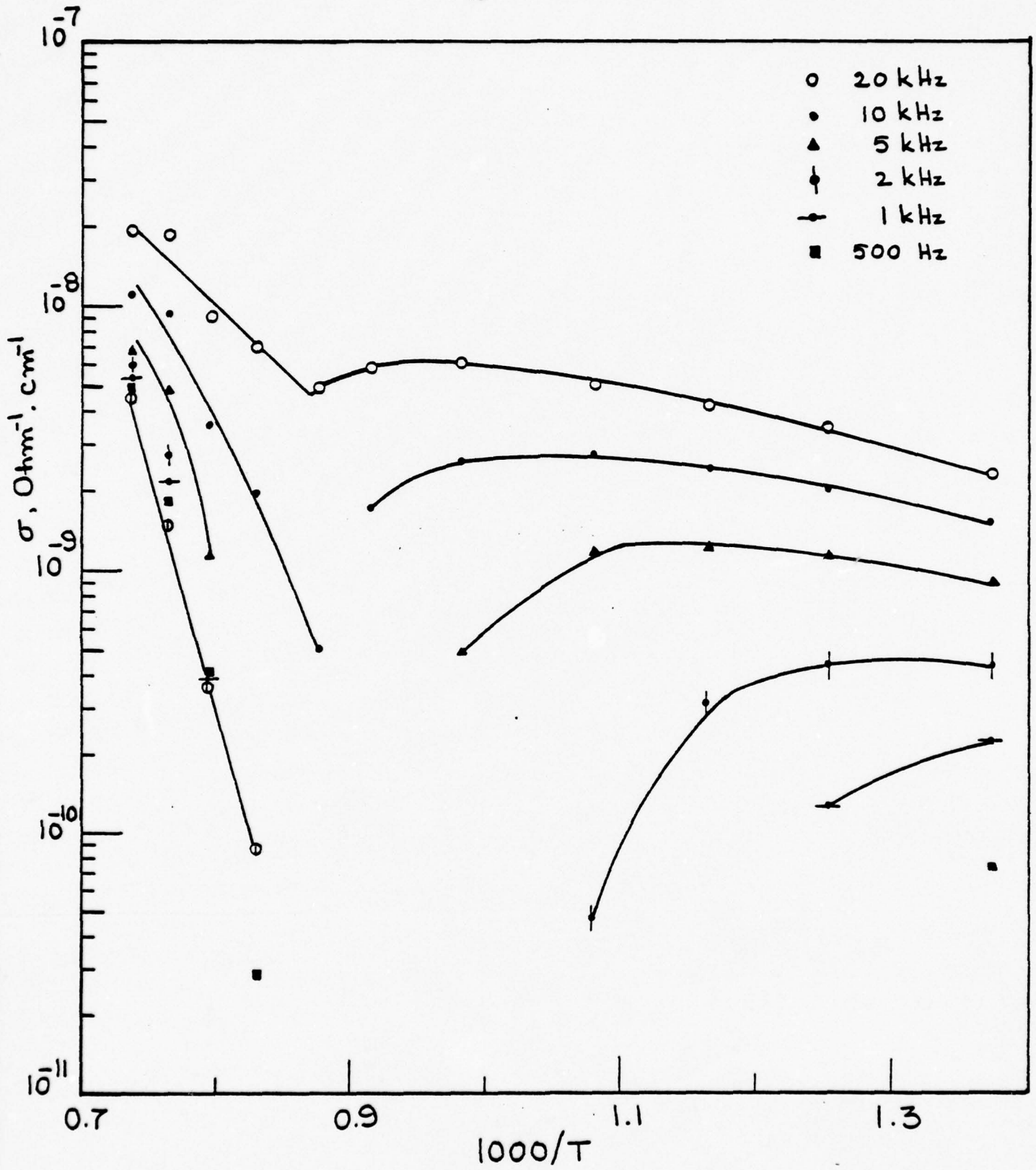
Figure 29. Plot of the electrical conductivity versus reciprocal temperature of sample (#85) with 0.5% SiO$_2$.

Figure 30. Plot of the electrical conductivity versus reciprocal
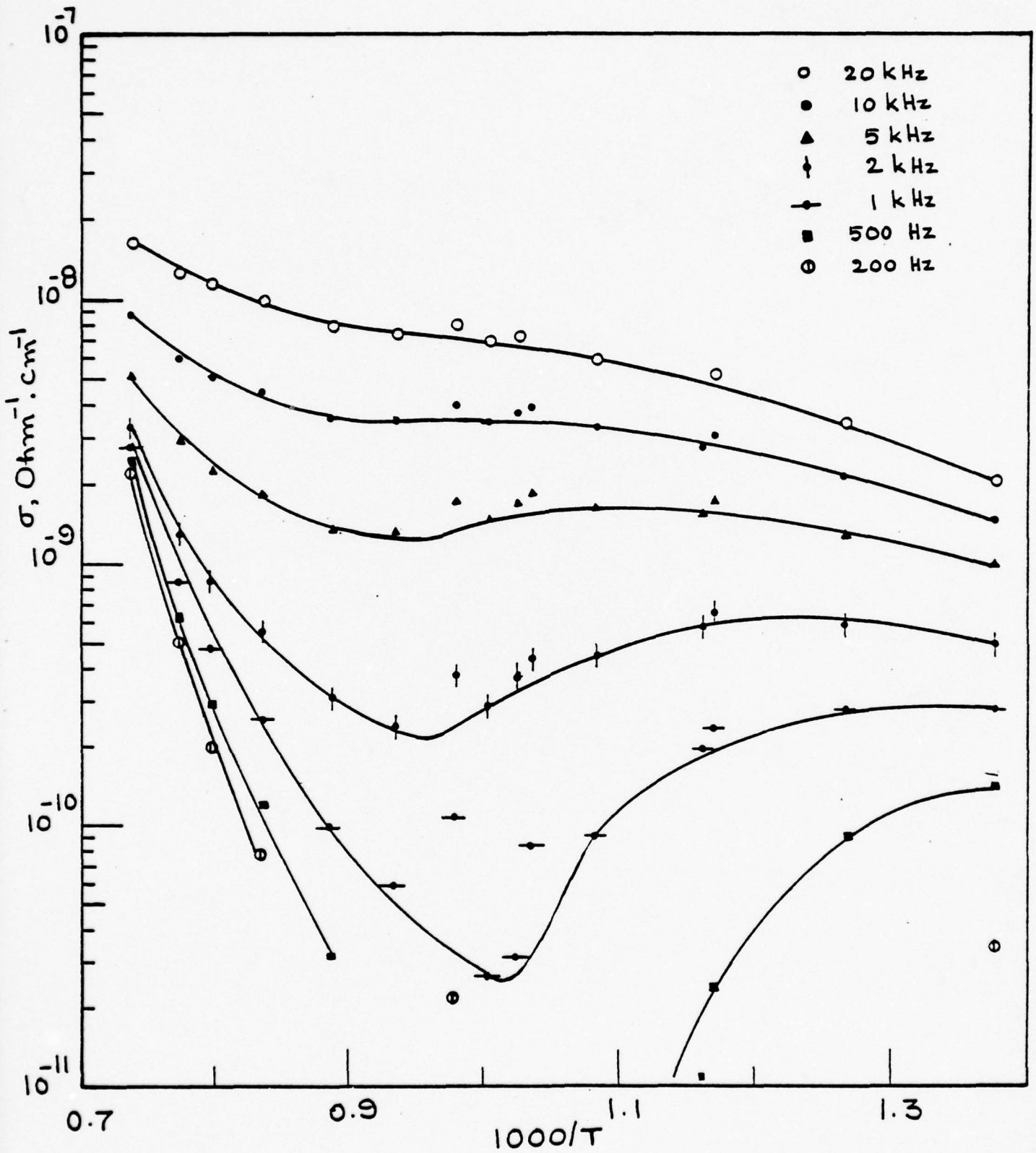temperature of sample (#119) with 1% SiO_2.
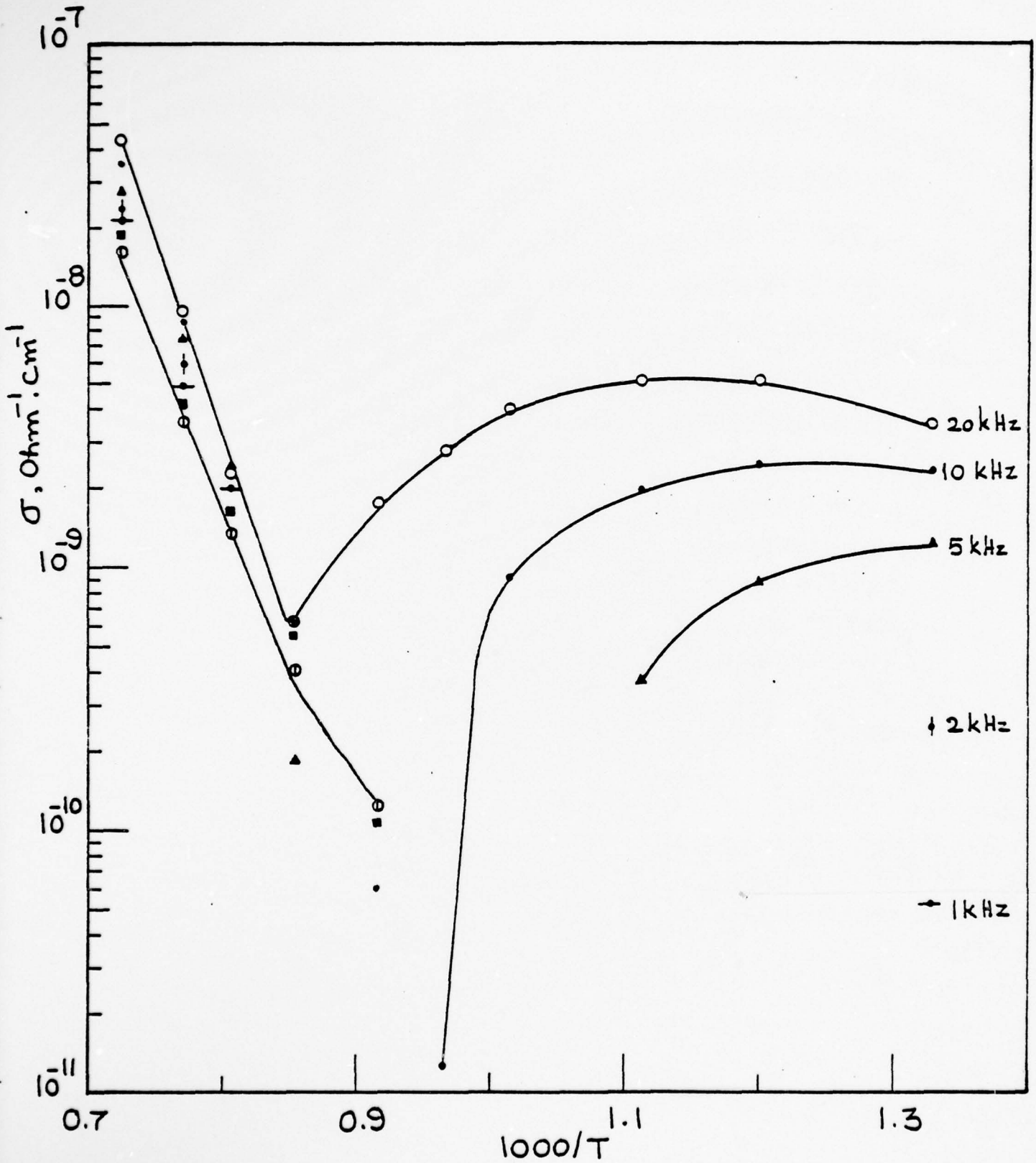
Figure 31. Plot of the electrical conductivity versus reciprocal temperature of sample (#108) with 5% SiO$_2$.

Figure 32. Plot of the electrical conductivity versus reciprocal temperature of sample (#110) with 20% SiO_2.

Figure 33. Plot of the electrical conductivity versus reciprocal
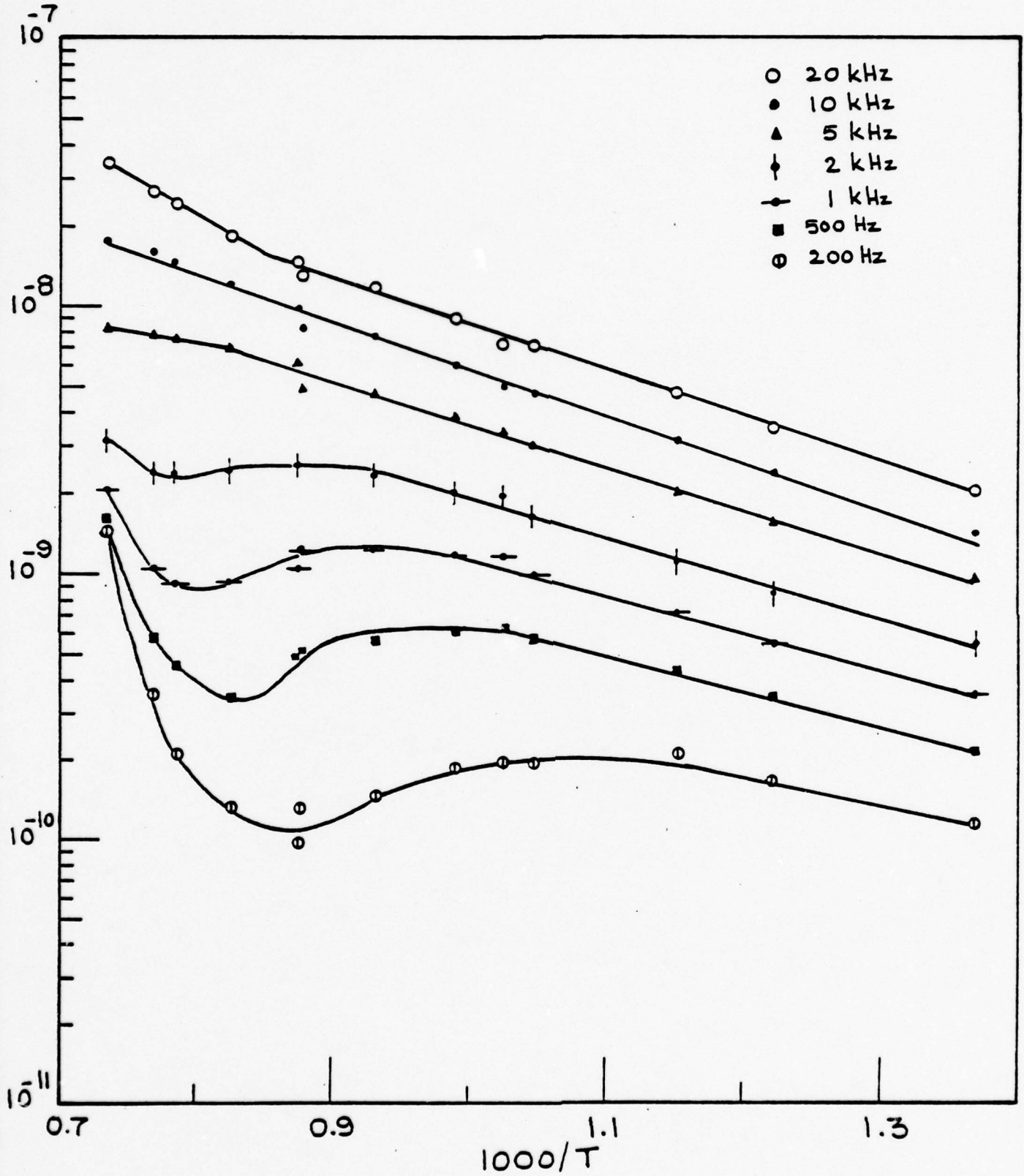temperature of sample (#130) with 22% SiO_2.

Figure 34. Plot of the electrical conductivity versus reciprocal temperature of sample (#122) with 24% SiO_2.
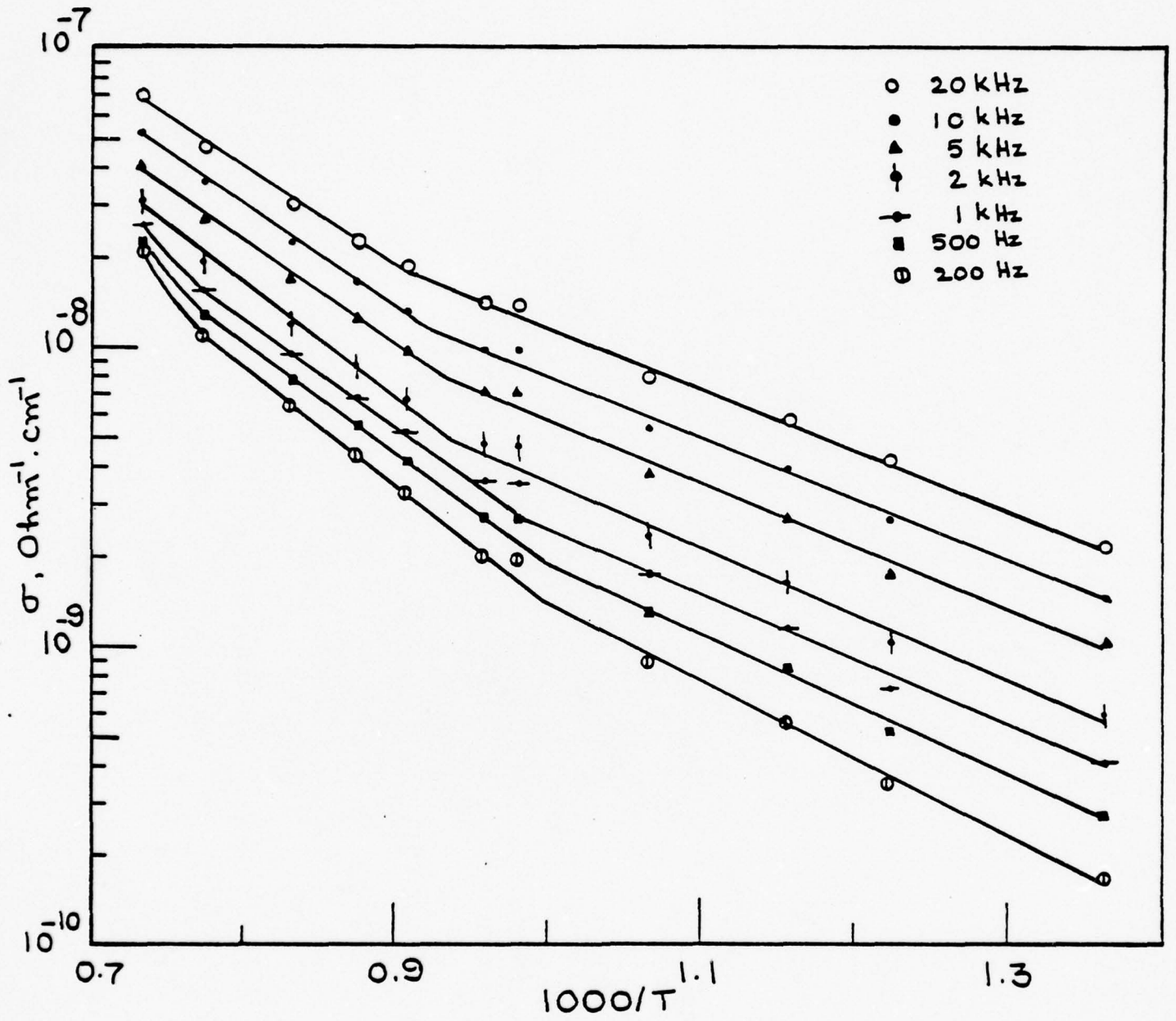
Figure 35. Plot of the electrical conductivity versus reciprocal temperature of sample (#126) with 28% SiO_2.

Microstructure-Electrical Property Correlations

1500°C-1000psi-t Series: Figures 36-41 show the variation of AC conductivity and dielectric constant with V_V^{pore}, the volume fraction of porosity, for a range of temperatures at applied frequencies of 0.2, 2 and 20 KHz. At lower temperatures there is a minimum in σ_{AC} centered around $V_V^{pore} = 0.08$ which shifts to lower V_V^{pore} with increasing temperature. At constant temperature the depth of the minimum decreases with increasing frequency and is entirely absent for $T \geq 900°C$ at 20 KHz. A similar trend is exhibited by $K'(\omega)$ vs V_v^{pore} plots except that the minimum there is still observed for the higher temperature measurements at 20KHz.

This behavior can be explained qualitatively by a model which assumes the total conductivity is the sum of contributions from the bulk Al_2O_3 grains and the grain boundary network. The contribution of volume conductivity is qualitatively depicted in Fig. 42. The conductivity of the loose stack is essentially zero. As contacts grow, and the amount of porosity diminishes, the cross sectional area available for conduction increases, and the volume conductivity increases monotonically (though not necessarily linearly). Ultimately, as V_v^{pore} approaches zero, this contribution to the conductivity approaches that of bulk alumina, designated σ_{bulk} in Figure 42(a).

In the early contact growth stage of sintering, the grain boundaries in the structure are largely at the interparticle contacts and are disconnected. Since only those isolated boundaries transverse to the current flow can have any influence on the conductivity, the contribution of σ_{gb} to σ_{total} is negligible unless $\sigma_{gb} \ll \sigma_{grain}$, which is unlikely in this system. With
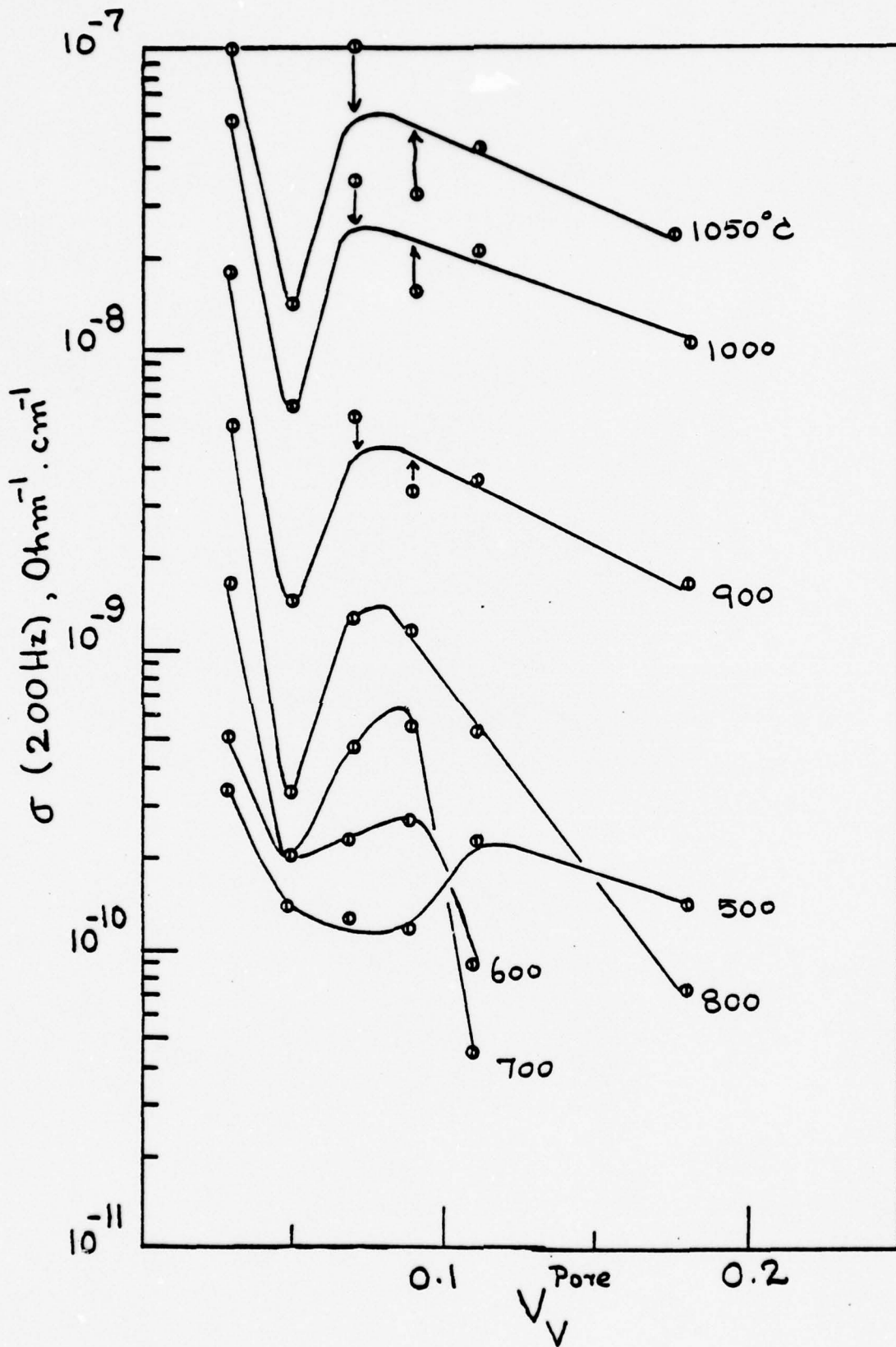
Figure 36. Plot of the electrical conductivity (200Hz) versus the volume fraction of pores in pure alumina samples hot-pressed at 1500°C-1000psi-t minutes.
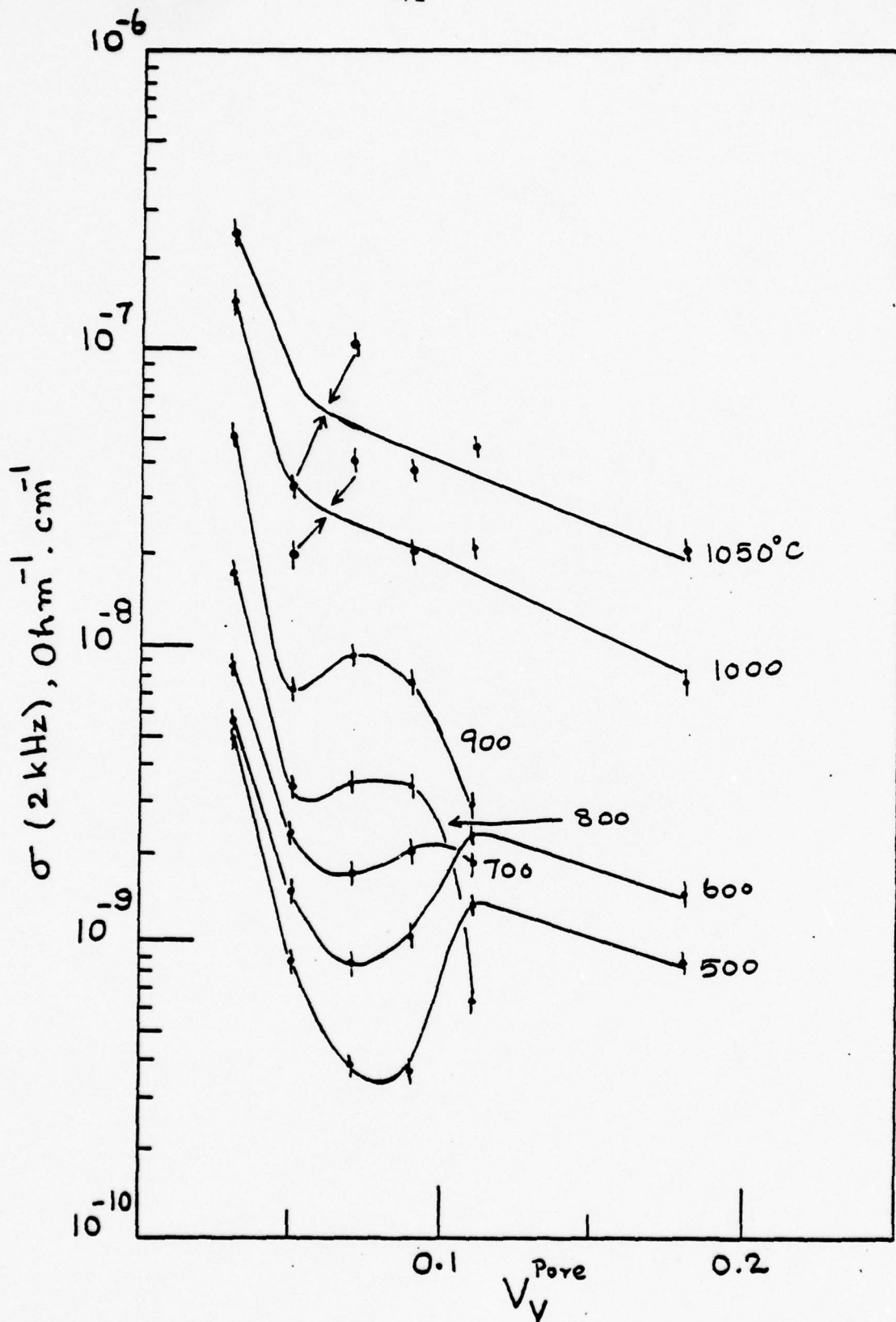
Figure 37. Plot of the electrical conductivity (2 KHz) versus the volume fraction of pores in pure alumina samples hot-pressed at 1500°C-1000psi-t minutes.
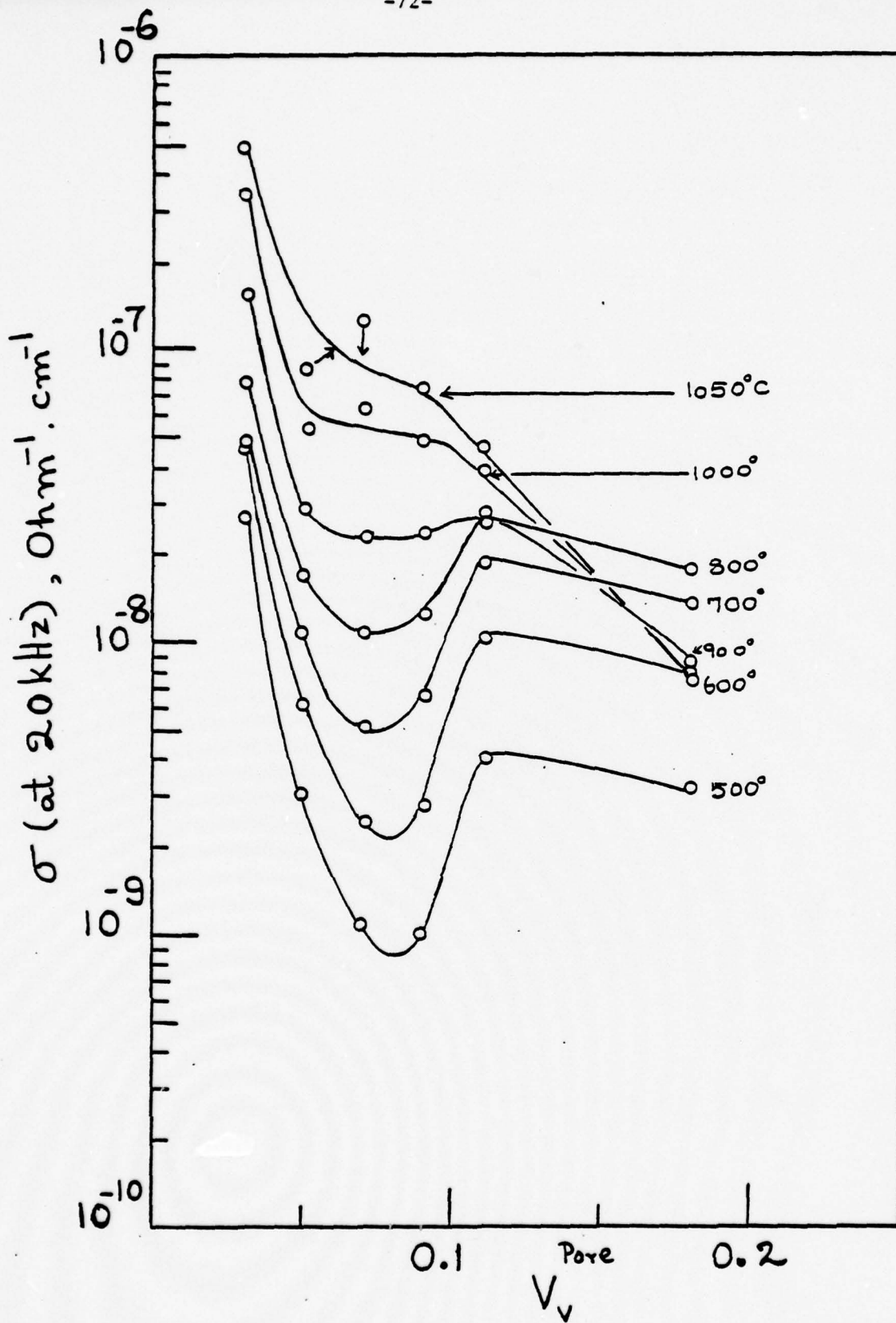
Figure 38. Plot of the electrical conductivity (20KHz) versus the volume fraction of pores in pure alumina samples hot-pressed at 1500°C-1000psi-t minutes.

Figure 39. Plot of the relative dielectric constant (200Hz), K', versus the volume fraction of pores in pure alumina samples hot-pressed at 1500°C-1000psi-t minutes.

Figure 40. Plot of the relative dielectric constant (20KHz), K', versus the volume fraction of pores in pure alumina samples hot pressed at 1500°C-1000psi-t minutes.
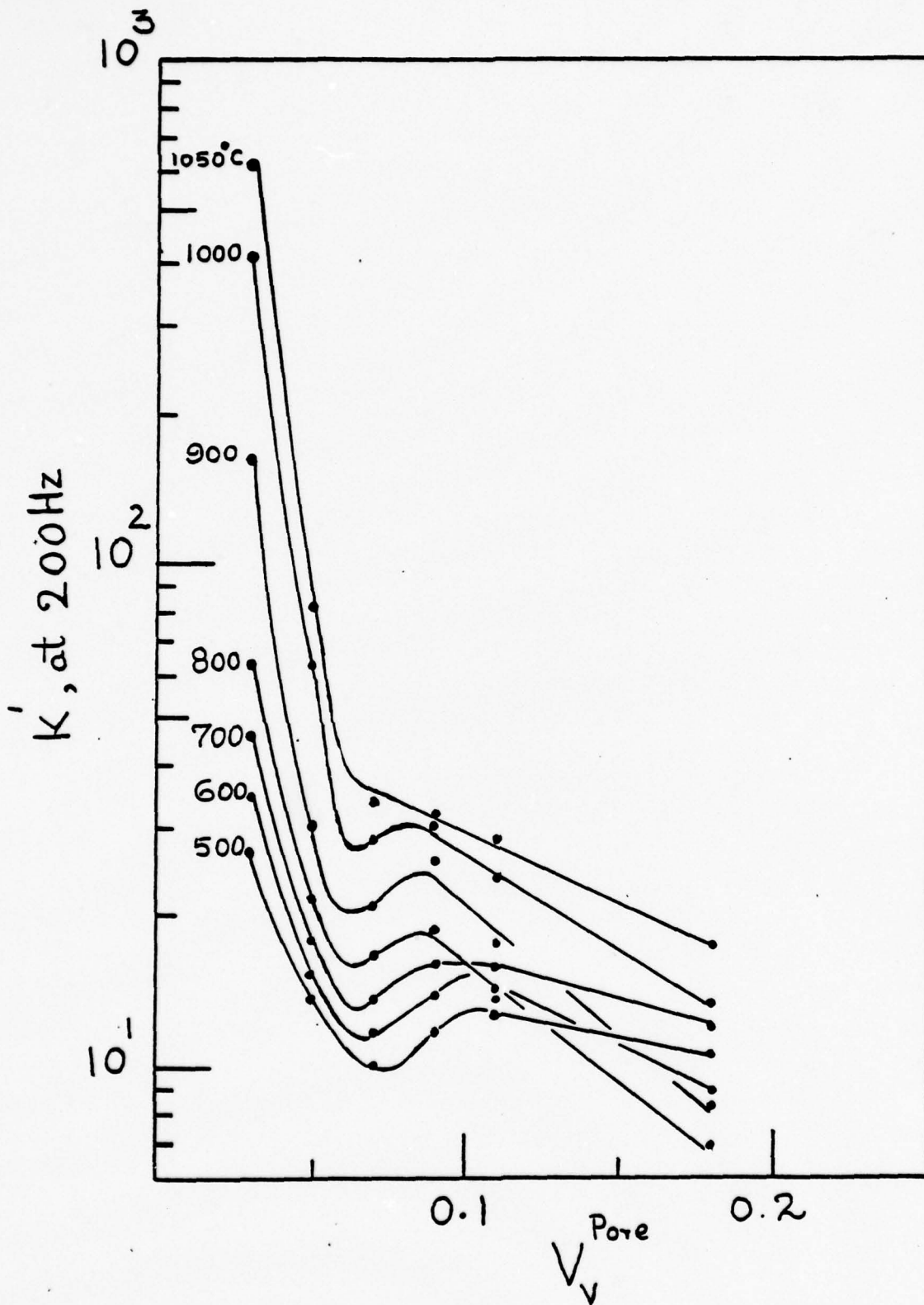
Figure 41. Plot of the relative dielectric constant (20KHz),K', versus the volume fraction of pores in pure alumina samples hot-pressed at 1500°C-1000 psi-t minutes.
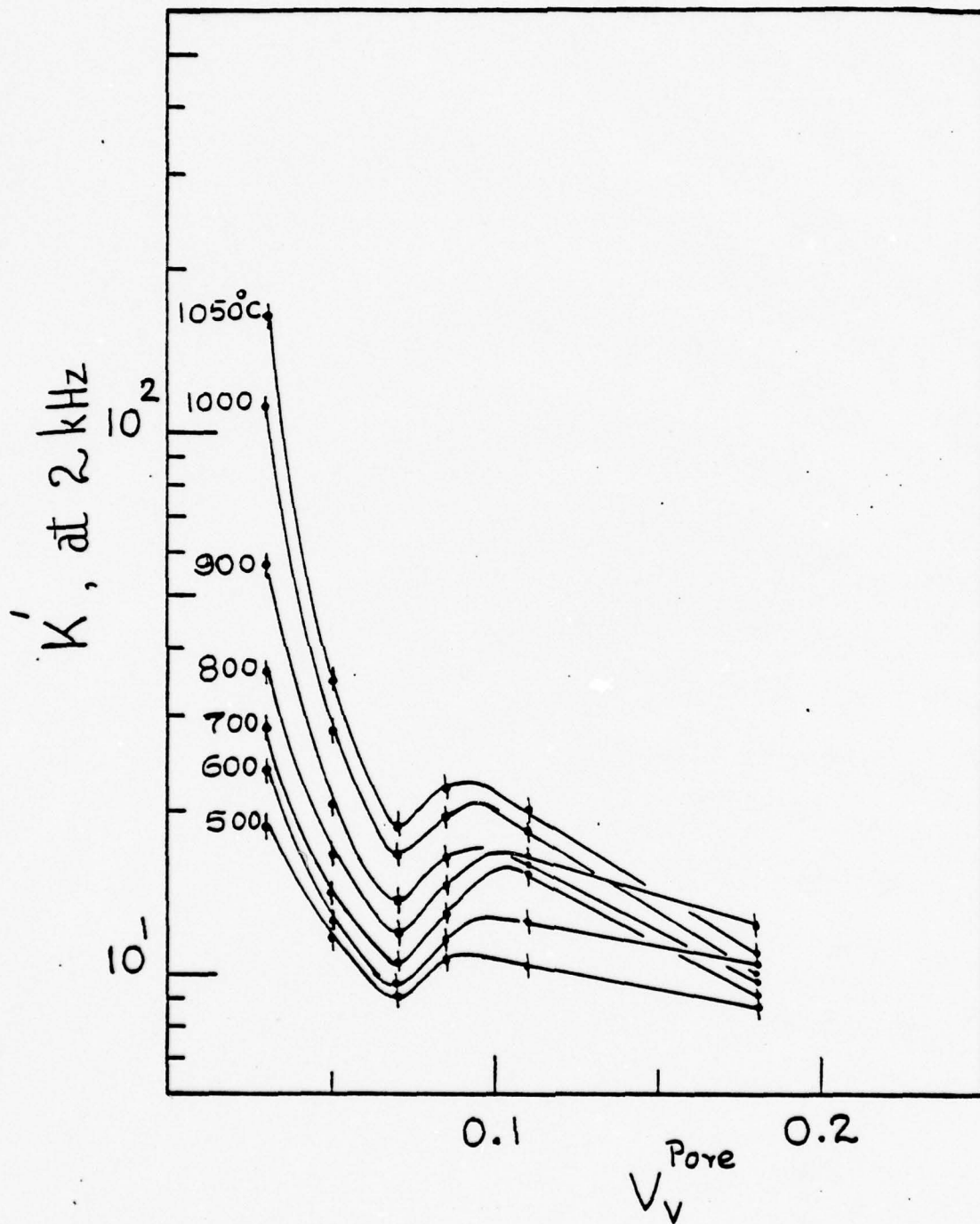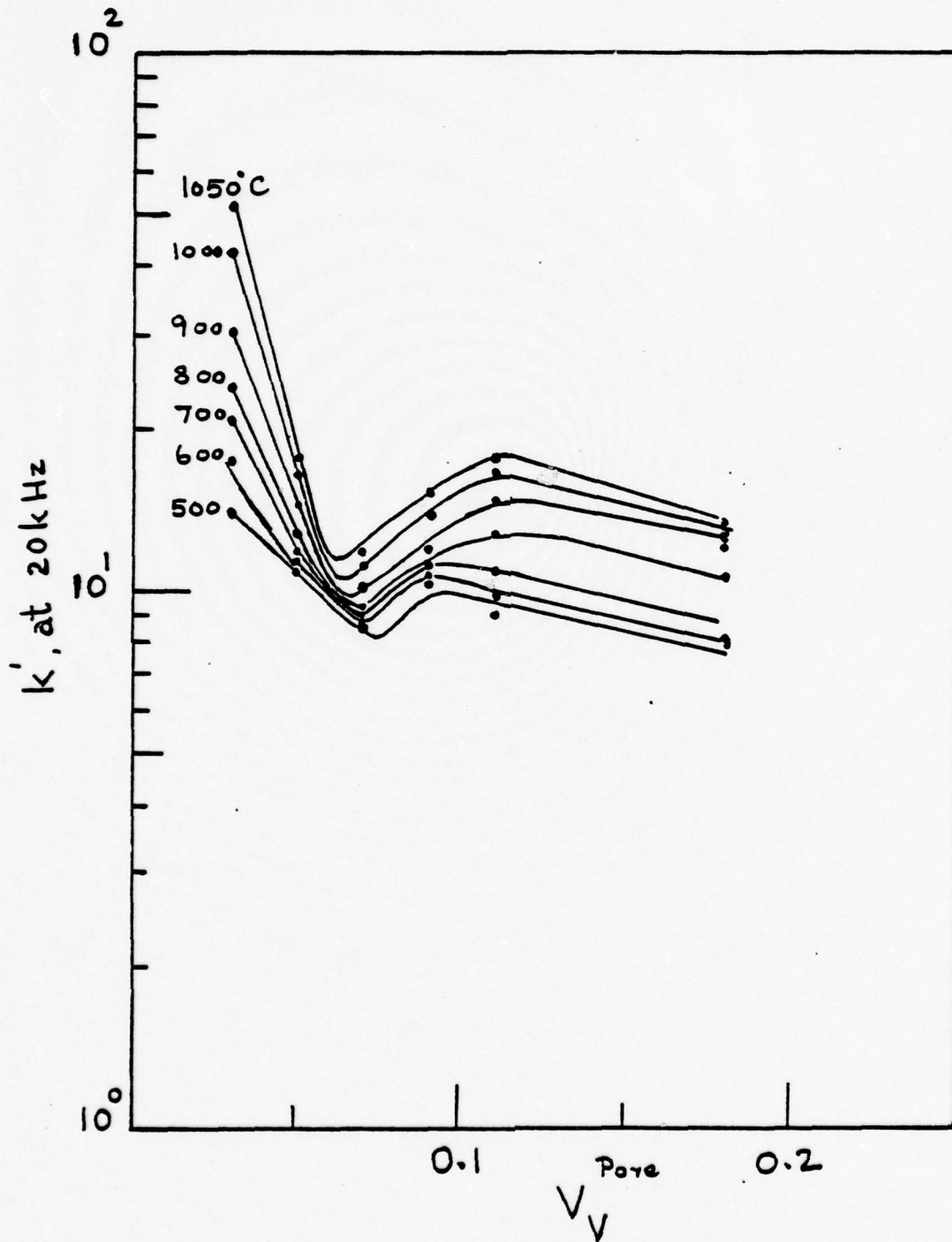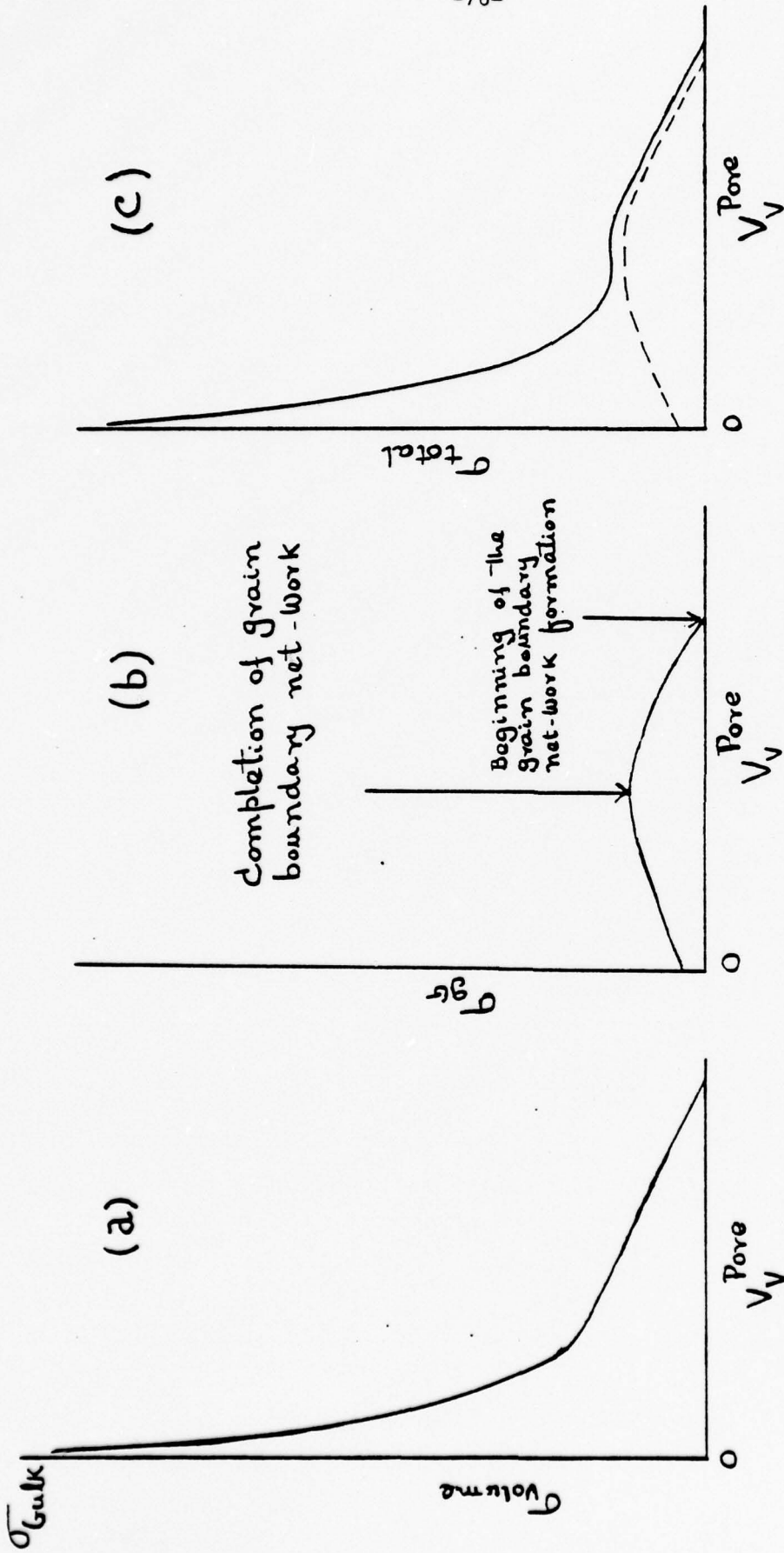
Figure 42. Qualitative representation of the contributions of different components to the total conductivity in pure alumina.

increasing sintering the closure of pores and channels dominates the micro-structural evolution and as interparticle contacts meet, a connected grain boundary network forms. The σ_{gb} contribution to the total conductivity increases accordingly. Once the network is nearly fully formed, grain growth may occur, decreasing the grain boundary area and, thus, σ_{gb}. Ultimately, at $V_v^{pore} = 0$, this contribution reaches a small but finite value, depending upon the final grain size attained. Thus, σ_{gb} would be expected to show the behavior exhibited in Fig. 42(b).

The total conductivity, shown in Fig. 42(c), is the sum of these two contributions. If the grain boundary conductivity is sufficiently large, the resultant plot of σ_{total} will show a pronounced minimum, as is observed experimentally at lower temperatures Figs. 36-38. The decrease in magnitude and eventual disappearance of the conductivity minimum can be accounted for if the temperature dependence of σ_{grain} is greater than that of σ_{gb} so that at the higher temperatures $\sigma_{grain} \gg \sigma_{gb}$. Likewise, the variation of the minimum with applied frequency can be explained if the frequency dependence of σ_{grain} is stronger than that of σ_{gb}.

Although the variation of σ_{gb} and σ_{grain} with microstructure cannot be measured independently to verify the model, indirect evidence of its validity is provided by Fig. 6, in which $Sv^{\alpha\alpha}$, the experimentally measured grain boundary surface area per unit volume, is plotted as a function of V_v^{pore}. If the thickness of the grain boundary regions does not change with V_v^{pore}, σ_{gb} should vary directly as $S_v^{\alpha\alpha}$; comparison of Figs. 6 and 42(b) reveals a close similarity in their dependence on V_v^{pore}.

Particle Size Effects in Polycrystalline Alumina: Samples with striking differences in both electrical and microstructural properties were produced by hot pressing either duPont K-θ or Linde A Al_2O_3 under identical conditions. The microstructural properties are summarized in Table VIII; the electrical properties are given in Figs. 43-46.

Table VIII

Comparison of Quantitative Microstructural Properties
of Samples Hot-Pressed from duPont and Linde A Al_2O_3

Sample	Hot-pressing Conditions	Relative Density	V_v	$S_v^{\alpha\rho}$, cm^{-1}	$S_v^{\alpha\alpha}$, cm^{-1}	$M_v^{\alpha\rho}$, cm^{-2}	$L_v^{\alpha\alpha\rho}$, cm^{-2}	$L_v^{\alpha\alpha\alpha}$, cm^{-2}
DuPont alumina	1450°C-6000 psi-30 m	95.3	.04	4.56×10^2	2.76×10^3	7.88×10^6	7.35×10^6	5.53×10^6
"	1450°C-6000 psi-0 m	93.6	.06	5.64×10^2	2.46×10^3	7.23×10^6	6.60×10^6	4.34×10^6
Linde A	1450°C-6000 psi-30 m	96.2	.03	9.71×10^2	6.25×10^3	1.85×10^7	1.40×10^7	3.70×10^7
—	1450°C-6000 psi-0 m	77.0	.08 (!)	2.12×10^3	1.41×10^4	1.12×10^7	4.98×10^7	1.68×10^8

Table VIII clearly shows the influence of the starting powder on microstructural properties. For example the duPont and Linde A 1450°C-6000psi-30 min samples have nearly the same V_v^{pore} (and hence relative densities), yet the surface area per unit volume of pore-grain interface in the Linde A is more than double that of the duPont specimen. Likewise, the other parameters for the Linde A sample in Table VIII are more than double than those for the duPont material.
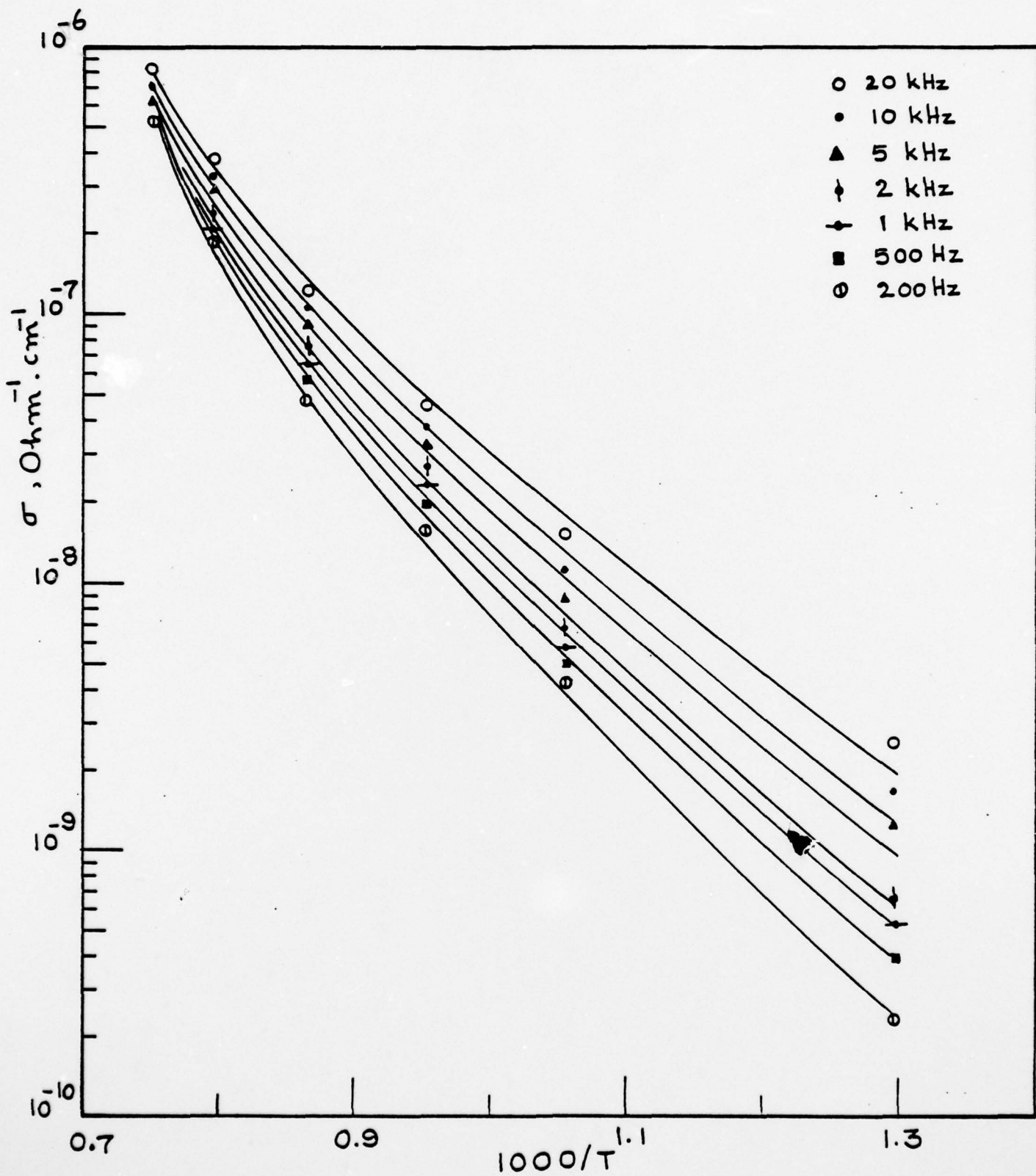
Figure 43.   Plot of the electrical conductivity versus reciprocal temperature of sample (#44A) hot pressed at 1450°C-6000psi-0 minutes.

Figure 44. Plot of the electrical conductivity versus reciprocal temperature of Sample (#37) hot pressed at 1450°C-6000psi-30 minutes.
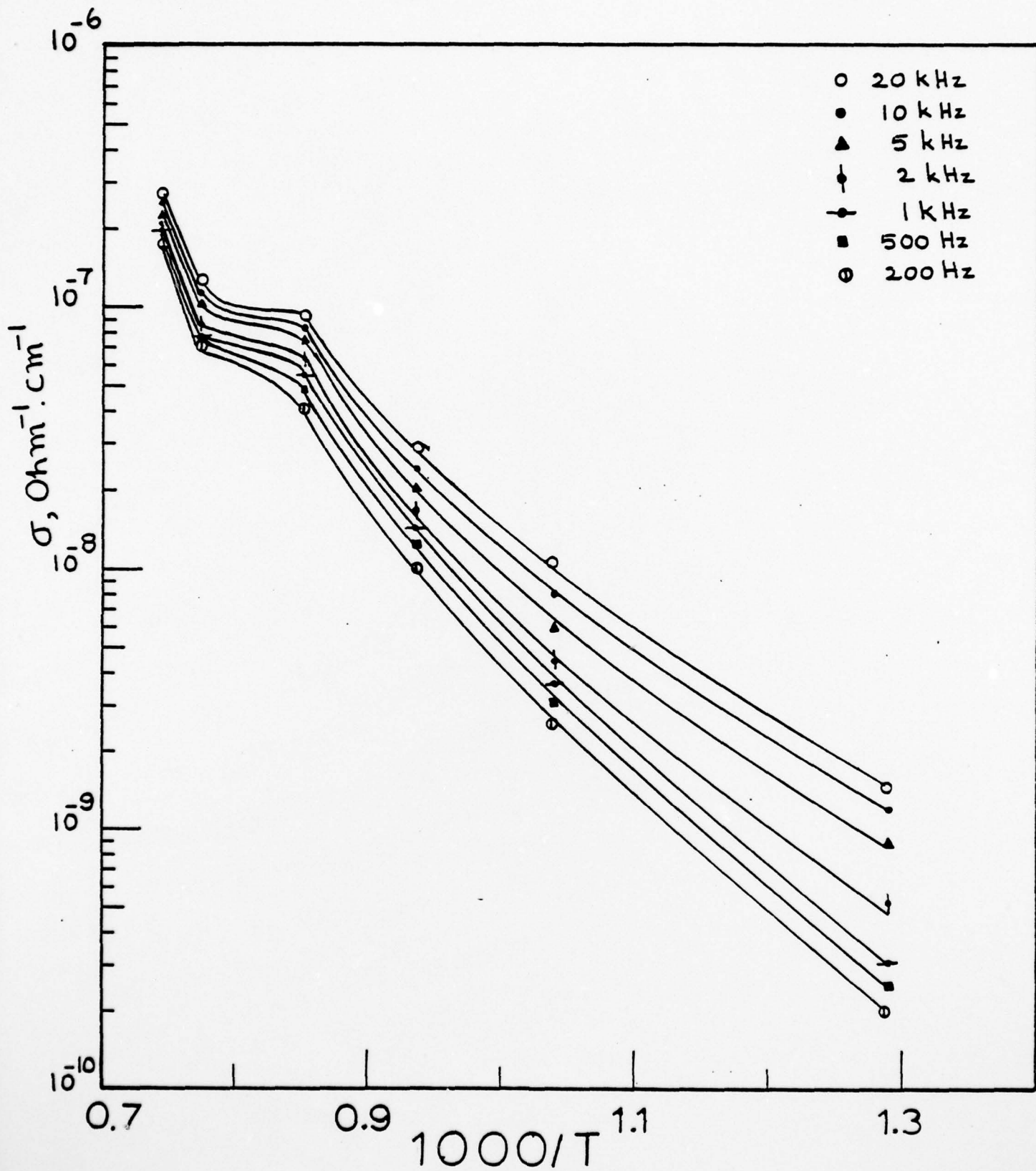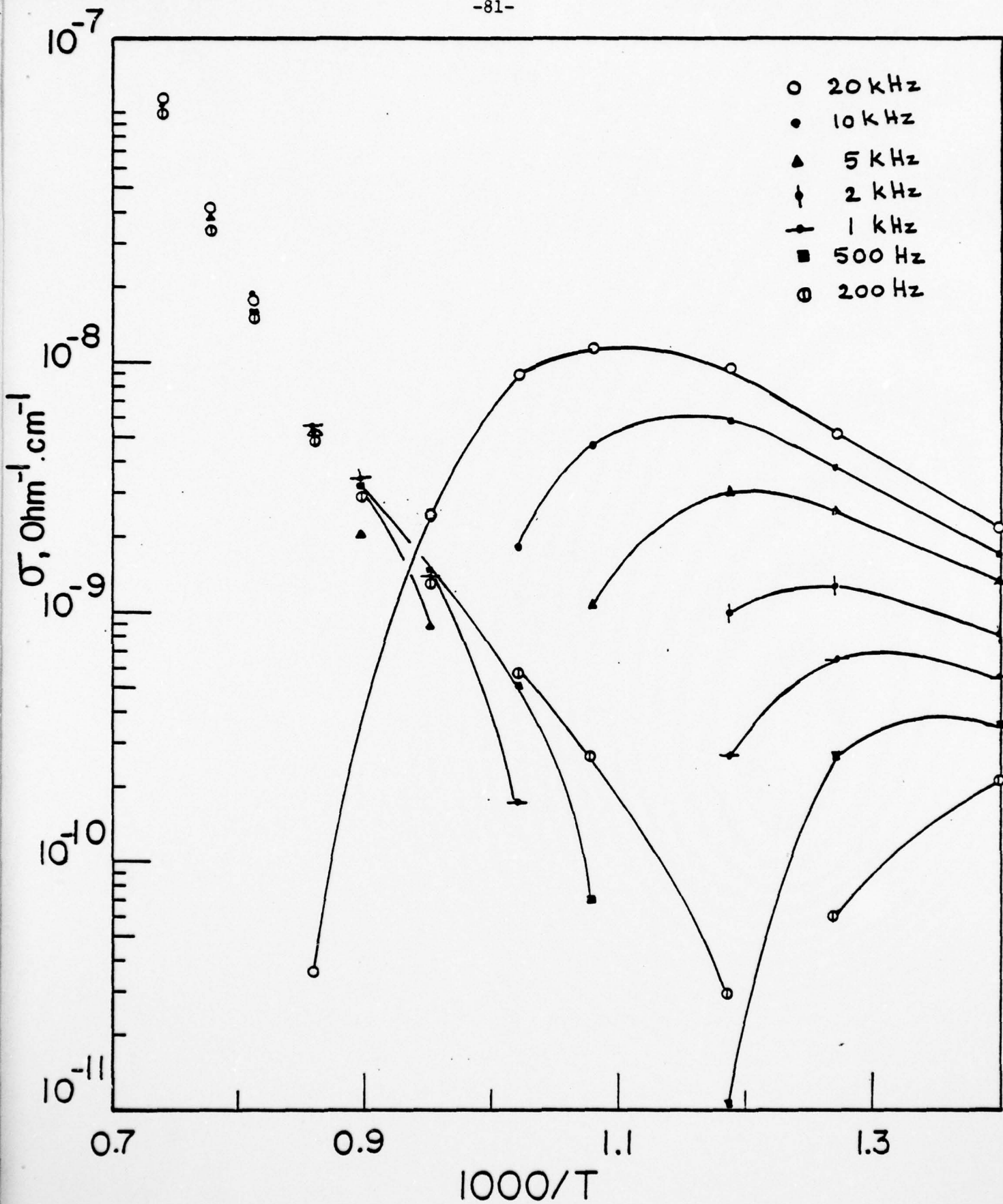
Figure 45. Plot of the electrical conductivity versus reciprocal temperature of sample (#47, Linde A) hot pressed at 1450°C-6000 psi -0 minutes.
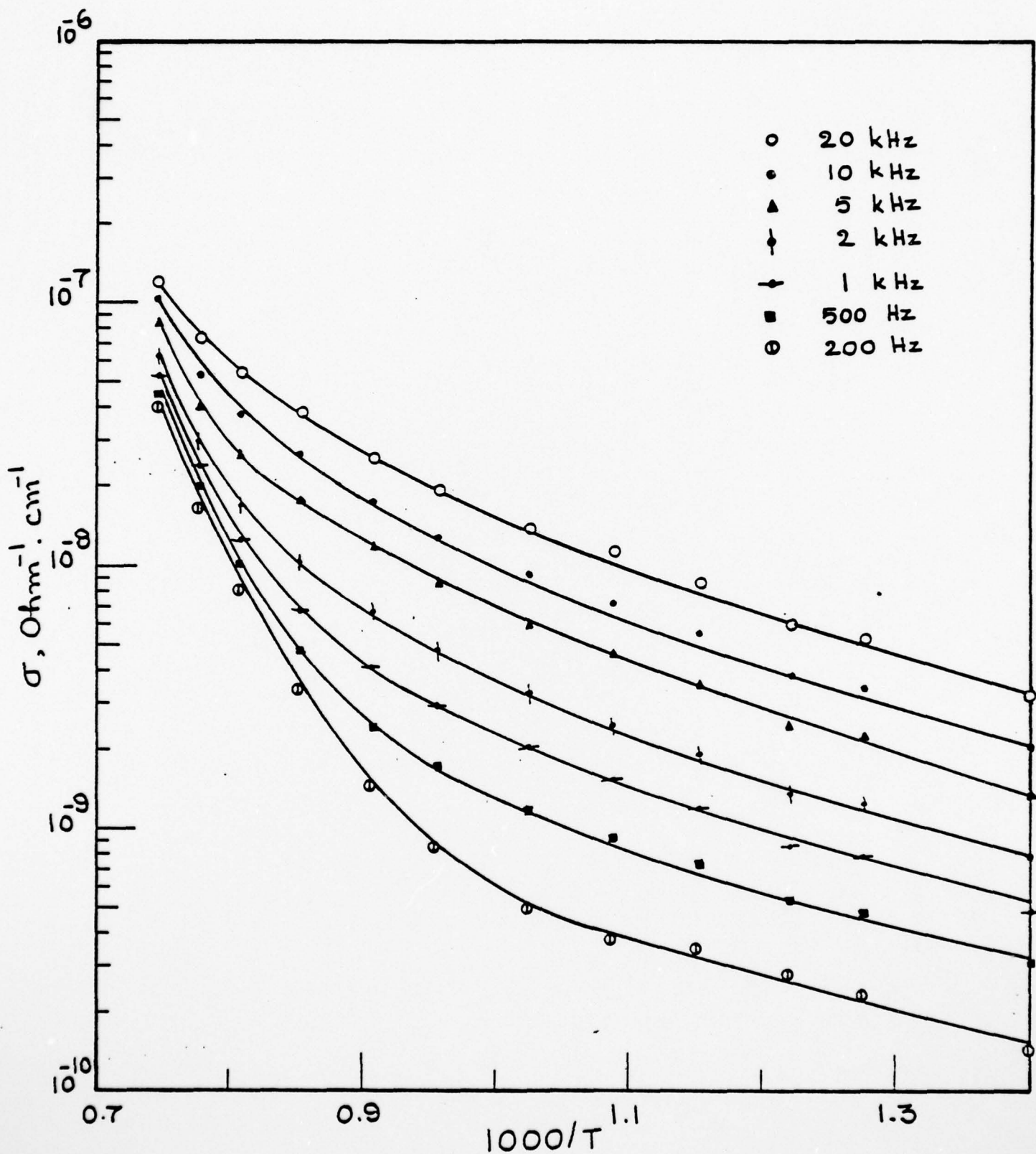
Figure 46. Plot of the electrical conductivity versus reciprocal temperature of sample (#40B, LindeA) hot pressed at 1450° -6000psi- 30 minutes.

Both the samples made from duPont alumina exhibited very similar electrical conductivities except that above 900°C, the conductivity of the sample hot-pressed for 30 min. was a factor of 5 lower than that for the sample hot-pressed for zero time (zero time means that once the desired temperature was attained, full pressure was applied, the furnace turned off and the pressure was set to decrease slowly as the sample cooled). By contrast, samples hot-pressed from Linde A for zero time exhibit a discontinuity in the σ-1/T plot, as is the case with the samples hot-pressed from duPont alumina for zero time in the 1500°C-1000psi - and 1400°C-2000psi series. The conductivity behavior of the 1450°C-6000psi-30 min. Linde A sample more closely resembles that of the samples hot-pressed from duPont alumina for 60 and 120 min in the 1500°C-1000psi-t series. The microstructural properties of these three samples are given in Table IX. As can be seen, the microstructures of these samples are much more nearly the same than is the case for the specimens of Table VIII.

Table IX

Comparison of Microstructural Properties
of Samples with Similar Electrical Behavior

Sample	Hot-pressing Conditions	Relative Density	Porosity	$S_v^{\alpha\rho}$, cm^{-1}	$S_v^{\alpha\alpha}$, cm^{-1}	$M_v^{\alpha\rho}$ cm^{-2}	$L_v^{\alpha\alpha\rho}$ cm^{-2}	$L_v^{\alpha\alpha\alpha}$ cm^{-2}
DuPont	1500°C-1000 psi-120m	94.5	.03	7.50×10^2	4.78×10^3	1.50×10^7	1.19×10^7	1.69×10^7
"	1500°C-1000 psi-60m	95.0	.05	1.32×10^3	4.66×10^3	2.18×10^7	1.81×10^7	1.42×10^7
Linde A	1450°C-6000 psi-30m	96.2	.03	9.71×10^2	6.25×10^3	1.85×10^7	1.40×10^7	3.70×10^7

<u>Significance of the Concept of Microstructural Path</u>: Comparison of the
properties of two specimens of nearly identical density which were prepared
so as to lie on different paths of microstructural change allows us to assess
the significance of this concept for electrical properties. Both were made
from the same batch of duPont Al_2O_3 under as nearly identical conditions as
possible except one was hot pressed for 1500°C-1000psi-60min and the other
for 1450°C-6000psi-30min. Even though the densities are the same, the micro-
structural properties of each are distinctly different, as can be seen from
Table X,

Table X

Properties of Samples on Different Paths of Microstructural Change

Sample	Hot-pressing Conditions	Relative Density	V_v^{pore}	$S_v^{\alpha\rho}$, cm^{-1}	$S_v^{\alpha\alpha}$, cm^{-1}	$M_v^{\alpha\rho}$, cm^{-1}	$L_v^{\alpha\alpha\rho}$, cm^{-1}	$L_v^{\alpha\alpha\alpha}$, cm^{-1}
DuPont alumina	1500°C-1000 psi-60m	95.01	.05	1.32×10^3	4.66×10^3	2.18×10^7	1.81×10^7	1.42×10^7
"	1450°C-6000 psi-30m	95.27	.04	4.56×10^2	2.76×10^3	7.88×10^6	7.35×10^6	5.53×10^6

Conventional reasoning, based on similarity of compositions and densities, would
predict very similar electrical properties. This is not the case, as seen in
Figs. 47-49. The sample exhibiting the largest discontinuity in the log σ vs.
1/T plot is the one with the highest values of $S_V^{\alpha\rho}$ and $S_V^{\alpha\alpha}$. This is entirely
consistent with the explanation given on pages 69-77 and schematically illustrated
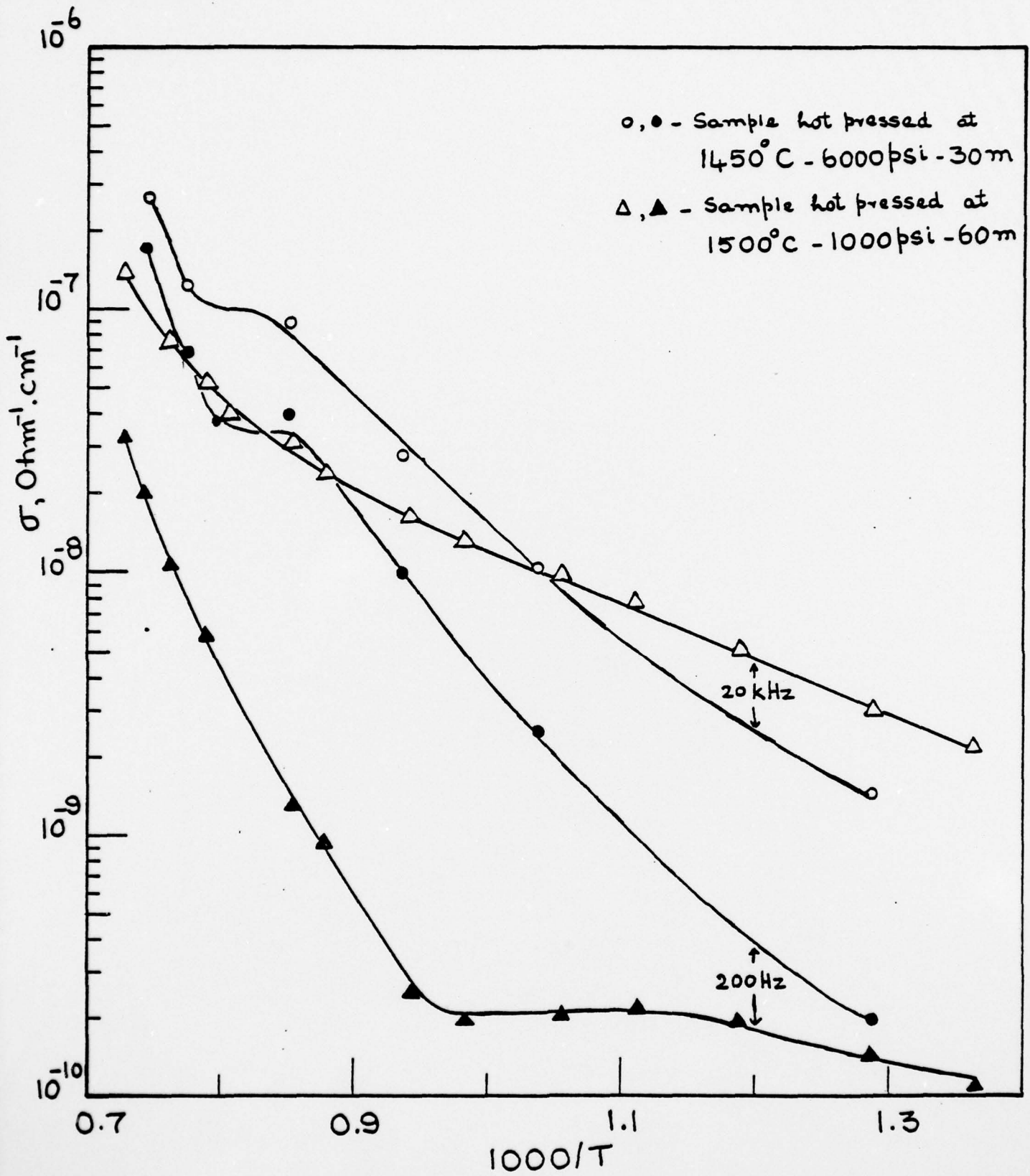in Fig. 42.

Figure 47. Plot of the electrical conductivity versus reciprocal temperature of samples with similar densities but are on different microstructural paths.
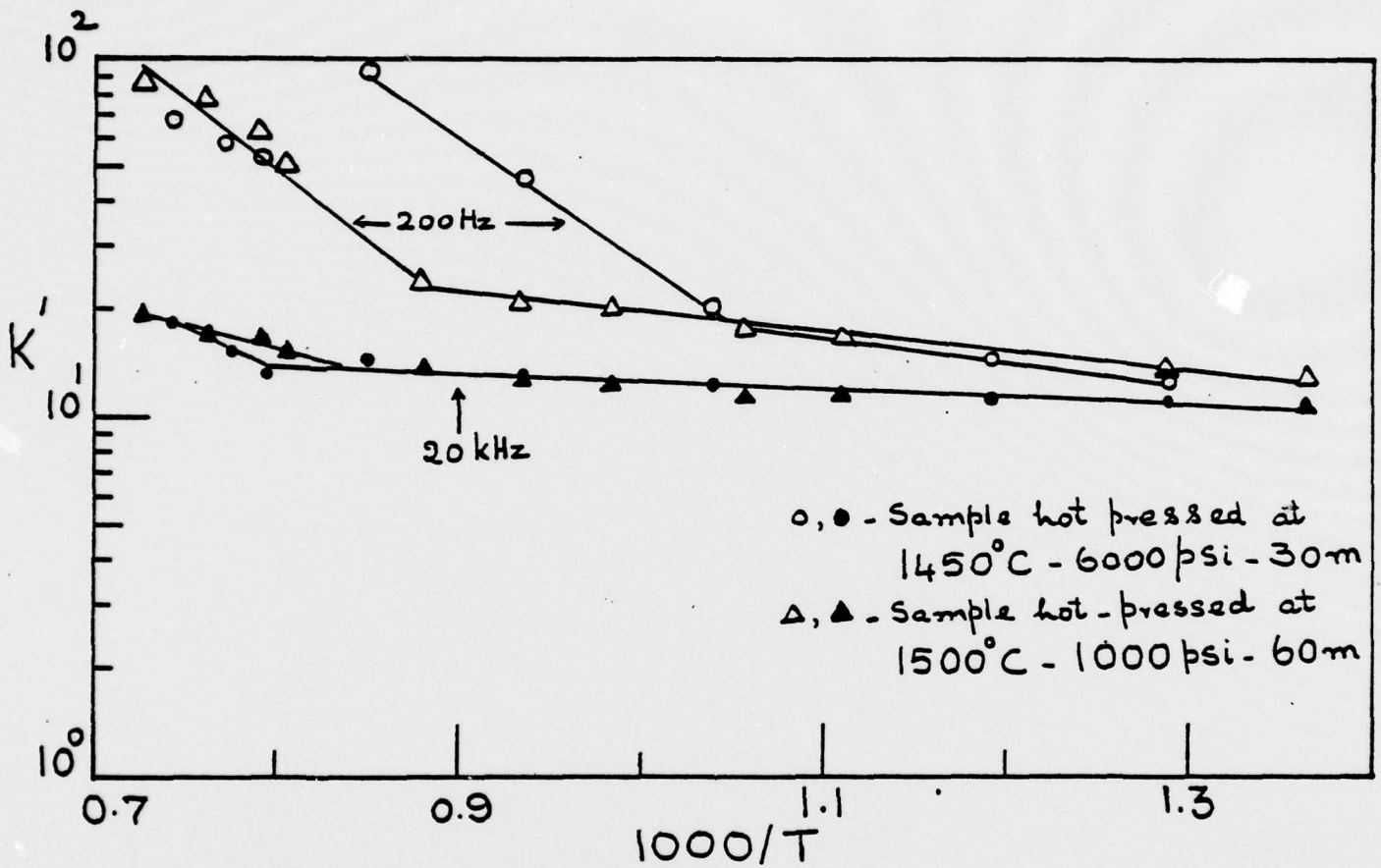
Figure 48. Plot of the relative dielectric constant (K') versus reciprocal temperature of samples with similar densities but are on different microstructural paths.
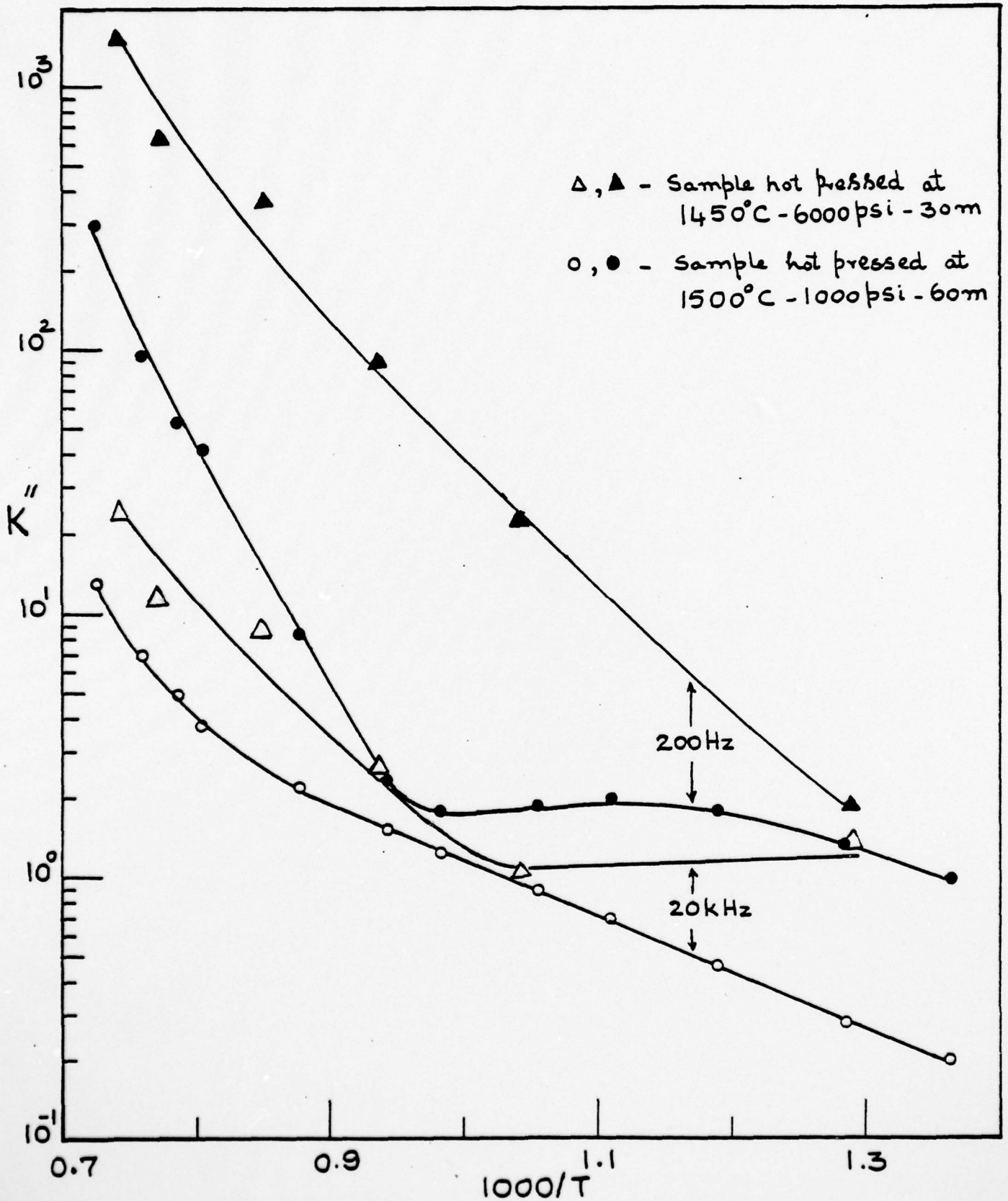
Figure 49. Plot of the loss factor (K") versus reciprocal temperature of samples with similar densities, but are on different microstructural paths.

Quantitative Microscopy of BaTiO$_3$ and PZT Ceramics*

Introduction

The microstructure of polycrystalline BaTiO$_3$ or PZT consists of conventional porosity and grain geometries and also a ferroelectric domain structure within the grains. Both levels of structure have been found to influence the mechanical and dielectric properties of this material. This structure and the resulting properties are sensitive to variables of composition, time and temperature of heat treatment, pressure, and the presence of electric fields. Changes in properties with aging time are also thought to be related to changes in this structure.

A schematic of the grain and domain structure of polycrystalline BaTiO$_3$ that has undergone incomplete grain growth is shown in Figure 50. There are several geometric features of this structure that may be analyzed quantitatively using the point and line-intercept counts. These include the relative volume fractions of porosity, V_V^{POR}, of fine grained volume, V_V^f, that has not yet experienced grain growth, and the volume fraction of large grained solid, V_V^s. (It is assumed that small grained porosity is below the resolution limit.) Within each large grain a portion of that volume, V_V^{180+}, is polarized 180° with respect to the other amd may be detected using differential etching relief. The volumes of 180° and 90° domains are interpenetrating so

$$V_V^s \leq V_V^{180+} + V_V^{90}, \quad V_V^{POR} + V_V^s + V_V^f = 1, \quad V_V^{90} = V_V^s + V_V^f = 1 - V_V^{POR}$$

An enclosing interface is associated with each of these volumes. Thus, the large grains are bounded by pore-solid, S_V^{P-S}, and grain-fine grain, S_V^{s-f}, areas. Within the grains are domain interfaces between antiparallel domains, S_V^{180+}, between 90° domains, S_V^{90}, the 90° domain bands, S_V^{band}, and the area of the [111] twin planes, S_V^{111}. The total area bounding the 90° domains
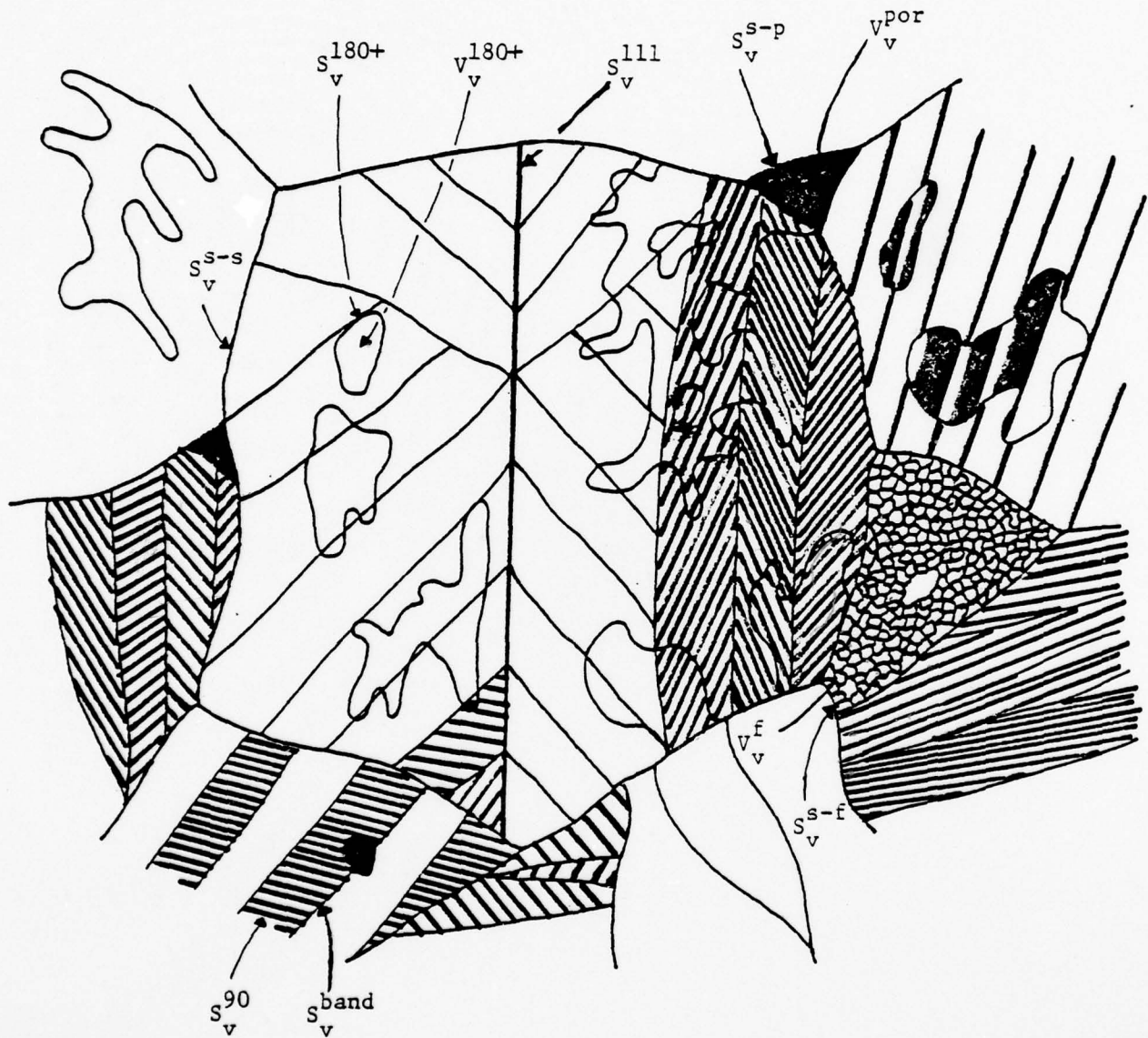
Figure 50. Schematic representation of the grain and domain structure of polycrystalline BaTiO$_3$ which had incomplete grain growth.

is actually

$$S_V^{90 \text{ tot}} = S_V^{90} + S_V^{\text{band}} + S_V^{111}$$

since these elements can be counted separately.

Measurements of grain and domain volume and area based on true micro-structural geometries rather than assumed particle or domain shapes, provide the means for improving understanding of several aspects of ferroelectric materials:

1) The relative amounts of 180° domain volume, S_V^{180+} and $S_V^{180-} = S_V^s = S_V^{180+}$, can be used as a quantitative measure of degree of poling. Correlations of this parameter with X-ray or electrical measurements can provide additional indices.

2) Measurement of domain wall areas may be used to improve the accuracy domain wall energy determinations.

3) Calculations of dielectric and piezoelectric properties of poly-crystalline material which utilize more realistic microstructural geometries have the potential for better agreement with experimentally measured values.[37,38]

4) The influence of domain geometry on aging phenomena may be clarified with a quantitative determination of domain structure.

5) The effect of processing on microstructure and properties may be studied quantitatively in terms of a path of microstructural change. For example, the degree of grain growth may be followed as a function of V_V^f or the influence of fabricating conditions on forming [111] twins as a function of S_V^{111}.

The goal of this portion of the project was to determine which, if any, of the above measurements could be made on a series of $BaTiO_3$ ceramics with differing microstructures. Once the feasibility was established the techniques

would be applied to commercial PZT sonar transducers in an attempt to determine the relation between microstructure and aging.

Experimental - $BaTiO_3$

The starting $BaTiO_3$ powder (Transelco grade 219-2) of 0.3-1.0 μm particle size (1.0-3.0 μm agglomerates) was hot pressed in graphite dies at 1250°C under a uniaxial pressure of 5000 psi. The sample was heated from room temperature to 1250°C as rapidly as possible (usually 15-17 minutes), the pressure applied for 15 minutes, and then the pressure was released and the power shut off. The sample cooled to 900°C in about 10 minutes. The pellet density was measured by Archimedian displacement in water. The pellets subsequently were heat treated in air to obtain several different grain size renges. Annealing was done at 1000°C for 24 hours to obtain fine grained material, 1250°C for 38 hours for a sample with intermediate grain size, and at 1350°C for 24 hours to obtain large grained specimens. The samples were then polished following generally the technique of Kontoleon and Tomlinson.[39] The final polishing step used 0.3 μm Al_2O_3 on nylon cloth with a few drops of the etching solution as a lubricant. The sample was then etched for 30-40 seconds and dried with an air blast. The acid etching solution was one volume percent of a $HF-HNO_3$ mixture (1 part HF, 2 parts HNO_3) in water.

Quantitative microscopy measurements were performed manually using an optical microscope (Research Metallograph II, Bausch and Lomb) at 800X magnification. A 49 point square grid in the reticule of the eyepiece was projected on the viewing field and its size calibrated with a stage micrometer to be 107 μm square. The best contrast was obtained by tilting the illumination slightly to shadow the relief obtained by polishing and etching and by using a light grey filter. The point counts were made using the 49

grid points, while the seven horizontal grid lines were used for the line intercept count. This gave a total line length of 749μm. By visually focusing on a particular geometric feature and scanning over the grid while making small adjustments to the microscope focus, the complex structure was divided into counts on the several simpler elements. The following counts were made on the small, intermediate, and large grained samples by examining 25 fields of view for each: P_P^{POR}, P_P^f, P_P^{180+}, P_L^{P-s}, P_L^{s-f}, P_L^{s-s}, P_L^{111}, P_P^{180+}, P_L^{band}, and P_L^{90}. After converting these to the corresponding volume or area parameters, the following mean intercepts were calculated:

$$\bar{\lambda}^{POR} = \frac{4V_V^{POR}}{S_V^{p-s}}; \quad \bar{\lambda}^{grain} = \frac{4(1-V_V^{POR}-V_V^f)}{S_V^{p-s}+2S_V^{s-s}} = \frac{4V_V^s}{S_V^{p-s}+2S_V^{s-s}}$$

$$\bar{\lambda}^{fine} = \frac{4V_V^f}{S_V^{s-f}}; \quad \bar{\lambda}^{180} = \frac{4V_V^{180+}}{S_V^{180+}}$$

$$\bar{\lambda}^{band} = \frac{4(1-V_V^{POR}-V_V^f)}{2S_V^{band}} = \frac{4V_V^s}{2S_V^{band}}; \quad \bar{\lambda}^{90} = \frac{4(1-V_V^{POR})}{2(S_V^{90}+S_V^{band}+S_V^{111})} = \frac{4(V_V^s+V_V^f)}{2S_V^{90\ tot}}$$

The 95% confidence interval was calculated as two times the standard error of the mean for the distribution of counts measured.

Results and Discussion - BaTiO₃

Figures 51-53 show the microstructures observed for fine, intermediate, and large grained BaTiO₃ samples. The densities of hot-pressed specimens were 96-98% of theoretical. Table XI presents the results of the quantitative microscopy measurements. The acid-etched fine grained sample (∿2 μm) has a pebbly surface and reliable intercept counts could not be made within the
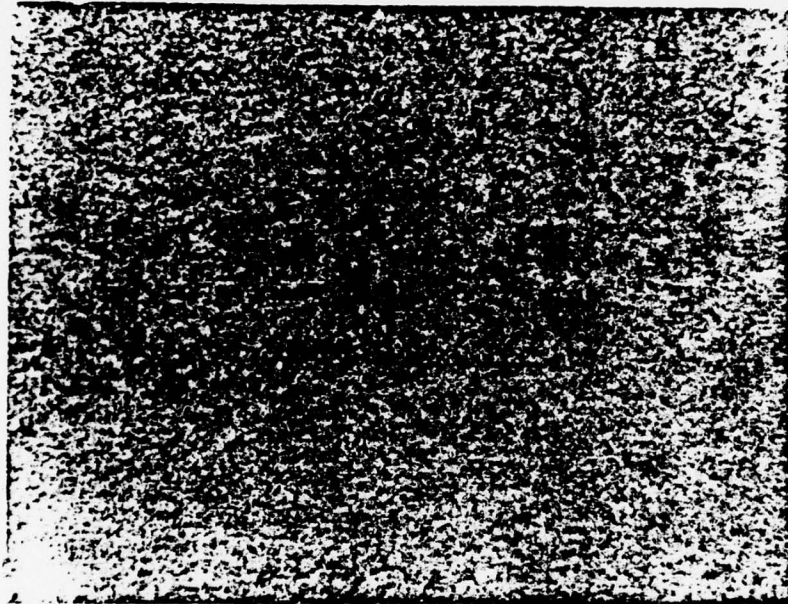
800X

Figure 51. Microstructure of fine grained polycrystalline BaTiO$_3$.
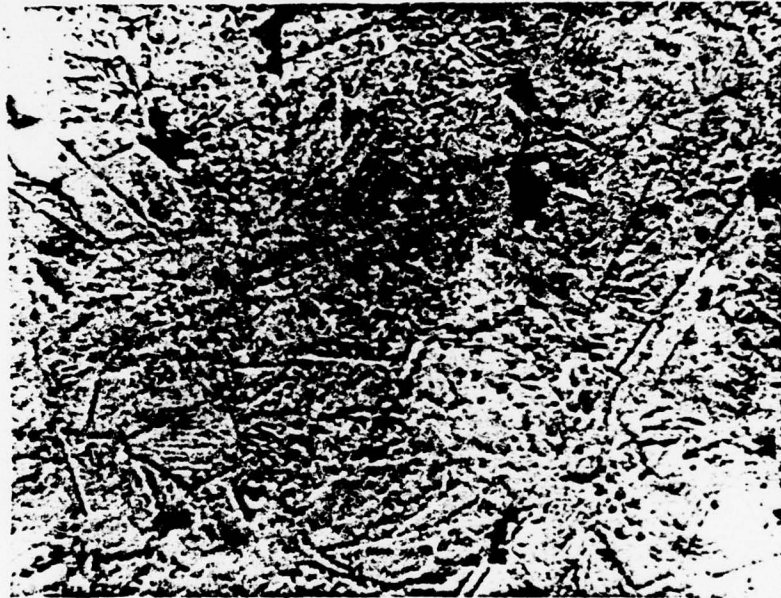
800X

Figure 52. Microstructure of intermediate grained polycrystalline BaTiO$_3$.

800X

Figure 53. Microstructure of large grained polycrystalline BaTiO$_3$.

Table XI

Results of Quantitative Microscopy

Parameter		Sample Grain Size		
		Fine	Intermediate	Large
V_v^{por}	cm³/cm³	0.048±0.021	0.038±0.017	0.054±0.015
V_v^{fine}	"	–	0.067±0.029	–
V_v^{180+}	"	–	0.434±0.036	0.598±0.036
S_v^{p-s}	cm²/cm³	38.4±8.7	82.1±15.1	56.1±14.0
S_v^{f-s}	"	–	72.1±18.7	–
S_v^{s-s}	"	14627	250.3±17.5	133.2±13.6
S_v^{111}	"	–	4.2±4.4	12.3±4.7
S_v^{180+}	"	–	482.3±102.4	600.3±93.9
S_v^{band}	"	–	710.3±69.8	780.2±62.1
S_v^{90}	"	–	2751±511.3	4528.0±607.5
$S_v^{90\ tot}$	"	–	3466.5	5320.5
$\bar{\lambda}^{por}$	μm	50.0	18.5	39.0
$\bar{\lambda}^{grain}$	"	1.3	61.4	117.0
$\bar{\lambda}^{fine}$	"	–	37.2	–
$\bar{\lambda}^{180}$	"	–	36.0	40.0
$\bar{\lambda}^{band}$	"	–	25.2	24.2
$\bar{\lambda}^{90}$	"	–	5.55	3.55

optical resolution of the microscope. Although measurements could have been
performed on thermally etched small-grained samples using scanning electron
microscopy, this was not done. The S_V^{s-s} for this material listed in Table XI
results from assuming $\overline{\lambda}^{grain}$ = 1.3μm. The structures for the intermediate
and large grain samples are similar to those reported by DeVries and Burke.[40]
Although the grain size of the intermediate sample is roughly half that of the
large grained sample, as seen by the greater S_V^{s-s} and $\overline{\lambda}^{grain}$ values in TableXI,
the 90° domain band area, S_V^{band}, twin area, S_V^{111}, and $\overline{\lambda}^{180}$ all show these
domain characteristics to be almost the same for both specimens and thus
independent of grain size. The $\overline{\lambda}^{180}$ result, in particular, illustrates the
value of quantitative microstructural analysis. By itself, visual inspection
of polished sections would not clearly show the decrease in V_V^{180+} and the
corresponding reduction of S_V^{180+} with grain size for the large and intermediate
grain size samples, or that the reduction is in proportion to give a relatively
constant $\overline{\lambda}^{180}$ which physically is a measure of antiparallel domain scale

(recall $\overline{\lambda}^{180} = \dfrac{4V_V^{180+}}{S_V^{180+}}$). The magnitude of $\overline{\lambda}^{band}$ and $\overline{\lambda}^{90}$ reflect the average

overall orientations of the surface-to-surface distances for the enclosed
volume and is not simply the distance between parallel surfaces. The constant
$\overline{\lambda}^{band}$ suggests that the increase in $\overline{\lambda}^{90}$ for the intermediate grain size sample
is a measure of slightly increased domain thickness over that for the large
grained sample. Since determination of P_L^{90} for large and intermediate grain
size samples was near the resolution limit of the optical microscope the
difference in $\overline{\lambda}^{90}$ for these two cases may not be that significant. Improved

accuracy in measuring features of this scale is readily available with electron

optics, however, and no problems for quantitative microscopy analysis at

increased magnification should be encountered as long as enough fields of

view are examined to obtain a representative sampling of the three-dimensional

structure.

Application of the Above Techniques to PZT Sonar Ceramics

By contrast with our experience with BaTiO$_3$, we were unable to develop

a metallographic technique to reliably reveal the domain structure in the

small-grained PZT ceramics supplied to us by R. Pohanka of the Naval Research

Lab. The etching procedure of Kontoleon and Tomlinson[39] proved unsuccessful,

as did several others we tried based on information in the literature. B. Jaffee[41]

suggested a method involving etching in a solution of 10 drops conc. HF

in 500 ml of a 1:1 conc. HCl - distilled water mixture. All but a small

strip of the sample surface to be etched was covered with tape and the sample

was immersed in the etching solution for 4 sec. After rinsing and drying

the sample, another small strip of tape, adjacent to the first, was cut

away and the sample was etched for another 4 sec. This procedure was

repeated until a sample consisting of parallel bands with successively

longer etches was produced. SEM examination revealed that this procedure

worked very well for revealing grain structure, but that in no case was the

domain pattern developed uniformly over the whole etched band. This non-

uniformity in the domain pattern prevented our obtaining reliable counting

statistics which are necessary for the calculations. The difference in

behavior between the BaTiO$_3$ and PZT seems related to the extremely fine

grain size in PZT relative to the BaTiO$_3$. Examples of the best metallography

we were able to achieve are shown in Fig. 54.

Due to manpower limitations we did not feel justified in launching a major effort to develop special metallographic techniques for fine grained PZT ceramics. Results on $BaTiO_3$ proved the feasibility of doing quantitative microscopy on ferroelectric domain patterns. Further work on commercial PZT ceramics will require a separate effort devoted entirely to the unique problems they raise.
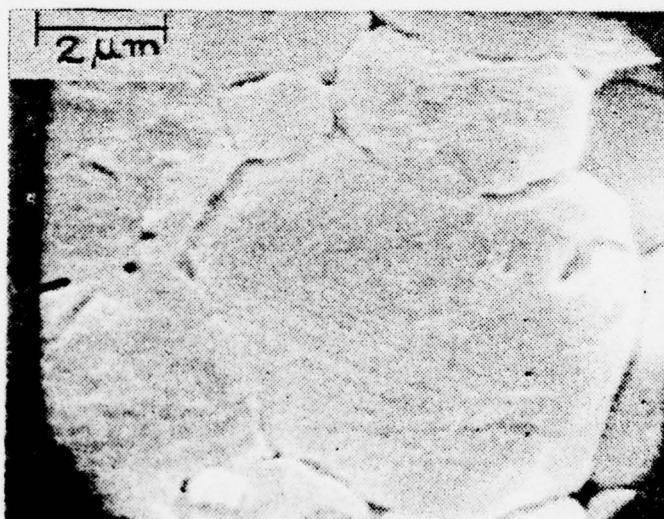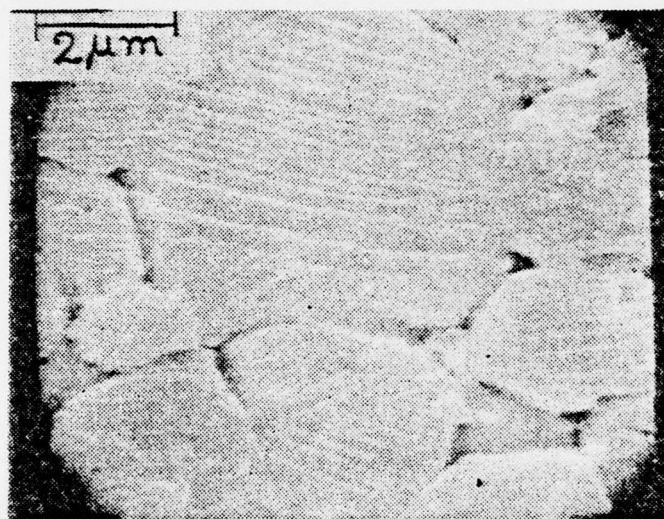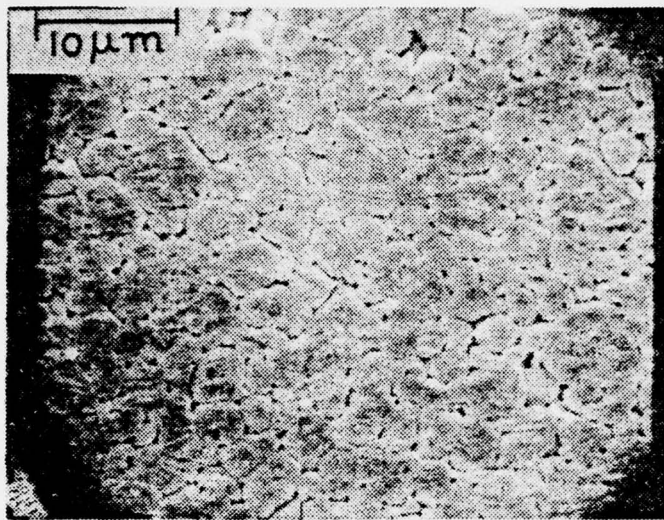
Figure 54. Scanning electron micrographs of PZT sonar ceramics etched
to reveal domain patterns.

References

1. J. C. Maxwell, Electricity and Magnetism, Vol. 1, 3rd Ed., Clarendon Press, Oxford, 1892, p. 440.

2. K. W. Wagner, Arch. Elecktrotechnik $\underline{2}$, 371 (1914).

3. R. W. Sillers, J. Inst. Elect. Engineers (London) $\underline{80}$, 378 (1937).

4. H. Fricke, Phys. Rev. $\underline{24}$, 575 (1924).

5. H. Fricke, J. Phys. Chem. $\underline{57}$, 934 (1953).

6. L. K. H. van Beek in Progress in Dielectrics, J. A. Burks, Ed., Vol. 7, CRC Press, Cleveland, 1966, pp. 69-114.

7. J. M. Wimmer, H. C. Graham, N. M. Tallan in Electrical Conductivity in Ceramics and Glass, Part A, N. M. Tallan, Ed., Marcel Dekker, N. Y., 1974, pp. 619-652.

8. D. A. G. Bruggeman, Ann. Phys. (Leipzig) $\underline{24}$, 636 (1935).

9. R. Landauer, J. Appl. Phys. $\underline{23}$, 779 (1952).

10. D. Stroud, Phys, Rev. B, $\underline{12}$, 3368 (1975).

11. S. R. Broadbent and J. M. Hammersley, Proc. Camb. Phil. Soc., $\underline{53}$, 629 (1957).

12. Scott Kirkpatrick, Rev. Mod. Phys. $\underline{45}$, 574 (1973).

13. Scott Kirkpatrick, Phys. Rev. Lett. $\underline{27}$, 1722 (1971).

14. G. E. Pike and C. H. Seager, Phys. Rev. B, $\underline{10}$, 1421 (1974).

15. C. H. Seager and G. E. Pike, Phys. Rev. B, $\underline{10}$, 1435 (1974).

16. G. E. Pike, W. J. Camp, C. H. Seager and G. L. McVay, Phys. Rev. B, $\underline{10}$, 4909 (1974).

17. R. Loehman, R. DeHoff and G. Rama Rao, "Electrical Properties of Poly-crystalline Ceramic Insulators", Technical Report April 1976, Contract # N00014-75-C-0888.

18. C. G. Koops, Phys. Rev. $\underline{83}$, 121 (1951).

19. T. Y. Tien, J. Amer. Ceram. Soc., $\underline{47}$, 430 (1964).

20. R. B. Greklia and T. Y. Tien, J. Amer. Ceram. Soc., $\underline{48}$, 22 (1965).

21. E. E. Underwood, Quantitative Stereology, Addison-Wesley, Reading, Mass. (1970).

22. R. T. DeHoff in _Treatise on Materials Science and Technology_, Vol. 1, Academic Press, N. Y., (1972) p. 247.

23. R. T. DeHoff and F. N. Rhines, _Quantitative Microscopy_, McGraw-Hill, N. Y. (1968).

24. R. T. DeHoff, E. H. Aigeltinger and K. R. Craig, J. Microscopy, 95, 69 (1972).

25. G. Moore, "Is Quantitative Metallography Quantitative?", ASTM STP-480 (1970).

26. R. N. Rhines, R. T. DeHoff and E. D. Whitney, "Quantitative Determination of Structure Property Relationships in Nuclear Fuel Element Materials", Final Report for the U. S. Atomic Energy Commission, Contract No. AT-(40-1)-4212, May 1975.

27. R. J. Brook, J. Yee and F. A. Kroger, "Electrochemical Cells and Electrical Conduction of Pure and Doped Al_2O_3", J. Amer. Ceram. Soc., 54, 444 (1971).

28. J. Yee and F. A. Kroger, "Measurements of Electromotive Force in Al_2O_3-Pitfalls and Results", J. Amer. Ceram. Soc., 56, 189 (1973).

29. R. C. McVickers, S. D. Ford and R. A. Dugdale, "Polishing and Etching Techniques for Dense Alumina", J. Amer. Ceram. Soc. 45, 199 (1962).

30. C. A. Elyard, "Discussion of Robinson and Gardner Note on Preparation of Highly Dense Al_2O_3 for Microscopic Examination", J. Amer. Ceram. Soc., 45, 47 (1962).

31. S. M. Gehl, "Structural Evolution and Electrical Conductivity of Sintered Uranium Dioxide", Doctoral Dissertation, University of Florida, 1977.

32. N. K. Hirgi, "Evolution of Microstructure During the Sintering of Boron Carbide", Masters Thesis, University of Florida, 1973.

33. E. H. Aigeltinger and H. E. Exner; Met. Trans., 8A, 421 (1977).

34. J. V. Florio, "Dilectric Properties of Alumina at High Temperatures: J. Amer. Ceram. Soc., 43, 262 (1960).

35. L. M. Atlas, H. Nagao and H. H. Nakamura, "Control of Dielectric Constant and Loss in Alumina Ceramics:, J. Amer. Ceram. Soc. 45, 467 (1962).

36. D. W. Peters, L. F. Feinstein and C. Peltzer, "High Temperature Electrical Conductivity of Alumina", J. Chem. Phys., 42, 2345 (1964).

37. M. Marutake, "A Calculation of Physical Constants of Ceramic Barium Titanate", J. Phys. Soc. Japan, 11, 807 (1956).

38. W. R. Buessem, L. E. Cross, and A. K. Goswami, "Phenomenological Theory of High Permittivity in Fine-Grained Barrium Titanate", J. Am. Ceram. Soc., 49, 33 (1966).

39. D. Kontoleon and J. Tomlinson, "Micro-examination of BaTiO$_3$, "Metals Progress, 69, 98 (1955).

40. R. C. DeVries and J. E. Burke, "Microstructure of Barium Titanate Ceramics," J. Am. Ceram. Soc., 40, 200 (1957).

41. B. Jaffee, personal communication to R. E. Loehman.

Technical and Summary Reports

Organization	No. of Copies	Organization	No. of Copies
Defense Documentation Center Cameron Station Alexandria, Virginia 22314	(12)	Naval Construction Batallion Civil Engineering Laboratory Port Hueneme, California 93043 Attn: Materials Division	(1)
Office of Naval Research Department of the Navy		Naval Electronics Laboratory Center San Diego, California 92152	
Attn: Code 471	(1)	Attn: Electron Materials	
Code 102	(1)	Sciences Division	(1)
Code 470	(1)		
		Naval Missile Center Materials Consultant Code 3312-1	
Commanding Officer Office of Naval Research Branch Office 495 Summer Street Boston, Massachusetts 02210	(1)	Point Mugu, California 93041	(1)
		Commanding Officer Naval Surface Weapons Center White Oak Laboratory Silver Spring, Maryland 20910	
Commanding Officer Office of Naval Research Branch Office 536 South Clark Street Chicago, Illinois 60605	(1)	Attn: Library	(1)
		David W. Taylor Naval Ship R&D Center Materials Department Annapolis, Maryland 21402	(1)
Office of Naval Research San Francisco Area Office 760 Market Street, Room 447 San Francisco, California 94102 Attn: Dr. P. A. Miller	(1)	Naval Undersea Center San Diego, California 92132 Attn: Library	(1)
Naval Research Laboratory Washington, D.C. 20390		Naval Underwater System Center Newport, Rhode Island 02840 Attn: Library	(1)
Attn: Code 6000	(1)		
Code 6100	(1)	Naval Weapons Center China Lake, California 93555	
Code 6300	(1)	Attn: Library	(1)
Code 6400	(1)		
Code 2627	(1)	Naval Postgraduate School Monterey, California 93940	
Naval Air Development Center Code 302 Warminster, Pennsylvania 18974		Attn: Mechanical Engineering Dept.	(1)
Attn: Mr. F. S. Williams	(1)	Naval Air Systems Command Washington, D.C. 20360	
Naval Air Propulsion Test Center Trenton, New Jersey 08628		Attn: Code 52031	(1)
Attn: Library	(1)	Code 52032	(1)
		Code 320	(1)

Organization	No. of Copies	Organization	No. of Copies
Naval Sea System Command Washington, D.C. 20362 Attn: Code 035	(1)	NASA Headquarters Washington, D.C. 20546 Attn: Code RRM	(1)
Naval Facilities Engineering Command Alexandria, Virginia 22331 Attn: Code 03	(1)	NASA Lewis Research Center 21000 Brookpark Road Cleveland, Ohio 44135 Attn: Library	(1)
Scientific Advisor Commandant of the Marine Corps Washington, D.C. 20380 Attn: Code AX	(1)	National Bureau of Standards Washington, D.C. 20234	
		Attn: Metallurgy Division Inorganic Materials Division	(1) (1)
Naval Ship Engineering Center Department of the Navy CTR BG #2 3700 East-West Highway Prince Georges Plaza Hyattsville, Maryland 20782 Attn: Engineering Materials and Services Office, Code 6101	(1)	Defense Metals and Ceramics Information Center Battelle Memorial Institute 505 King Avenue Columbus, Ohio 43201	(1)
Army Research Office Box CM, Duke Station Durham, North Carolina 27706 Attn: Metallurgy & Ceramics Div.	(1)	Director Ordnance Research Laboratory P.O. Box 30 State College, Pennsylvania 16801	(1)
Army Materials and Mechanics Research Center Watertown, Massachusetts 02172 Attn: Res. Programs Office (AMXMR-P)	(1)	Director Applied Physics Laboratory University of Washington 1013 Northeast Fortieth Street Seattle, Washington 98105	(1)

Air Force
Office of Scientific Research
Bldg. 410
Bolling Air Force Base
Washington, D.C. 20332
Attn: Chemical Science Directorate
  Electronics and Solid State
  Sciences Directorate
	(1)
	
	(1)
		Metals and Ceramics Division
		Oak Ridge National Laboratory
		P.O. Box X
		Oak Ridge, Tennessee 37380
		
		Los Alamos Scientific Laboratory
		P.O. Box 1663
		Los Alamos, New Mexico 87544
		Attn: Report Librarian
			(1)
			
			(1)

Air Force Materials Lab (LA) Wright-Patterson AFB Dayton, Ohio 45433	(1)	Argonne National Laboratory Metallurgy Division P.O. Box 229 Lemont, Illinois 60439	(1)

Organization	No. of Copies	Organization	No. of Copies
Brookhaven National Laboratory Technical Information Division Upton, Long Island New York 11973 Attn: Research Library	(1)		
Library Building 50 Room 134 Lawrence Radiation Laboratory Berkeley, California	(1)		

Technical and Summary Reports

Advanced Research Projects Agency
Materials Science Director
1400 Wilson Boulevard
Arlington, VA 22209

Professor Michael Bell
Yeshiva University
Belfer Graduate School of Science
New York, NY 10033

Dr. Don Berlincourt
Channel Products
16722 Park Circle Dr. W.
Chagrin Falls, OH 44022

Dr. J. V. Biggers
Pennsylvania State University
Materials Research Laboratory
University Park, PA 16802

Mr. George Boyer
Sensor Systems Program
Office of Naval Research
Code 222
Arlington, VA 22217

Professor R. Bradt
Ceramics Section
Materials Sciences Department
The Pennsylvania State University
University Park,, PA 16802

Dr. Dean Buckner
Piezo Products Division
Gulton Industries
P.O. Box 4300
Fullerton, CA 92634

Dr. Robert Callahan
Channel Industries
839 Ward Drive
Box 3680
Santa Barbara, CA 93105

Professor L. E. Cross
The Pennsylvania State University
Materials Research Laboratory
University Park, PA 16802

Mr. N. Coda
Vice President for Engineering
Erie Technological Products
West College Avenue
State College, PA 1680

Dr. A. G. Evans
Rockwell International
P.O. Box 1085
1049 Camino Dos Rios
Thousand Oaks, CA 91360

Dr. Richard Fulrath
University of California
266 Hearst Mining Building
Berkeley, CA 94720

Dr. Gene Haertling
Motorola Corporation
3434 Vassar, NE
Albuquergue, NM 87107

Dr. W. B. Harrison
Honeywell Ceramics Center
1885 Douglas Drive
Golden Valley, MN 55422

Dr. D. P. H. Hasselman
Virginia Polytechnic Institute
Department of Materials Sciences
Blacksburg, VA

Dr. L. L. Hench
Department of Metallurgy
University of Florida
Gainesville, FL 32603

Dr. A. H. Heuer
Professor of Ceramics
Case Western Reserve University
University Circle
Cleveland, OH 44106

Dr. F. Robert Hill
Marine Resources
755 Highway 17 & 92
Fern Park, FL 32730

SUPPLEMENTARY DISTRIBUTION LIST (CONT"D)

Dr. Bernard Jaffe
232 Forbes Road
Bedford, OH 44146

Dr. Paul Jorgensen
Stanford Research Institute
333 Ravenswood Avenue
Menlo Park, CA 94025

Dr. R. N. Katz
Army Materials and Mechanics
  Research Center
Watertown, MA 02172

Dr. H. Kirchner
Ceramic Finishing Company
P. O. Box 498
State College, PA 16801

Dr. B. G. Koepke
Honeywell, Inc.
Corporate Research Center
10701 Lyndale Avenue South
Bloomington, MN 55420

Mr. Frank Koubek
Naval Surface Weapons Center
White Oak Laboratory
Silver Spring, MD 20910

Dr. J. Lankford
Southwest Research Institute
8500 Culebra Road
San Antonio, TX 78284

Dr. R. Lapetina
Edo Western Corporation
2645 South 300 West
Salt Lake City, UT 84115

Mr. C. LeBlanc
Naval Underwater Systems Center
TD 121
Newport, RI 02840

Dr. R. E. Loehman
University of Florida
Ceramics Division
Gainesville, FL 32601

Professor P. B. Macedo
The Catholic University of America
Washington, DC 20017

Dr. N. Perrone
Code 474
Office of Naval Research
800 N. Quincy Street
Arlington, VA 22217

Dr. R. Pohanka
Naval Research Laboratory
Code 6130
Washington, DC 20375

Dr. R. Rice
Naval Research Laboratory
Code 6360
Washington, DC 20375

Dr. Frank Recny
General Electric Company
Court Street
Plant Building C
Box 1122
Syracuse, NY 13201

Dr. J. H. Rosolowski
General Electric Company
Research and Development Center
P.O. Box 8
Schenectady, NY 02301

Dr. D. A. Shockey
Stanford Research Institute
Poulter Laboratory
Menlo Park, CA 94025

Dr. J. H. Simmons
Catholic University of America
Washington, DC 20064

Dr. P. L. Smith
Naval Research Laboratory
Code 6361
Washington, DC 20375

SUPPLEMENTARY DISTRIBUTION LIST (CONT'D)

Dr. R. W. Timme
Naval Research Laboratory
Code 8275
Underwater Sound Reference Division
P.O. Box 8337
Orlando, FL 32806

Dr. Charles C. Walker
Naval Sea Systems Command
National Center #3
2531 Jefferson Davis Highway
Arlington, VA 20390

Dr. Paul D. Wilcox
Sandia Laboratories
Division 2521
Albuquerque, NM 87115

The State University of New York
  at Alfred
Material Sciences Division
Alfred, NY

SUPPLEMENTARY DISTRIBUTION LIST

Dr. N. S. Corney
Ministry of Defence
(Procurement Executive)
The Adelphi
John Adam Street
London WC2N 6BB
UNITED KINGDOM

Dr. Murray Gillen
Australian Embassy
Washington, DC 33801

Dr. D. J. Godfrey
Admiralty Materials Laboratory
Ministry of Defence
(Procurement Executive)
Holton Heath
Poole, Dorset
BH16 6JU
UNITED KINGDOM